Դավիթ Արայի Զարգարյան

ԱԿՏԻՎ ԳԱԼԱԿՏԻԿԱԿԱՆ ՄԻՋՈՒԿՆԵՐԻ ՄԵԾ ՄԱՍՇՏԱԲՈՎ ՇԻԹԵՐԻ ՃԱՌԱԳԱՅԹՄԱՆ ՄԵԽԱՆԻԶՄՆԵՐԻ ՈՒՍՈՒՄՆԱՍԻՐՈՒԹՅՈՒՆԸ

ԱՏԵՆԱԽՈՍՈՒԹՅՈՒՆ

Ա.03.02 - «Աստղաֆիզիկա» մասնագիտությամբ
ֆիզիկամաթեմատիկական գիտությունների
թեկնածուի գիտական աստիճանի համար

Գիտական ղեկավար՝
ֆ.մ.գ.թ., Հայկ Հարությունյան

ԲՅՈՒՐԱԿԱՆ – 2018

NATIONAL ACADEMY OF SCIENCES OF THE REPUBLIC OF ARMENIA
BYURAKAN ASTROPHYSICAL OBSERVATORY

Davit Ara Zargaryan

STUDY OF THE EMISSION MECHANISMS OF LARGE SCALE JETS IN ACTIVE GALACTIC NUCLEI

DOCTORAL THESIS

A thesis submitted in fulfillment of the requirements
for the degree of Doctor of Philosophy
in
specialization 01.03.02 – "Astrophysics"

Supervisor:

Dr. Hayk Harutyunyan

BYURAKAN - 2018

Contents

INTRODUCTION

This thesis is dedicated to study the high energy (HE) emission processes in the Active Galactic Nuclei (AGNs). The galaxies, which have very bright nuclei, so bright that the central region can be equal or more luminous than the remaining galaxy light, are called AGNs [1]. Being the brightest sources in the universe, AGNs are discovered from far distances and the observations of these distant sources are essential for investigating the emission and acceleration processes in single objects as well as to study the formation and evolution of the Universe [2].

Considering the huge energies usually realized from the AGNs (sometimes AGNs can have a luminosity of $\sim 10^{49}\ erg\ s^{-1}$), which are produced the result of the physical processes, so they are special targets for exploring the real nature of the relativistic outflows [1]. It is believed, that the source of energy output is the accretion of matter onto supermassive black hole (billions of solar mass), although alternative considerations such as the main emission is produced from very dense and massive object cannot be ruled out. Moreover, currently the most common theory for energy extraction from the central source (considering it is a black hole) is the Blandford–Znajek mechanism [3].

The observations show that around the central objects in AGNs from the matter following on it an accretion disc is formed. This accretion disc emits in ultraviolet (UV) and sometimes in the X-ray bands. Massive explosions take place in galactic nuclei, and as a result, a huge amount of mass is ejected [4]. The accretion disc powers extremely energetic and highly collimated outflowing plasma structure: so called jet [1]. They can extend up to several hundreds of kilo parsec (kpc) into space often remaining a remarkably high degree of collimation. The radio jets occur in about 10 % of AGNs, in so-called radio-loud objects [5]. These jets not only carry enormous amount of energy but also appear to be one of the crucial components of different AGN types. According to the current unification theory of AGNs, due to the jet orientation AGNs exhibit a variety of appearances [5]. The extreme types of AGNs are blazars when the relativistic jet is directed towards our line of sight [5]. Generally, they are divided into two subclasses: namely, blazars, which have very weak, or

no emission lines are BL Lac objects (BL Lacs) instead Flat Spectrum Radio Quasars (FSRQs) show strong emission lines [5]. The nonthermal emission from blazars is characterized by strong variability (the flux increases in short time scale) which sometimes can be as short as the order of a few minutes. This implies that the emission from blazars is produced in very compact region of the jet, and their observations provide a unique chance to investigate the structure of sub-parsec scale jets. As the emitting material in blazars jets moves with very fast velocities, and the jet makes small angle to the observer, the nonthermal radiation emitted from jets is amplified by relativistic factors and it dominates over the emission of other AGN components [1]. This boosted emission is significantly less in radio galaxies: AGNs which are very bright in the radio band and their jets are oriented at a larger viewing angle [5]. The boosted emission from the jets of radio galaxies is the same order or sometimes even less as compared with the emission from other components of the AGN (e.g., the lobes, knots middle relativistic plasma, etc.). Therefore, observing radio galaxies will allow not only to study the jet emission but also the other important components of the AGNs are investigating which are crucial for understanding the physics of AGNs. Based on the radio morphology, radio galaxies are commonly divided into two subclasses: Fanaroff-Riley I (FRI) and FRII [6]. FRI shows bright jets close to the nucleus, while FRII shows prominent hot spots far from it. In the unification schemes, FRI galaxies are the parent population of BL Lacs while FSRQs are linked with FRII galaxies [5].

One of the most interesting and unsolved phenomena in astrophysics is to understand the launching, collimation and propagation of jets [1]. Even if the emission from the jets is detected almost in all from radio to HE γ-ray bands, the formation and connection with central source, the particle emission and acceleration processes within the jet as well as the jet composition (e.g., the relative contribution of the electrons and protons) are unclear. There are different ways for solving the above mentioned problems, for example using hydrodynamical simulations of jet or using realistic high resolution simulations of the jets to investigate their impact on the environments where they propagate, so to understand their collimation [1, 7]. However, all the mentioned simulations require that the initial parameters describing the jet match as closely as possible the actual parameters, which can be obtained

only in detailed and high-resolution observations. Therefore, the jet observations in different bands are not only crucial for studying the emission processes in the jets but also these results can be used for other jet studies.

The observations of jets especially in radio or optical bands (where the instruments have better angular resolution) show that there are substructures (referred as knots) within the large scale jets of radio-loud AGNs. The natures of these knots have not well known yet; they are bright local regions of the jet with the size varying from pc to kpc scales [7]. Up to now, in order to explain the formation of knots different scenarios have been proposed, such as internal shocks due to surface instabilities or changing surface pressure, variations in the jet velocity, bow shocks due to collisions with small, dense clouds etc. [8]. The emission from these knots was detected in radio, optical and X-ray bands, which shows they are ideal sites where the particles are effectively accelerated. In the standard picture of jet propagations, the jet is decelerated in a hot spot, where its kinetic energy is converted into relativistic electrons and some part in a magnetic field [8]. Sometimes, these electrons are further reaccelerated reaching up to GeV/TeV band and as a result the emission from these hot spots up to X-ray band was detected [8].

The study of emission from the knots and hot spots in large scale jets of AGNs has become more important after the lunch of Chandra telescope, which, due to its excellent spatial resolution, is able to resolve X-ray knots of the jets. In most of the knots, the X-ray knots well coincide with their radio/optical contours and the emission can be explained by synchrotron emission from accelerated electrons [8]. The multiwavelength data from the observations of the knots in different bands provide useful information about the basic emission mechanism and the underlying acceleration processes involved there. However, in some cases, the X-ray emission is described by a hard power-law index and they have larger flux compared with the radio one, and the extrapolation of low energy synchrotron component cannot explain the observed X-ray data [9]. There are different mechanisms proposed to explain the origin of this second component (e.g., inverse Compton scattering of different photon fields, synchrotron emission of second population of electrons or energetic protons, etc.), but up to now the exact mechanism responsible for the emission is

not clear [10-14]. The observations of knots in different bands (especially in X-ray band) and the theoretical interpretation of the origin from them (especially in these peculiar cases) are among the hot topics in astrophysics.

Tremendous progress in the study of emission from AGNs is achieved after the launch of Fermi Large Area Telescope (Fermi-LAT) in 2008. After the initial four years of operation, it detected more than 1000 AGNs and provided continuous γ-ray data over very long period (now already nearly 10 years). Most likely, the emission in the γ-ray band was produced from pc/sub-pc scale jet (inferred from the observed variability) and combining the γ-ray data with observations in other bands (from radio to X-rays) the processes in the jet occurring near the nuclei (where the jet is most likely formed) can be investigated [15-19]. On the other hand, some AGNs observed in the γ-ray band have also knots in their jets and from the observations of these knots permit to investigate the same jet properties much farther from the nuclei [20].

Combining the data derived at the sub-*pc* and kilo-parsec regions of the same jet can be crucial for powerful extragalactic jets studies, e.g., help to understand the evolution and propagation of the jets from the central engine to the outer regions, where the jet is starting to decelerate significantly [20]. This approach can be fruitfully applied when the large-scale jets are long enough to be resolved by Chandra. Unfortunately, the blazars do not tend to have well-studied large-scale jets, as they are most closely aligned with the line of sight, the projected angular dimension of the large-scale jet is reduced. Thus, for such kind of study good targets are radio galaxies. Up to now in the γ-ray band there are 22 radio galaxies detected and most of them are nearby, so their jets are well studied in almost all bands [15,20]. Therefore, studying the emission from the jet of these sources in different scales can help not only to understand the radiation process in the jets but also their dynamics.

The goals of this work:
- Select those radio galaxies which are detectable both in HE γ-ray band (by Fermi-LAT), and at the same time the emission from large scale jets are being detected by Chandra.

- Analyze the HE γ-ray data from seven years (from 2008 to 2015) of Fermi-LAT observations of selected sources. Make spectral analysis to estimate the photon index and flux in HE γ-ray band. Collect data from the observation of these sources in other bands, etc.

- From previous studies of the large scale jets of the considered sources in the radio, optical and X-ray bands, identify the knots and hotspots, select their coordinates and regions in the jets, estimate their physical sizes etc.

- Using the Chandra observations of these knots and hotspots, find their X-ray spectra in the 0.5-10 keV energy range. Use Chandra data accumulated in different periods to investigate the parameter changes in time.

- For all considered sources, make theoretical modeling of the spectral energy distributions, correspondingly observed for both < pc and > kpc regions. Using the modeling results to estimate the jet luminosity, magnetic field, etc. in different scales and compare them.

- Study in detail the emission from the peculiar jet of 3C 120, which extends up to 100 kpc. This jet has a few bright knots well detected in the X-ray band and the core emission well studied up to HE γ-ray band.

- Using the obtained results, investigate the particles acceleration and emission processes.

Scientific novelty:

- The spectral and temporal characteristics of M87, Pictor A, 3C 303, 3C 275.1, NGC 6251, 3C 207, 3C 111 and 3C 120 radio galaxies in the γ-ray band are studied, based on the 7-years (2008-2015) analysis of Fermi-LAT data. The results show that γ-ray emission from the considered sources can be described by Power-law model with the photon index indices of $\Gamma_\gamma > 2.1$ with the average gamma-ray flux of $< (4.87 \pm 0.32) \times 10^{-8}$ photon cm^{-2}s^{-1}. Temporal variations of the γ-ray emission have been studied using the light curves generated by adaptive binning method.

- X-ray data from the Chandra observations of large scale structures of the jets of M87, Pictor A, 3C 303, 3C 275.1, NGC 6251, 3C 207, 3C 111 and 3C 120 radio

galaxies have been analyzed. The origin of X-ray emissions from the knots and hotspots is investigated. It is shown, that X-ray emissions from most of these large scale structures have X-ray photon indices $\Gamma_X < 2.0$, which does not change significantly during in different years.

- Theoretical modeling of the data from the observations of the inner jet near the central sources ($<$ pc) shows that the emission can be described by synchrotron/synchrotron self-Compton (SSC) model. The estimated jet power is $L_{jet} \cong (0.51 - 26.47) \times 10^{44} erg\ s^{-1}$ and the magnetic field is $B \cong (0.3 - 100)\ mG$ which are typical for radio galaxies.

- The emission from large scale structures of jet cannot be explained by synchrotron emission from the electrons radiating in radio-optical band, and it is necessary to take into account an additional contribution from other components. For example, the Inverse Compton scattering of CMB photons if the jet remains highly relativistic at kpc distance from the core, or the synchrotron emission from more energetic electrons.

- For the first time, the luminosities of the jet estimated near the core and at kpc distance from it are compared. Interestingly, for most of the jets the luminosities of the innermost and outer regions are comparable, suggesting that the jet does not suffer important energy losses when propagating from the regions close to the black hole to those at hundreds of kiloparsecs from it.

- We compare the constraints on the physical parameters in the innermost ($\leq$ pc) and outer ($\geq$ kpc) regions of the 3C 120 jet by means of a detailed multiwavelength analysis and theoretical modeling of their broadband spectra. The data collected by Fermi LAT (γ-ray band), Swift (X-ray and ultraviolet bands) and Chandra (X-ray band) are analyzed together and the spectral energy distributions are modeled using a leptonic synchrotron and inverse Compton models, taking into account that seed photons are originating inside and outside of the jet. The γ-ray flux from the inner jet of 3C 120 was characterized by rapid variation from MJD 56900 to MJD 57300. Two strong flares were observed on April 24, 2015 when, within 19.0 minutes and

3.15 hours the flux was as high as $(7.46 \pm 1.56) \times 10^{-6}\ photon\ cm^{-2}s^{-1}$ and $(4.71 \pm 0.92) \times 10^{-6}\ photon\ cm^{-2}s^{-1}$ respectively, with $\geq 10\sigma$. During these flares the apparent isotropic γ-ray luminosity was $L_\gamma \cong (1.20 - 1.66) \times 10^{46}\ erg\ s^{-1}$ which is not common for radio galaxies.

- It is shown that the broadband emission from the innermost jet in the quiet and flaring states can be described as SSC emission while inverse Compton scattering of dusty torus photons cannot be excluded for the flaring states. The X-ray emission from the knots can be well reproduced by inverse Compton scattering of cosmic microwave background photons only if the jet is highly relativistic (since even when $\delta = 10$ still $U_e/U_B \geq 80$). These extreme requirements can be somewhat softened assuming the X-rays are from the synchrotron emission of a second population of very-high-energy electrons.

Basic thesis statements:

- The HE γ-ray data from the observations of M87, Pictor A, 3C 303, 3C 275.1, NGC 6251, 3C 207, 3C 111 and 3C 120 radio galaxies has been analyzed using seven years Fermi LAT data and the flux, photon index in the γ-ray band were estimated. In addition, the temporal variation of the γ-ray flux was investigated.

- The emission spectra observed from sub-pc regions near the core have been modeled and the parameters were estimated using Markov Chain Monte Carlo method. It is shown, that the multiwavelength emission of the considered sources can be explained by SSC mechanism.

- The Chandra X-ray observations of 30 knots and 6 hotspots regions in the jets of considered sources have been analyzed and corresponding database created. It is shown, that for the several knots and hotspots the radio to X-ray emission cannot be explained by emission from single electrons population and additional contribution is needed. The emission in the X-ray band can be described by Inverse Compton scattering of the cosmic microwave background photons if the jet matter velocity remains relativistic even kpc distances from the core, otherwise the second and letter accelerated electrons synchrotron emission is needed to explain the X-ray emission.

- The main properties of the jets (i.e. luminosity, magnetic field, particle density etc.) of considered sources, near the central source and at the kpc distances from it have been estimated and compared by theoretical modeling. These are crucial for understanding the dynamics and the evolution of the jet.

- Significant variability of the HE γ-ray emission from 3C 120 radiogalaxy has been observed. Especially, the maximum flux increased up to $F_\gamma = (7.46 \pm 1.56) \times 10^{-6}\,\text{photon}\,\text{cm}^{-2}\text{s}^{-1}$ with the corresponding luminosity of $L_\gamma = (1.2 - 1.6) \times 10^{46}\,\text{erg}\,\text{s}^{-1}$.

- It is shown that the HE γ-ray emissions from the inner jet regions of 3C 120 jet in active and quiescent states can be described as SSC emission while inverse Compton scattering of dusty torus photons cannot be excluded for the flaring states. The X-ray emission from the knots can be well reproduced by inverse Compton scattering of cosmic microwave background photons only if the jet is highly relativistic or by synchrotron emission of a second population of very-high-energy electrons.

The practical value:

The obtained results can be used for studying the dynamics of the jet, as well as to understand the acceleration and radiation mechanisms of the particles. The basic parameters estimation methods, based on the analysis and theoretical modeling of the data from the observations in different scales of the jet, can be used for studying the emission from the large scale jets of the another AGNs.

During the theoretical modeling of data using the electrons distributions accelerated in different times, indicate that inside the large scale jet of the radio galaxies, even the kpc distance from the core the particles can be accelerated. These results can be used for modeling the emission from the knots.

The thesis consists of introduction, 4 chapters, a summery and bibliography.

In the introduction the relevance of the work, formulation of the main objectives and goals are presented.

In chapter 1 very briefly the main properties of AGNs, their unification scenarios, their basic components (knots, hot spots etc.) and the main emission process responsible for the emission in radio galaxies are presented.

In chapter 2 the basic steps and methods of data analyses (data extraction and preparation, spectra analyses etc.) observed both with Chandra and the Fermi-LAT are presented.

In Chapter 3 the constraints on the physical parameters in the innermost ($\leq$ pc) and outer ($\geq$ kpc) regions of the 3C 120 jet are compared by means of a detailed multiwavelength analysis and theoretical modeling of their broadband spectra. Namely, the data collected by Fermi-LAT (γ-ray band), Swift (X-ray and ultraviolet bands) and Chandra (X-ray band) are analyzed together and the spectral energy distributions are modeled using a leptonic synchrotron and inverse Compton models, taking into account the seed photons originating inside and outside of the jet.

In chapter 4 the emission process in the radio galaxies jets which are detected in the γ-ray band and have knots or hot spots in their jets are investigated. By theoretical modeling the main properties of the jet (e.g., luminosity, magnetic field, etc.) are estimated in different scales and are compared.

In summmery the main results obtained in the thesis are presented.

Chapter 1

ACTIVE GALACTIC NUCLEI

Active galactic nuclei (AGNs) are the brightest sources in the universe. AGNs are galaxies being very bright in the central/nuclear region, which is hosting a super massive black hole (SMBH) [7]. Around this black hole when the matter falls onto the black hole, it forms an accretion disk [1]. This accretion disk, emits in the optical and UV energies, is common for almost all AGN types. The gas surrounding the black hole is photoionized and radiates emission lines, with from nearby regions within 10^3 Schwarzschild radii the broad lines are produced, while the narrow lines are produced from much more extended regions [1]. The strong infrared emission observed in all AGNs shows the presence of obscuring matter (torus) concentrated towards the plane in which the accretion occurs [22]. Next, the accretion disc powers a linear structure, which transports energy from the core out to intergalactic media (jets) [1] and the jets are observed in almost all powerful radio-loud AGNs. The jets exhibit a large range of apparent velocities, from middle relativistic to highly relativistic motion [23]. The emission from the jets has been observed across all the electromagnetic spectrum: from radio to HE γ-ray bands.

1.1 AGNs Unification

There are different types of AGNs and it is quite complex to distinguish between them. Depending on their observed properties and their physical parameters, the unified models have been proposed and a common division is based on the radio observations: in the radio band AGNs can be divided into two types, radio-loud and radio-quiet [5]. The radio loudness is defined as the ratio of the radio flux at 5 GHz to optical (B-band) flux, and the radio louds are when $F_{5\,GHz}/F_B > 10$ [5,24]. The observations show that roughly 10-15 % of AGNs are radio-loud [5]. Comparing radio loud and quiet objects it is noticeable that large scale jets and lobes are formed in the radio-loud AGNs [5]. The radio loud AGNs are further divided depending on the jet orientation. One of the fainter galaxies are Seyferts, which are

divided into two subclasses Seyfert 1 (Sy1) and Seyfert 2 (Sy2) galaxies based on their optical spectra [25]. A sketch of blazars unification depending on the jet orientation is shown in Fig. 1.1. The most luminous AGNs are the blazars when the jet has smaller inclination. The blazars are subdivided into two large classes depending on the emission line: blazars with no or weak emission lines are BL Lacs while the others are FSRQs [5].
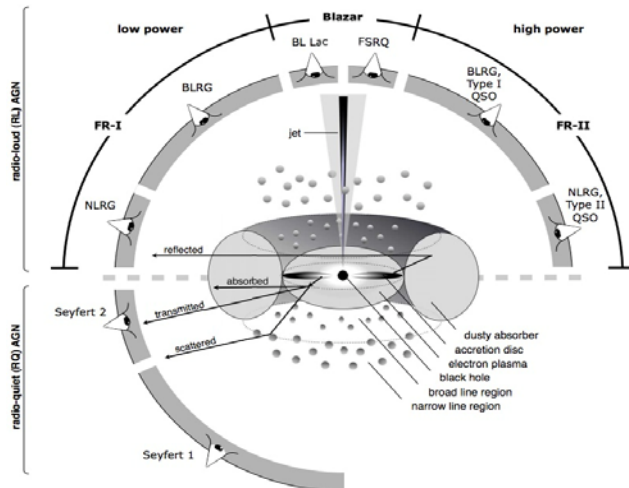
FIGURE 1.1: The illustrated demonstration of the unified AGN model [7].

The radio galaxies even being the same objects show different radio morphologies. According to the Fanaroff and Riley classification [6], the radio galaxies are distinguished by their luminosity at the 178 MHz, the boundary luminosity corresponds to $\approx 2 \times 10^{25} \, W \, Hz^{-1} \, sr^{-1}$: the ones having luminosity below this limit are FR-I sources while the other ones are FR-II classes.
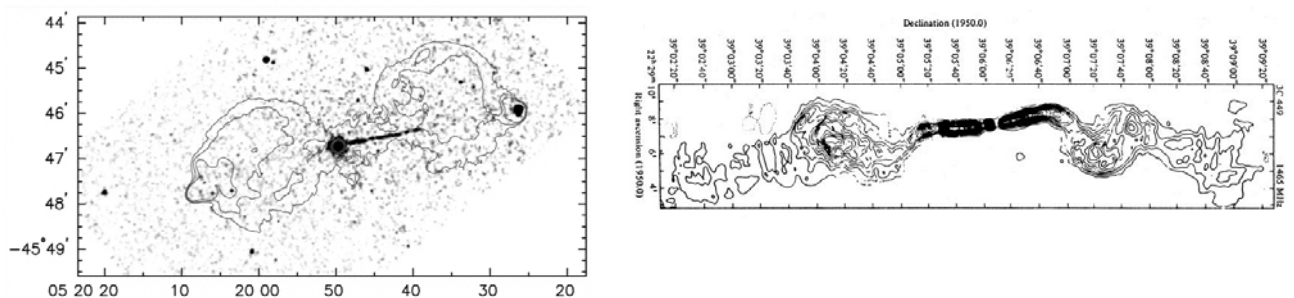
FIGURE 1.2: On the left side is presented the X-ray image of FR II radiogalaxy Pictor A overlaid with radio contour. At the hundred kpc distance from the core well appearing bright hotspot (taken from [8]. On the right side is presented the 3C 449 radiogalaxy [26], as an example of FR I class.; compared to the FR II radio galaxies the jet disappears at short distances and afterwards the main radiation is dominated in near the central region.

Examples of FRI and FRII sources are shown in Fig. 1.2. The luminosity of FR-I radio galaxies gradually decreases farther from the core while the FR-IIs the jet is more bright farther from the core in the lobes.

1.2 Jets

As we mentioned above, one of the main characteristic structures of the AGNs, are the large scale jets. They carriy huge amount of mass and momentum and emerging from the nucleus and transports the energy up to kpc distances forming diffuse radio lobes [1,22]. Due to its peculiarity jets are observed almost all wavebands. In the radio bands a very sensitive observations allow to identify and study different components of the extragalactic jets also the VLBI radio observations allowed to estimate some individual components with superluminal motion [23]. Then the jet and its components are observed in higher frequency observations, such as optical and X-ray bands, which allow to understand many important parameters of the jet as well as to investigate the particle acceleration and emission processes. The observations of the jets in different bands have identified knots and hotspots structures in their large scale jet [8, 9]. These are the bright features of the large kpc jets, which are strong emitters in almost all energy bands (from radio to X-ray bands). Even up to now, many knots have been detected and their nature (formation) is not well known yet. One of the most popular theories is that in the radio to optical band the emission can be well explained by electron synchrotron radiation, while the X-ray component's flux sometimes exceeds the radio flux and it has harder power low index, so multi component emission scenarios are proposed [9-14]. In addition, an alternative possibility can be the proton synchrotron emission [27]. As the knots are very luminous and being observed in almost all band, the current radio, optical and X-ray telescopes allow not only to resolve but also make detailed spectral analysis of these knots emission, considering available large amount of data. Understanding the nature and exact mechanism responsible for the emission from the knots is one of the most discussed topics in astrophysics.

1.3 Radiative processes

Here below the main processes responsible for nonthermal emission in astrophysical source are discussed. Since in AGNs we have extreme conditions and some astrophysical phenomena taking place on the relativistic velocities, the study of particle acceleration and radiation mechanisms from these sources is one of the most important topics. The basic radiation mechanisms are synchrotron radiation and Inverse-Compton scattering, which are discussed below.

1.3.1 Synchrotron radiation

The main mechanism responsible for the emission in the low energy band (e.g., in AGNs, supernova remnant, pulsar wind nebulae etc.) is the synchrotron emission of electrons in magnetized medium. Relativistic moving electrons in the magnetic field are affected by Lorentz force and the electrons obtained spiraling path and emit photons via synchrotron radiation. Considering, an electron with energy E_e moves in B magnetic field radiated photons that have the following differential spectrum [28,29]

$$\frac{dN_{e,\gamma}}{dE_{e,\gamma}dt} = \frac{\sqrt{3}}{2\pi} \frac{e^3 B}{m_e c^2 \hbar E_{e,\gamma}} F\left(\frac{E_{e,\gamma}}{E_c}\right) \tag{1.1}$$

where $E_{e,\gamma}$ and m_e is the γ-ray emitted electron energy and mass respectively. The F(x) function is defined

$$F(x) = x \int_x^\infty K_{5/3}(\tau) d\tau \tag{1.2}$$

Here, $K_{5/3}$ is the modified Bessel function and E_c is the characteristic energy of synchrotron photons

$$E_c = \frac{3e\hbar B}{2m_e c} \left(\frac{E}{m_e c^2}\right)^2 \tag{1.3}$$

The function F(x) in the homogenous magnetic field can be approximated by the following function [28]

$$F(x) \approx 2.15x^{\frac{1}{3}}(1 + 3.06x)^{\frac{1}{6}} \times \frac{1 + 0.884x^{\frac{2}{3}} + 0.471x^{\frac{4}{3}}}{1 + 1.64x^{\frac{2}{3}} + 0.974x^{\frac{4}{3}}} e^{-x} \tag{1.4}$$

The emissivity F(x) function is depicted in Fig. 1.3 and is clear that the maximum value of the function $F(x) = 0.918$ is reached when x= 0.2858.
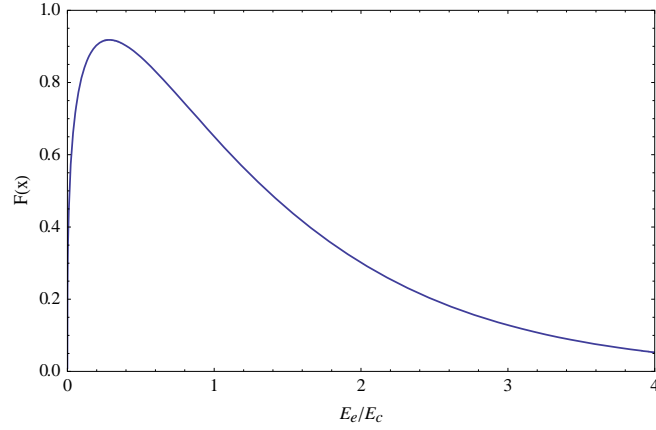

FIGURE 1.3: The F(x) as a function of E_e/E_c ratio. As shown in graph the F(x) function has maximum value when the ratio is equal 0.2858.

Considering inhomogeneous magnetic field, the corresponding function is (from [28,29])

$$G(x) = \frac{x}{20}\left[(8 + 3x^2)\left(k_{1/3}\right)^2 + xk_{2/3}\left(2k_{1/3} - 3xk_{2/3}\right)\right] \tag{1.5}$$

where $k_{1/3} = K_{1/3}\left(x/2\right)$ and $k_{2/3} = K_{2/3}\left(x/2\right)$, which can be approximated using

$$G(x) \approx \frac{1.808x^{\frac{1}{3}}}{\sqrt{1 + 3.4x^{\frac{2}{3}}}} \frac{1 + 2.21x^{\frac{2}{3}} + 0.347x^{\frac{4}{3}}}{1 + 1.353x^{\frac{2}{3}} + 0.217x^{\frac{4}{3}}} e^{-x} \tag{1.6}$$

function. Compared with F(x), the maximum of G(x) is comparably small $G(x) = 0.7126$, when $x = 0.2292$.

In order to calculate the synchrotron emission from an electron population with $N(\gamma)$ distribution, Eq. 1.1 should be multiplied by $N(\gamma)$ and integrated over all energies of the electrons. The energy losses and cooling times of electrons can be calculated by [29]:

$$\frac{d\gamma}{dt} = \frac{4}{3}\frac{\sigma_T c}{m_e c^2}\frac{B^2}{8\pi}\gamma^2; \quad t_{cool} = \frac{\gamma}{d\gamma/dt} \tag{1.7}$$

1.3.2 Inverse-Compton scattering

In different objects (including AGNs) the relativistic electrons can interact with low energy photons and inverse Compton up scatter these photons to higher energies. Defining the parameter $\kappa_0 = \varepsilon_e \omega_0$ (where ε_e and ω_0 are the interacting electron and photon energies), the total cross section of Inverse Compton scattering is [30]

$$\sigma_{IC} = \frac{3\sigma_T}{8k_0}\left[\left(1 - \frac{2}{k_0} - \frac{2}{k_0^2}\right)\ln(1 + 2k_0) + \frac{1}{2} + \frac{4}{k_0} - \frac{1}{2(1 + 2k_0)^2}\right] \tag{1.8}$$

The spectrum of inverse Compton scattered photon can be calculated by [29,30]

$$\frac{d^2N(\theta, \varepsilon_\gamma)}{d\varepsilon_\gamma d\Omega} = \frac{3\sigma_T}{16\pi\omega_0\varepsilon_e^2}\left[1 + \frac{z^2}{2(1 - z)} - \frac{2z}{b_\theta(1 - z)} + \frac{2z^2}{b_\theta^2(1 - z)^2}\right] \tag{1.9}$$

where $b_\theta = 2(1 - cos\theta)\omega_0\varepsilon_e$, $z = \varepsilon_\gamma/\varepsilon_e$. Integrated over the angle θ and appointing $b = 4k_0$, we receive the spectrum for the isotropically distribute particle field [29]

$$\frac{dN(\varepsilon_\gamma)}{d\varepsilon_\gamma} = \frac{3\sigma_T}{4\omega_0\varepsilon_e^2}\left[1 + \frac{z^2}{2(1-z)} - \frac{z}{b(1-z)} + \frac{2z^2}{b^2(1-z)^2} + \frac{z^3}{2b(1-z)^2} - \frac{2z}{b(1-z)}\ln\frac{b(z-1)}{z}\right] \tag{1.10}$$

the energy loss rate of electrons can be calculated by

$$\frac{d\varepsilon_e}{dt} = \frac{3\sigma_T c n_{ph}}{4\omega_0 b}\left[\left(6 + \frac{b}{2} + \frac{6}{b}\right)\ln(1 + b) - ln^2(1 + b) - 2Li\left(\frac{1}{1+b}\right) - \frac{\left(\frac{11}{12}\right)b^3 + 8b^2 + 13b + 6}{(1+b)^2}\right] \tag{1.11}$$

where $Li(x) = \int_x^1 (1 - y)^{-1}\ln(y)dy$. The b parameter shows the transition between Thomson and Klein-Nishina regimes. For example, the Eq. 1.11 can be approximated by the following equations in different regimes [29]

i) Thomson regime ($b \ll 1$)

$$\frac{d\varepsilon_e}{dt} = \frac{4}{3}\sigma_T c\omega_0 n_{ph}\varepsilon_e^2 \tag{1.12}$$

ii) Klein-Nishina regime ($b \gg 1$)

$$\frac{d\varepsilon_e}{dt} = \frac{3}{8}\frac{\sigma_T c n_{ph}}{\omega_0}\left(lnb - \frac{11}{6}\right) \tag{1.13}$$

Chapter 2

X-RAY AND γ-RAY TELESCOPES

2.1 Fermi Gamma-ray Space Telescope

2.1.1 Introduction

The Fermi Gamma Ray Space Telescope (FGST), which was formerly called the Gamma-Ray large area Space Telescope (GLAST), carries two instruments, the Large Area Telescope (LAT) and the Gamma-Ray Burst Monitor (GBM), and is one of the unique instruments, currently working on HE band [31]. The LAT's viewing sector is enough to cover about 20% of the sky at any time and orbiting constantly around the earth, each three hours it can scan the whole sky. The detector's design (e.g. the accuracy of the converter-tracker and calorimeter), makes possible to detect photons from 20 MeV to more than 300 GeV [31]. The instrument with such a wide field-of-view, large effective area, good angular resolution and energy band, permits to study the HE γ-rays emission processes in the active galactic nuclei.

As highlighted above, the second instrument on the board of Fermi satellite, devoted to observing the transient phenomena in the 8 keV - 40 MeV energy range, is the Gamma-ray Burst Monitor (GBM) [31]. These two instruments provide an opportunity to investigate different astrophysical and cosmological phenomena such as a system with a supermassive black hole, pulsars, active galactic nuclei, the nature of γ-ray bursts, other high-energy phenomena, etc.

In this thesis, I have used Fermi-LAT data to study the HE γ-ray emission from the core of radio galaxies. The steps of data analyses, as well as how to prepare the spectral energy distributions, temporal variability, etc. are presented in section 2.1.4.

2.1.2 The Fermi-LAT instrument

The Fermi-LAT instrument is sensitive to the particles (photons) in the energy range > 20 MeV. When the high-energy particles infiltrate into the detector, γ-rays interact with converter, made of 16 planes of high-Z material, produce e+ e− particles (see Fig. 2.1) [31]. Furthermore, these pairs are stopped in cesium iodide calorimeter, which allows to compute the primary energy of incoming photons. In addition, the detection in the calorimeter allows to compute all necessary information for the incoming photons, e.g., the direction, the energy angle etc. More details on the technical parameters of the instrument can be obtained from [31].
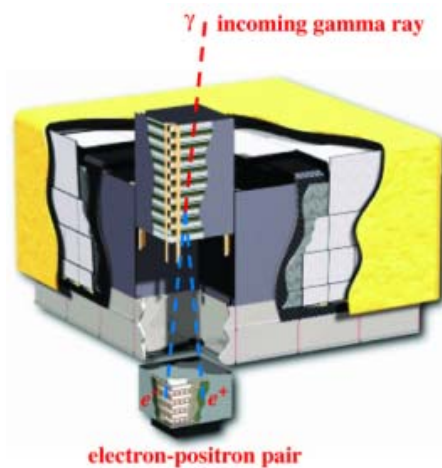
FIGURE 2.1: The schematic view of the Fermi-LAT detector [31].

2.1.3 Fermi-LAT Performance

The main characteristics of the Fermi-LAT telescope especially the selection of the background, the efficiency of algorithms for reconstructing true events etc., depend on the LAT instrument's design [31]. The LAT collaboration has presented the plots of the main properties of the LAT performance, based on the results of latest P8R2_V6 instrument response function (Fig. 2.2). One of the important characteristics is the response of the instrument to the incoming γ-ray photons, which is characterized by instrument response function. In Fig. 2.2 are presented the plot of the point spread function (PSF; upper left) of the instrument, acceptance of the instrument (upper right) and effective area for both dependence on the energy (lower left) and as a function of inclination angle at 10 GeV (lower right).

Interestingly, the improvement of the instrument response function and the latest one P8R2_V6 has significantly improved the mentioned characteristics of the Fermi-LAT instrument.
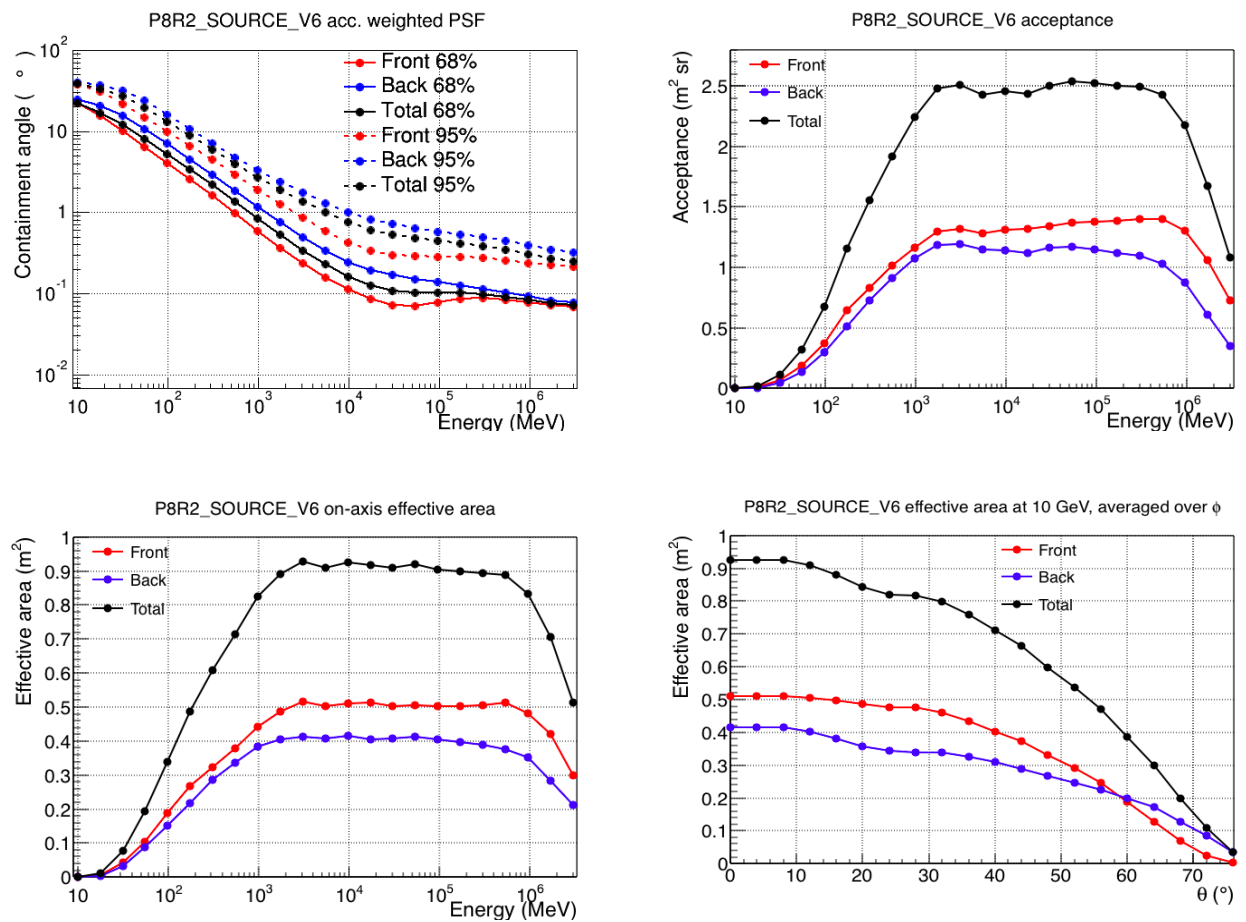
FIGURE 2.2: The plots of point Spread Function (top left), acceptance (top right) and effective area (down) respectively depend on energy and effective area as a function of inclination angle at 10 GeV are presented. Taken from [1]

After ten years of observation of the Fermi-LAT, the Point source sensitivity of the instrument is presented in Figure 2.3. The graphical view of the integral flux is created as following: performing a ten-year Fermi-LAT analysis, restoring initial energetic photons by the latest response function (P8R2_SOURCE_V6) and extracting integral flux above 100 MeV with fixed power law index equals 2 (see eg.[2]). The test statistic is higher than 5-sigma threshold.

---

[1] http://www.slac.stanford.edu/exp/glast/groups/canda/lat_Performance.htm

FIGURE 2.3: Integral flux sensitivity for a point source of Fermi-LAT (from [2]).

2.1.4 Fermi-LAT Data analysis: Binned Likelihood Data Analysis

In general, the Fermi-LAT data are analyzed using likelihood analysis method (details from [3]). The Fermi-LAT data collected since its launch (about 10 years) are available for public, which can be downloaded and analyzed. Initially depending on the exact research, there are different parameters nec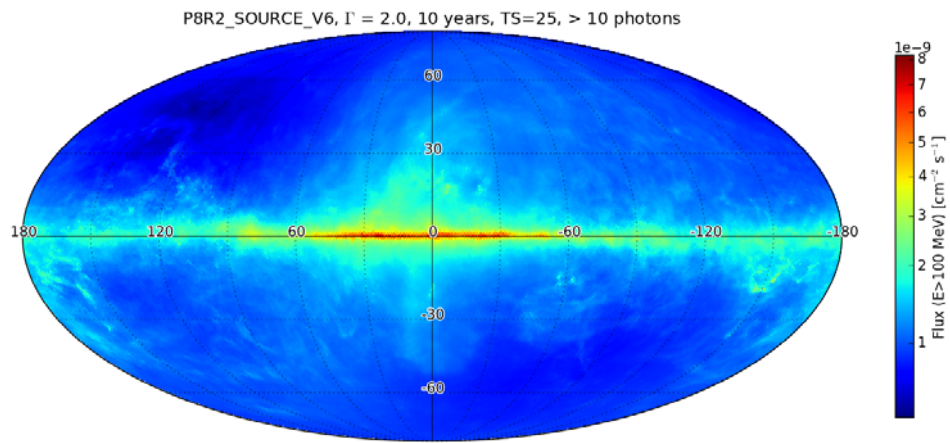essary to choose and perform data analysis. The data can be downloaded from the web[4], filling all necessary empty fields, such as coordinate, energy range, time interval and preferable region radius. Then using different tools, the data analyses is performed which is shown in Fig. 2.4. Using *gtselect* and *gtmktime* tools we perform cuts in time and energy then using filters ((*DATA_QUAL>0)&&(LAT_CONFIG==1*)), remove unnecessary events from the downloaded data. During the data selection we choose the region of interest (ROI, mainly > 12 degree) and apply it during the data filtering. At the same time START and STOP (MET) and energy rang (MeV) in the data selection are used in data filtering. As we know, the interactions of cosmic rays with the earth atmosphere produce γ-rays, which can be also detected by Fermi-LAT. Thus in order to exclude these particles from the data, rocking angle of the LAT < 52 degree and zenith angle < 90 degree cuts are selected respectively. Afterwards, using the selected ROI, we create source model file, which contains all sources around our target source of interest, with their spectral description and coordinate.

---

[2] http://www.slac.stanford.edu/exp/glast/groups/canda/lat_Performance.htm
[3] https://fermi.gsfc.nasa.gov/ssc/data/analysis/scitools/binned_likelihood_tutorial.html
[4] https://fermi.gsfc.nasa.gov/cgi-bin/ssc/LAT/LATDataQuery.cgi
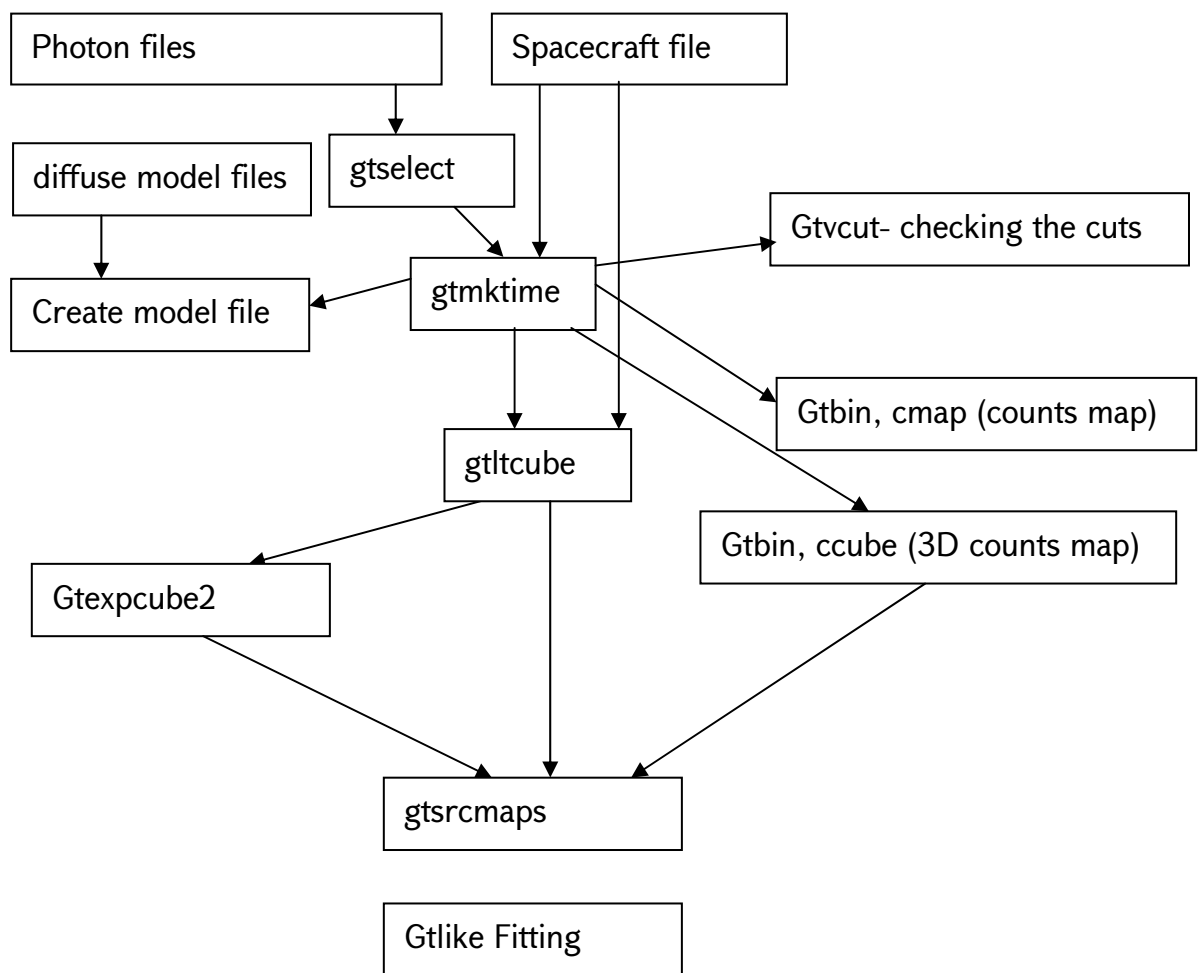
FIGURE 2.4: The descriptive chart of the Fermi-LAT binned likelihood analysis.

This model file is created based on Fermi four years source catalog (3FGL, see [5]). Additionally, to validate the precision of used cuts, the count map (cmap) is built with *Gtbin/cmap* command. By this command, two-dimensional count maps are building, which depict the brightness at each point of the chosen ROI. Then, we can import the used model ROI file on the counts map to see if the selected ROI represents the observed data. Subsequently, running next commands (*gtltcube, gtexpcube2, gtsrcmaps*), mention in the Fig. 2.4, all needed files are prepared for initiating fitting. *Gtlike* tool uses optimization methods and finds best spectral description of the ROI sources (see [6]). Before starting the fitting, the optimizers (MINUIT or NEWMINUIT) and the initial parameters (e.g., the tolerance) should be given in order to enable the efficiency of the fitting. As a result, after the fitting the best description of the source parameters included in the model file will be

---

[5] https://fermi.gsfc.nasa.gov/ssc/data/access/lat/4yr_catalog/
[6] https://fermi.gsfc.nasa.gov/ssc/data/analysis/scitools/help/gtlike.txt

obtained. For further analysis, such as deriving the spectral energy distribution and temporal variability, we use the model file from result of the fitting. These methods of analyses are used to investigate HE emission from the core region of radio galaxies.

2.2 Chandra X-ray Observatory

2.2.1 Chandra Instrument

The Chandra space telescope is one of the best instruments working in the X-ray band $(0.1-10\ keV)$ which has excellent angular resolution $(< 0.5\ arcsec)$ and wide field of view $(30' \times 30')$ (details from [32]). Chandra X-ray satellite provides X-ray images of large scale jets with their knots and hotspots structures. Operating since 1999, Chandra collected larger amount of X-ray data giving an opportunity to study the X-ray emission from different objects. The schematic view of Chandra is shown in Fig. 2.5.
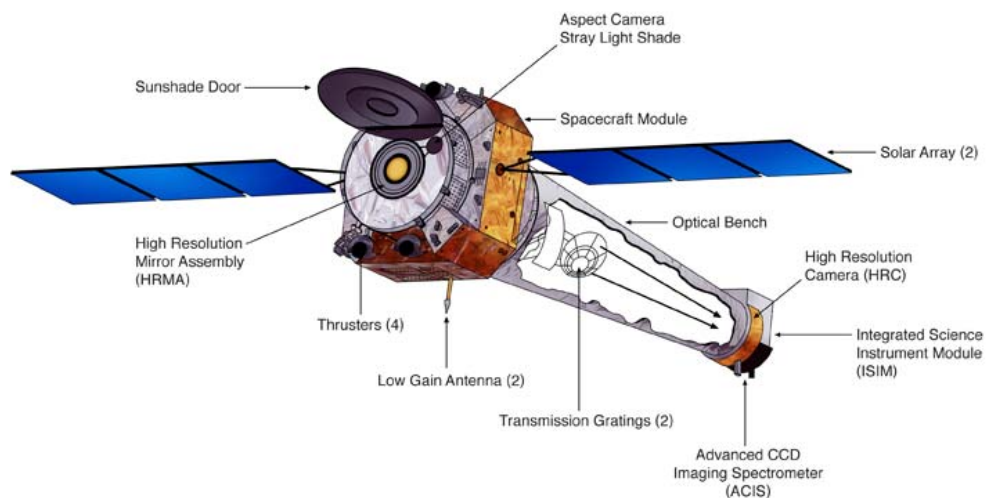

FIGURE 2.5: The schematic picture of the Chandra X-ray telescope (taken from [7]).

The main structures of Chandra instrument are presented below and details from [32]:

1) High Resolution Camera

---

[7] http://chandra.harvard.edu/resources/illustrations/craftIllustrations.html#craft3

2) Advanced CCD Imaging Spectrometer

3) High and Low Energy Transmission Gratings

The High Resolution Camera (HRC) consists of two detectors: the HRC-I and the HRC-S. The HRC-I responsible for imaging, works on the energy range $(0.06 - 10 \, keV)$ and has 30×30 arcmin field of view which is the largest aboard Chandra.

The Advanced CCD Imaging Spectrometer (ACIS) consists of two chips ACIS-S and ACIS-I and is considered as an X-ray imager, detected the incoming X-ray photon's position, energy and arrival time. The image resolution is about one arcsec, which can be used for resolving inner structures of the large scale jets. The Low Energy Transmission Grating (LETG) provides the spectral resolving at low energies $(0.07 - 0.15 \, keV)$, while the High Energy Transmission Grating (HETG) is designed for spectroscopy of bright sources in the range $0.4 - 10 \, keV$. Detectors are owned a high resolution, e.g. HETG clearly resolve the emission lines from O to Fe-K and LETG used to study the bright sources in the universe. Almost all characteristics (energy, position, quantity, and time) of detected X-ray photons are identified from the cooperative working on the ACIS and HRC. As regards HETG and LETG, these are designed to arrange diffracted X-ray photons [32].

The important part of the spacecraft is science instrument module (SIM), which is composed of adjustable detectors [32]. The ACIS and the HRC are the constituent parts of the SIM. The SIM moves in both the X-axis and the Z-axis and the schematic view of the arrangements of ACIS-I, ACIS-S, HRC-I, HRC-S are shown in Fig. 2.6.

The structural ground of Advanced CCD Imaging Spectrometer is the charged coupled device (CCD). Chandra has two CCD detectors, front- and back-illuminated. Due to flexible semiconductor structure, the CCD's Chandra detector has permissible advantages. For instance, the high-level quantum efficiency permits to distinguish successfully X-ray photons, with their direction, arrival time and energy [32]. Furthermore, the distinctive structure of X-ray detectors such as CCD can intensively detect X-ray photons and

simultaneously obstruct optical photons, using special filters. And more detailed information about it can be found at the Proposer's Observatory Guide[8] and in [32].
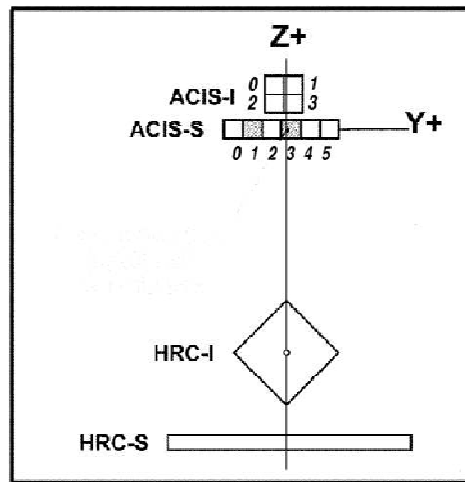
FIGURE 2.6: The schematic view of Science Instrument Module (SIM) (from [32]).

2.2.2 Detecting X-ray technique

X-ray telescopes depending on their main scientific purposes have different structures. In contrast to optical telescopes, where the light can be detected by focusing the optical lenses, in the case of more energetic X-ray photons the detection mechanisms are different. In order to focus the X-ray photons into the detector and detect them, an optical bench is used as a basic structure of the Chandra telescope which redirect energetic incoming photons. The case of Chandra telescope the optical bench (length about 10 meters) is designed guided by Wolter type 1 configuration [32].
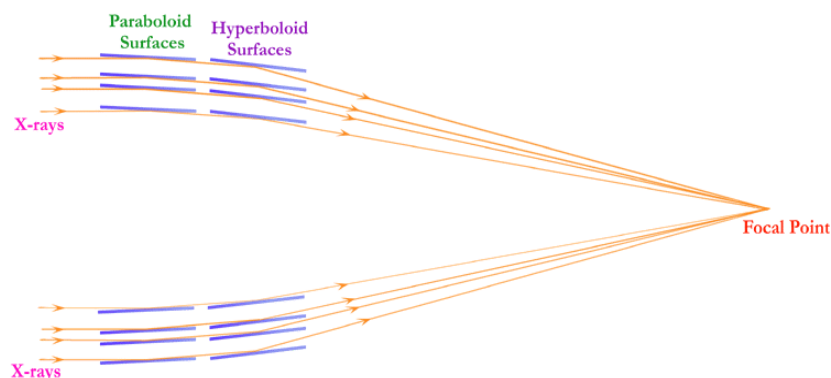
FIGURE 2.7: Grazing incident effect with the support of the mirrors (taken from [9]).

Specially designed and skillfully polished mirrors are used inside the optical bench being composed of four pairs of hyperbolic and parabolic mirrors. Thereby, such reasonable structures compel the X-ray photons to change their orientation at a very tiny angle ("grazing incidence", see Fig. 2.7) and collect photons on the detector.

2.2.3 The performance

Chandra telescope is endowed with several detection characteristics, which primarily depend on several effects, such us geometrical reflectivity of mirrors, vignetting, CCD quantum efficiency etc. of the instrument [32]. The effective area is one of the important properties of X-ray telescopes and for Chandra it is about 800 cm^2 and it is shown in Fig. 2.8 depending on the energy (detailes from [10]).
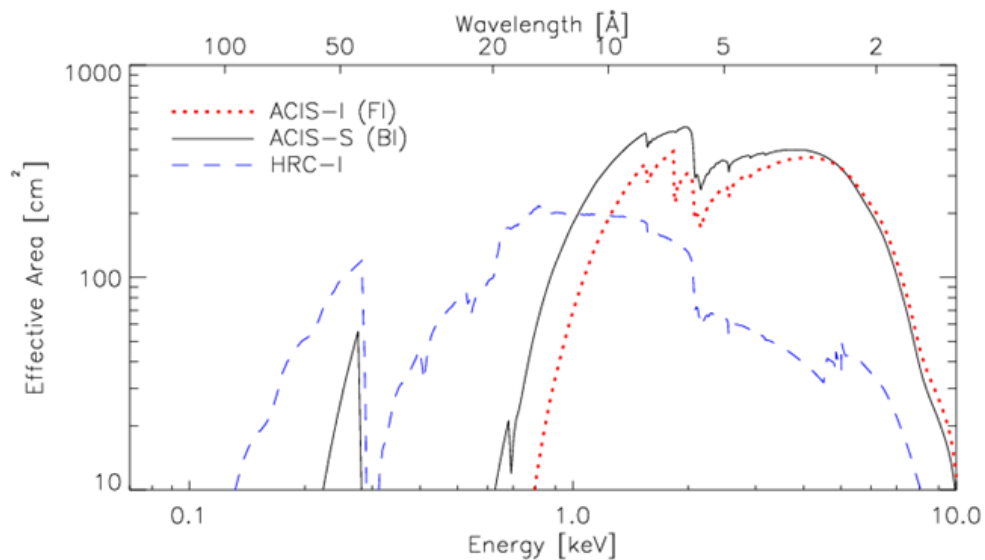
FIGURE 2.8: Effective area as function of energy (from [10])

Another improved feature of the Chandra X-ray telescope is its exceptional angular resolution, which is 0.5 arcsec [32]. This kind of improved angular resolution allowed to study the large scale structure of AGN's as well as distinguish the structures of different components.

2.2.4 Chandra Data Analysis. CIAO

For analyzing Chandra X-ray data, we use Chandra Interactive Analysis of Observations (CIAO) 4.8 software package with Chandra Calibration Database (CALDB) version 4.7.2 [11]. In general, Chandra data analysis consists of several parts, depending on the target and the type of observation. Here are presented the main commands and tools, which are used during the X-ray data analysis.

*download_chandra_obsid* – For starting data analysis, all necessary data are downloaded from Chandra data archive. Filling the source name or coordinate, the Level 1 unprocessed files can be obtained. For more details see [12].

chandra_repro – By this command, we can filter Level 1 data and get rid of unnecessary events (details see in [13]). This tool includes various parameters, which can be chosen depending on the observation. As recommended from the Chandra Team before the data analyses it is recommended to use chandra_repro command, which automatically applies filters and reprocesses Level 2 files more effectively.

After creating level 2 files, we have to check background flares and readout streak [14]. It is common in the case of bright sources. Initially, we build background light curve and estimate background counts/rate threshold. Before starting our spectral and spatial analysis, with the help of lc_clean command we can remove background anomalous effects. It is also essential to handle the readout streak when photons are detected in the wrong row during the readout[15].

The next step, for extracting spectra, we need to choose source and background regions. Opening filtered level 2 event file on the platform of *SAOImage ds9* application[16], we can choose from the image the backgrounds and source regions.

Specextract [17] – Both in extended and point like source cases we use this command for extracting spectrum. We can create spectrum step by step, but this tool automatically

---

[11] http://cxc.cfa.harvard.edu/ciao/

[12] http://cda.harvard.edu/chaser/

[13] http://cxc.harvard.edu/ciao/ahelp/chandra_repro.html

[14] http://cxc.harvard.edu/ciao/threads/flare/

[15] http://cxc.harvard.edu/ciao/threads/acisreadcorr/

[16] http://ds9.si.edu/site/Home.html

accomplishes the task, giving us both source and background spectrum with appropriate corrected Response Matrix Files (RMFs) and Ancillary Response Files (ARFs). The output of this tool we use for future spectral fit. Basically, each selected target (source) has several observations explored in different time scales.

In order to study the source spectrum more detailed and obtain more accurate results of the fitting, we combine spectra or doing simultaneously fitting. For each source, the *combine_spectra*[18] script sums all observations PHA spectra obtained in different time scales, as well as the associated background PHA spectra and source and background ARF and RMF response files are also combined. The further analyses to obtain the spectra are performed with Sherpa[19]. As refer to the *simultaneously fitting*[20], the Sherpa programming language allows us to simultaneously import all spectra for each observation and to make further fit.

---

[17] http://cxc.harvard.edu/ciao/ahelp/specextract.html
[18] http://cxc.harvard.edu/ciao/ahelp/combine_spectra.html
[19] http://cxc.harvard.edu/sherpa/
[20] http://cxc.harvard.edu/sherpa/threads/simultaneous/

Chapter 3

3C 120 JET EMISSION AT SMALL AND LARGE SCALES

3.1 Introduction: Structure of 3C 120 jet.

The broad line radiogalaxy (BLRG) 3C 120, due to its peculiarity, has been extensively studied at all wavelengths. Following Fanaroff-Riley Classification (FR, [6]) generally used to study of the morphology of radio galaxies, BLRG 3C 120 have FRI types morphology. 3C 120 is a Seyfert 1 spiral galaxy, and the spectroscopic observations with Lick Observatory (120-inch telescope) show its distance to be z=0.033 (140 Mpc) [33]. The reverberation-mapping techniques, such as spectroscopic monitoring of the variations of Hβ emission lines, have determined the mass of black hole in 3C 120 to be $(5.7 \pm 2.7) \times 10^7 M_\odot$ [34].

The observations in the radio wavelengths indicate the existence of one-sided polarized radio jet, and 3C 120 is a prime candidate for exploring the physics of relativistic jets with a linear size extending from 0.5 pc to 100 kpc [35]. Furthermore, the observations of superluminal motion with $\beta_{app} = 8.1$ [9] indicate that the inclination angle to the line of sight is limited by $< 14°$ [36]. Another radio observation, allowed to investigate the very inner jet structure of the 3C 120 at 15, 22, 43 GHz wavelengths, detecting relativistic components with velocities up to 4-6c [37,38]. Studying the kpc scale jet of 3C 120 have shown relatively slowly moving cool medium, which confirms the existence of the helical jet structure [39]. This kind of jets characteristics, e.g. different superluminal components and the helical jet structure can be explained as the result of jet precession [40].

Deep observations with Hubble Space Telescope (HST) analyzed by applying a two-dimensional model to create HST images [41], broad emission lines and several diffuse stellar remnants around the central kiloparsec have been found, which may denote a past merging process.

In X-rays, 3C 120 is a bright ($\approx 5 \times 10^{-11} \mathrm{erg\,cm^{-2}s^{-1}}$ at 2–10 keV) and variable source on time scales from days to months [42]. The ASCA observation shows a broad iron line Kα that can be fitted by Gaussian with σ = 0.8 keV and equivalent width of 400 eV. Recently, using X-ray and radio observations, [43] found that the dips in the X-ray emission are followed by ejections of bright superluminal knots in the radio jet, which clearly establishes an accretion-disk-jet connection. The kpc-scale jet of 3C 120 has a complex structure with several knots, k4, k7, s2, s3, and k25 (see Fig. 2 of [9], where on the 1.6 GHz radio contours the section of the jet with knot labels is shown), detected in the radio, optical, and X-ray bands [9]. The knots are labeled by their distance from the core in arcseconds (e.g., k4, k7) and the smooth sections of the jet detected in the optical band [44] are labeled as s2 and s3. These knots appeared to have interesting morphology and spectra more tricky among which is the X-ray emission from the knot k25: it has a very weak radio flux but it is bright in the X-ray band [9]. It is a real challenge for one-zone synchrotron emission scenario to interpret the emission from k25 in case of which large deviation from the minimal energy condition is required. It has been suggested that X-rays might be produced through the synchrotron radiation of an electron population distinct from that responsible for the radio emission [9]. Alternative theories such as proton synchrotron emission [27] or Inverse-Compton scattering of CMB photons [45] have also been proposed. However, it is to date not clear which is the exact mechanism responsible for the X-ray emission.

At high energies (HE; $> 100\,MeV$) the source was not detected with the energetic γ-ray experiment telescope on board the Compton Gamma Ray Observatory, despite several pointing observations and 2σ upper limit on the source flux above 100 MeV was set to $9 \times 10^{-8} cm^{-2} s^{-1}$ [46]. Afterwards, the source was detected with the Fermi-LAT using 15 months of all-sky exposures and the averaged HE spectrum between 100 MeV and 1 GeV can be described by the power law with photon index $\Gamma = 2.71 \pm 0.35$ and an integral flux $F_{E > 100\,MeV} = (2.9 \pm 1.7) \times 10^{-8} cm^{-2} s^{-1}$ with the detection significance of 5.6σ [47]. However, the source is not included in the *Fermi*-LAT second source catalog ([48], 2FGL) since the averaged signal appeared to be below the required 5σ threshold. This might be evidence of the long-term variability of the flux, since for a steady γ-ray signal the

accumulation of longer data set (24 versus 15 months) should result in an increase of the detection significance $\approx \sqrt{24/15} \times 5.6\sigma$. [47] and [48] investigated the temporal variations of the γ-ray flux (above 100 MeV) over short timescales. The light curve binned in three-month-long periods shows only a few episodes when the flux increased on a level more than 3σ. One such episode occurred during the 15-month data set [47] and two occurred during the 24-month data set [49]. The rest of the time, the source was undetectable by *Fermi*-LAT. This was interpreted as a GeV flux variation on 90-day scales. However, considering only two periods out of eight have been detected and taking trials into account, post-trial significance probably is even lower than 3σ. Therefore, these conclusions were inconclusive considering the limited statistics of the detected signal. Also a long-term (several months) variability had been found using the five-year Fermi-LAT data [16] with short periods (days and hours) of brightening [16,17]. Inverse Compton scattering of synchrotron photons seems to be the mechanism responsible for the γ-ray emission from 3C 120 [16,17] while the flares and the fast γ-ray variability are explained within more complex structured jet scenarios [18,19,49].

Combining of the data derived at the sub-pc and kilo-parsec regions of the same jet could greatly help to understand the features of powerful extragalactic jets, e.g., shed some light on the evolution and propagation of the jets from the central engine to the outer regions, where the jet is starting to significantly decelerate [19]. This approach can be fruitfully applied to the sources showing a large-scale jet long enough to be resolved by Chandra. Unfortunately, the best-studied blazars do not tend to have well-studied large-scale jets, precisely because the blazars are most closely aligned with the line of sight, reducing the projected angular dimension of the large-scale jet. Thus, only a few jets can be studied on both scales [20]. The prominent features of 3C 120, e.g., the strong jet well resolved in both small (pc) and large (kpc) scales makes this object an ideal target for investigation of the processes occurring in the powerful jet along its propagation, this is why the emission from this particular source is discussed in details here [16,18,19].

3.2 Swift XRT/UVOT observation of nuclear region

As a first step, the emission from the jet of 3C 120 near the nucleus is investigated. Initially, the data from Swift telescope are analyzed. The Swift satellite [50] operates since 2007 and has been observing 3C 120 periodically. Interestingly Swift satellite observed 3C 120 in its γ-ray quiescent and active states. As the X-ray flux varies as well (see www.bu.edu/blazars/VLBA_GLAS T/3c120.html), we have selected the observations made on MJD 55252.70 and MJD 55800.25 when the X-ray flux also was low. During the γ-ray active state 3C 120 was observed only three times, on MJD 56934.19, MJD 56937.70 and MJD 56938.50. The data from two of the instruments on board Swift, the Ultraviolet and Optical Telescope (UVOT) and the X-Ray Telescope (XRT) have been used in the analysis.

3.2.2 Swift XRT

The Swift-XRT observations were made in the photon counting (PC) (Obsid 37594002, 37594004) and windowed timing (WT) (Obsid 37594042, 37594048, 37594049) modes. The data extraction and analysis have been done using HEASoft package (v.6.21) correspondingly XRTDAS software package (v.3.3.0). We define source and background region using DS9 program, shown in the Fig. 3.1. The source circular region centered at the 3C 120 radiogalaxy, with a radius of 30 pixels ($\sim$ 71") and background region is an annulus: the inner and outer radius being 80 ($\sim$ 190") and 120 pixels ($\sim$ 280") respectively again centered at the source. For the PC-mode observation (37594004), the count rate was > 0.5 count/s being affected by the piling up in the inner part of the PSF. This effect was removed by excluding the events within a 4-pixel radius circle centered on the source position. Then, using xrtmkarf task, ancillary response files were generated by applying corrections for the PSF losses and CCD defects. Considering the number of detected counts it is necessary to rebin assuming minimum 20 counts per bin. Then the bad channels are ignored applying energy cut below $0.5\,\mathrm{keV}$.

The spectrum is well fitted using XSPEC v12.9.1a X-ray spectral fitting package. The results of the fit are presented in Table 3.1 and the energy spectrum is shown in Fig. 3.13 and 3.14. The absorbed power-law spectral model describes well the energy spectrum in the

0.5-6.0 keV energy range. The column density is $N_H = 1.06 \times 10^{21}\,cm^{-2}$ taken from LAB [51]. Although the X-ray flux did not increase significantly (the highest flux of $F_{(0.5-6)keV} \simeq (6.73 \pm 0.15) \times 10^{-11} erg\,cm^{-2}s^{-1}$ observed on October 4, 2014, exceeds the lowest one ~ 2.8 times), the X-ray photon index softened, changing in the range of $\Gamma_x = (1.76 - 1.80)$ during the bright γ-ray periods.

Table 3.1: The Swift XRT analysis results			
Obsid	Γ_X MJD	νF_ν $\times 10^{-11} erg\,cm^{-2}s^{-1}$	reduced χ^2
37594002	1.42±0.07	4.27±0.18	0.43
37594004	1.53±0.08	2.41±0.11	0.75
37594042	1.76±0.04	6.73±0.15	1.21
37594048	1.72±0.04	5.37±0.12	1.05
37594049	1.80±0.06	3.73±0.13	0.86
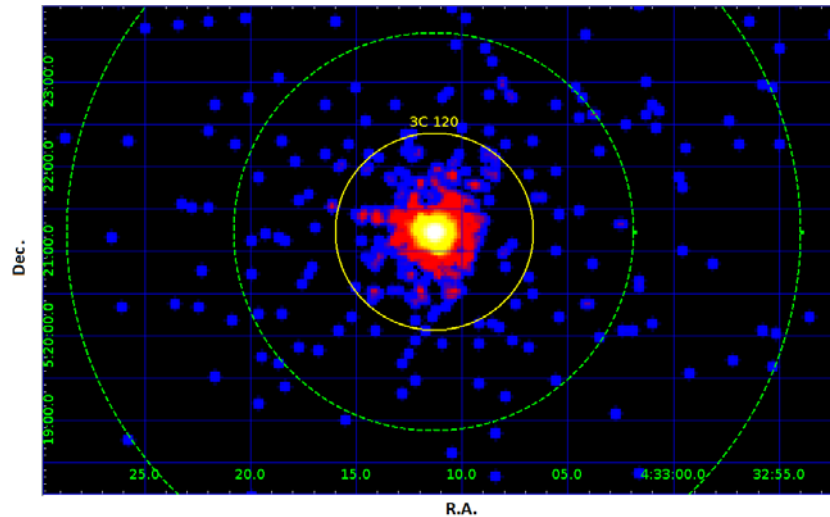
FIGURE 3.1: The Swift PC mode observation (Obsid 37594002). The yellow circle is source region and dashed green annulus is the background region respectively.

3.2.3 Swift UVOT

Analyzing Swift UVOT data gives an opportunity to study the multi-wavelength emission from 3C 120 jet. Observing simultaneously with the XRT, the UVOT allows us to study the source in the optical range (170-650 nm) covering $17' \times 17'$ field.

In the analysis of the Swift UVOT data, the source and background regions were chosen as circular regions as shown in Fig. 3.2. The source region corresponds to $5.0''$ circle (yellow

solid) and background region 20″ circle (yellow dashed) which does not contain any neighboring source.

The magnitudes were computed using the *uvotsource* tool (HEASOFT v6.21), corrected for extinction according to [52] using $E(B-V) = 0.256$ from [53] and zero points from [54] and converted to fluxes following [55]. The corresponding spectra are shown in Fig. 3.13/3.14. The optical-UV data points harden during the flaring periods.
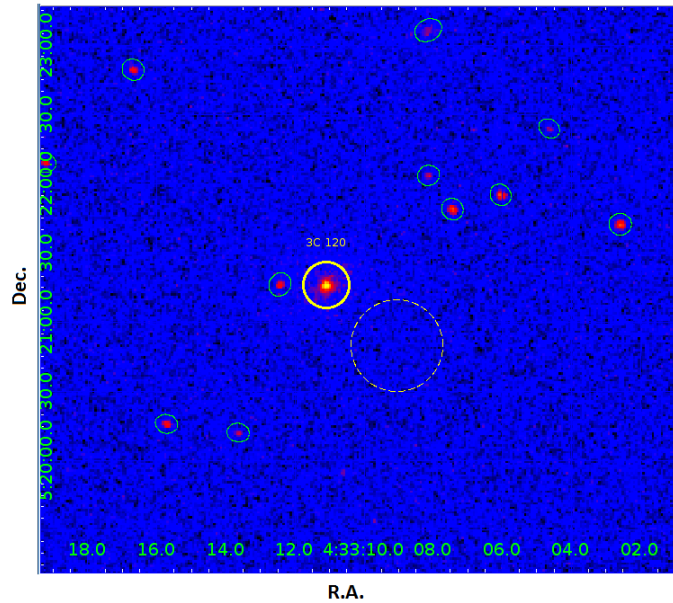
FIGURE 3.2: Swift UVOT count map with the mentioned source (yellow) and background (yellow dashed) and other sources within selected region are also circled (green).

3.3 γ-ray observation of nuclear region

3.3.1 Data Extraction

The γ-ray emission from 3C 120 was investigated considering three different periods for the analyses

i)   The first period: the Fermi-LAT ∼ 5.3 year data (from 4th August 2008 to 4th December 2013, correspondingly (MET 239557417–407808003)) in the energy range from 100 MeV to 100 GeV were analyzed.

ii)   The second period using the 7 year accumulated data accumulated up to 4th August 2015

iii)   The third and most complete study was using Fermi-LAT data collected during eight years (up to August 8, 2016 (MET 239557417-460339204)).

Here are the results from the analyses performed in the third period. We have performed binned maximum likelihood analysis following the section 2.1.4. Due to low statistics, the observations, 3C 120 is not included in Fermi-LAT four years Point Source Catalog. We manually added on the model file a new source on the known coordinates of (RA, dec) = (68.296, 5.354) [56]. The ROI with the sources included in the ROI 3FGL is shown in Fig. 3.3. The background is modeled using diffuse background model (gll_iem_v05_rev1.fits) and isotropic γ-ray background (iso_source_v05.fits).
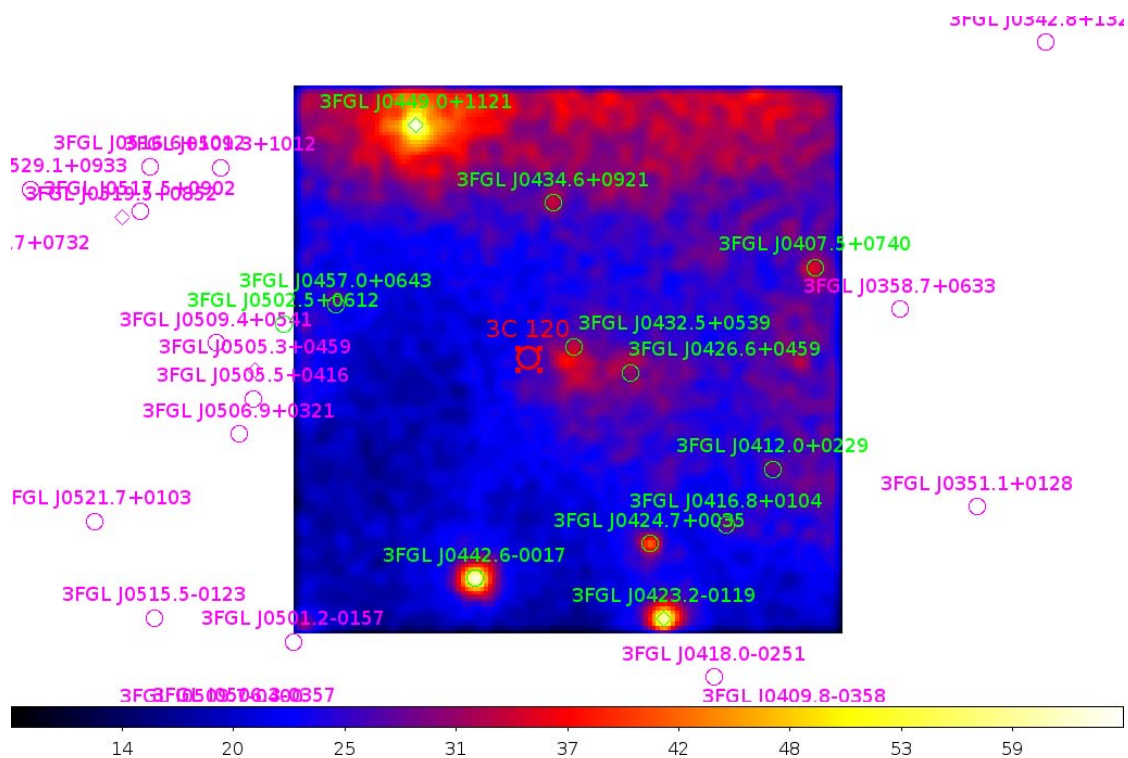
FIGURE 3.3: Count map of 3C 120 with the included sources.

Since the Fermi-LAT third catalog was created based on four-year Fermi-LAT observations and here we are using data from the longer observations, it is necessary to check if there are new sources in the ROI, which are not taken into account. The TS map was created using *gttsmap* tool and as a result no sources with >5σ have been found. In addition, we checked the source localization with *gtfindsrc* tool which resulted to R.A. = 68.205, decl. = 5.38 with a 95% confidence level. This coordinated are shifted only by 0.09 from the VLBI radio position of 3C 120 (R.A. = 68.296, decl. = 5.354) [56].

3.3.2 Spectral Analysis

During the binned Likelihood analysis, the γ-ray emission from each ROI source is model with the same spectra as in the catalog and it the case of 3C 120 we assumed power-law model in the form

$$\frac{dN}{dE} = N_0 \left(\frac{E}{E_0}\right)^{-\alpha} cm^{-2}s^{-1}MeV^{-1} \tag{3.1}$$

Where the normalization (N_0) and the power-law index (α) were left as free parameters during the likelihood analysis.

Below we present the results from the analyses of Fermi-LAT data accumulated in different periods.

1) For the first 5.3 years' data [16], the best-fit power-law parameters for 3C 120 are

$$\left(\frac{dN}{dE}\right)_P = (4.06 \pm 1.0) \times 10^{-10} \left(\frac{E}{100\ MeV}\right)^{-2.72 \pm 0.1} \tag{3.2}$$

The integrated flux above 100 MeV is $F = (2.35 \pm 0.5) \times 10^{-8}\ photon\ cm^{-2}s^{-1}$, and the TS = 76.3 (8.7$\sigma$). The obtained results are comparable with the parameters found in [47], namely photon index $\Gamma = 2.71 \pm 0.35$ and integral flux $F = (2.9 \pm 1.7) \times 10^{-8}$ photon cm^{-2}s^{-1} above 100 MeV.
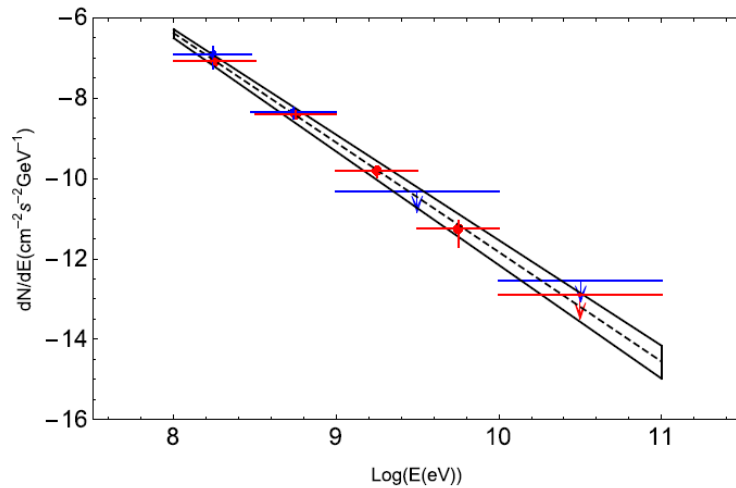
FIGURE 3.4: The averaged differential spectrum of 3C 120 at 0.1-100 GeV energy range compared with the one based on the initial 15-month data set [47]. The dashed black line shows the best power-law fit result determined from the *gtlike*.

In order to obtain the spectrum, from 100 MeV to 100 GeV energy range was divided into 5 logarithmically equal bins and analyzed each of them with gtlike tool. The spectral energy distributions of 3C 120 are shown in the Fig. 3.4 as compared with the previous study of 3C 120 [47].

2) In Fig. 3.5 is shown the 7-years averaged spectra as compared with the flares on 21-27 September 2014 (Flare 1) and on 20-26 April 2015 (Flare 2) [18]. The corresponding parameters are given in the Table 3.2.

TABLE 3.2: The results of the spectral analysis, for the whole period (7 year) and Flare 1, 2

	N_0 $\times 10^{-12}$	α	Integral Flux $\times 10^7$ photon cm^{-2} s^{-1}	TS
7 year	1.179 ± 0.038	2.69 ± 0.05	0.412 ± 0.05	334
Flare 1	17.44 ± 3.8	2.38 ± 0.15	3.05 ± 0.59	80.9
Flare 2	30.3 ± 7.2	2.25 ± 0.12	4.28 ± 1.2	112

The results show that the obtained spectra for the long time are similar with the ones obtained using 5.3 year data [16], namely $\alpha = 2.69 \pm 0.05$ and integral flux $(4.12 \pm 0.5) \times 10^{-8}$ $photon\, cm^{-2}\, s^{-1}$ above 100 MeV with a detection significance of $TS = 334\ (\approx 18.27\sigma)$. As one can see from the Table 3.2 during the flaring periods, the flux increases up to $(4.28 \pm 1.2) \times 10^{-7}$ $photon\, cm^{-2}\, s^{-1}$ and the photon indexes harden $\alpha = 2.25 \pm 0.12$. These kinds of changes indicate as effective particles acceleration during the flare periods and the particle radiation mechanisms are discussed in Section 3.5.1.
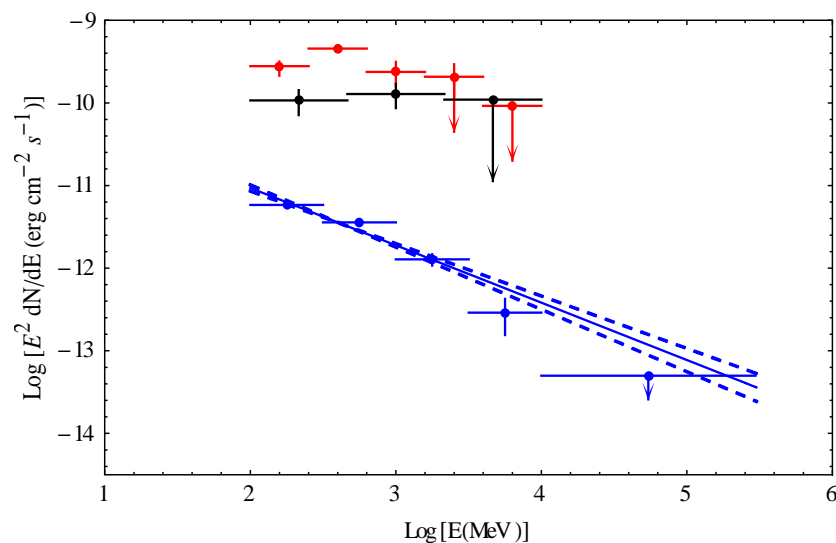
FIGURE 3.5: The averaged differential spectrum of 3C 120 (above 100 MeV) for the period 4th August 2008 - 4th August 2015 (blue points). Black and red points are the spectra of Flare 1 and Flare 2 respectively.

3.3.3 Temporal Variability

The variability of the observed γ-ray flux contains valuable information on the emitting region(s) size. The emitting region size can be estimated from the relation $R/\delta < c\tau/(1 + z)$, where δ is the Doppler factor and z is the redshift. In order to create γ-ray light curve the time period is divided into different time bins and unbinned likelihood analysis is performed. In the model file in order to decrease the uncertainties in the flux estimation, the photon indices of all ROI sources were fixed to the best guess values obtained in full time analysis. The index of 3C 120 initially was considered as a free parameter then also fixed. In addition, the normalizations of both background components were fixed; since no variability is expected from background components.

Initially the variability was investigated using Fermi-LAT data collected during initial five years' data [16]. In this data set the statistics allowed to investigate the variability only in long periods, e.g., dividing into 180- and 365- days bins, shown in red and blue points respectively in Fig. 3.6.

It can be noticed that after 56000 MJD the γ-ray flux sufficiently increased more than twise as compared with its average level (see Fig. 3.6). The highest test statistics for 365 days' bins corresponds to TS = 63.8 and for 180- day sampling TS = 38.92.
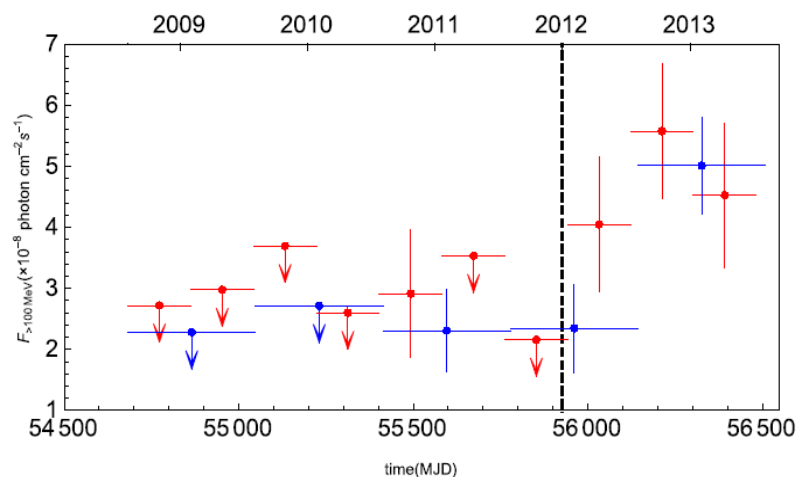
FIGURE 3.6: γ-ray light curve from August 4th 2008 to December 4th 2013. The bin size corresponds to 180- (red) and 365- days (blue).

The variability is studied using the data accumulated for longer periods [18]. Using seven years of Fermi-LAT data provides larger photon statistics. The light curve is generated for

the energy range 100 MeV - 300 GeV and for the whole time by dividing correspondingly in 90-days periods (Fig. 3.7).
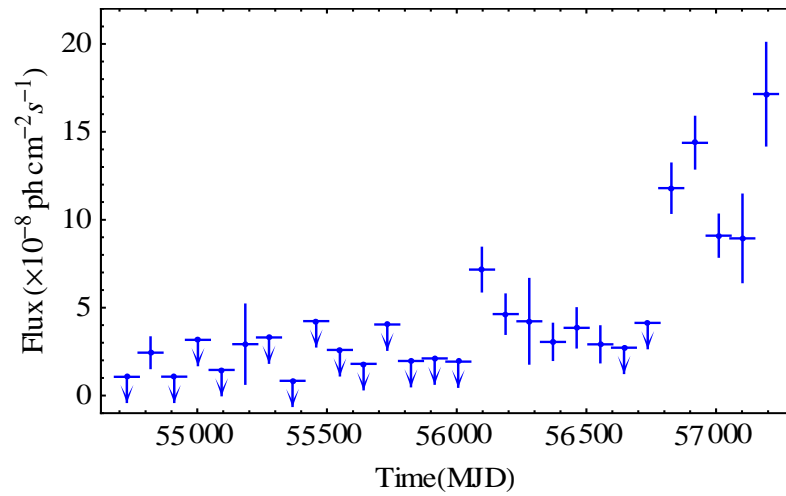
FIGURE 3.7: γ-ray light curve from August 4th, 2008 - 2015. The bin size is 90 days.

Similarly, to previous result [16] it is noticed that after ≈ 55400 MJD the $\gamma - ray$ emission from 3C 120 has increased. Furthermore, in order to study the temporal variability in shorter time scales the active period (56000 – 57238 MJD) was separated. The separated region was divided into week time scales and unbinned likelihood analysis was performed for studying light curve for shorter time period. The result is shown in Fig. 3.8. It is noticeable flux temporal variation for 7-days sampling. Furthermore, in two periods the fluxes increased significantly.
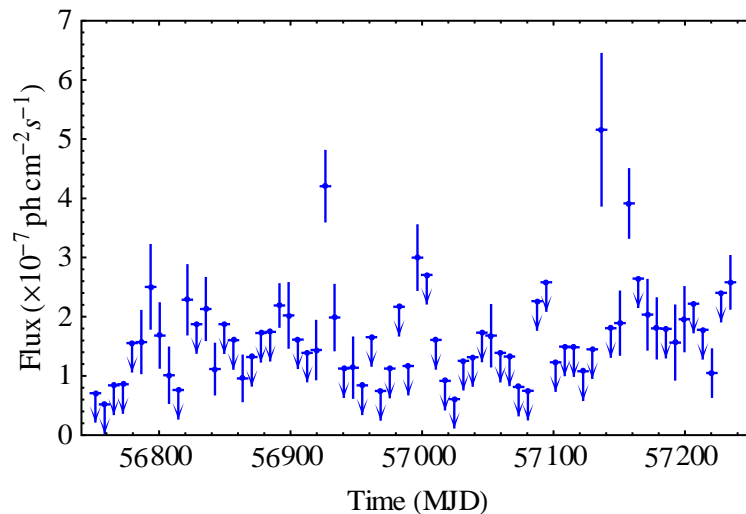
FIGURE 3.8: The light curve with one week binning.

i)   Flare 1 - (21-27 September 2014), the integral flux was $(3.05 \pm 0.59) \times 10^{-7}$ $photon\ cm^{-2}\ s^{-1}$ with the 10.58σ detection significance.

ii)   Flare 2 - (20-26 April 2015) the flux was $(4.28 \pm 1.12) \times 10^{-7}\ photon\ cm^{-2}\ s^{-1}$ and detection significance equals to the 8.9σ.

The spectra during the selected periods were estimated using the unbinned likelihood analysis. The results show that the flux increased approximately 7-10 times compared to its average level and photon indices were noticeably hardened, e.g., for the first flare it had changed from 2.69 to 2.38 and for the second flare to 2.25, respectively. The spectral energy distribution and the results of those analyses are presented in the Fig. 3.5 and Table 3.2, respectively.

In order to investigate the variability of 3C 120 jet emission in the γ-ray band, new method was used [19]. Initially the considered 8-years were divided into 90 day intervals. The light curve obtained for 90-day binning is shown in the upper panel of Fig. 3.9.
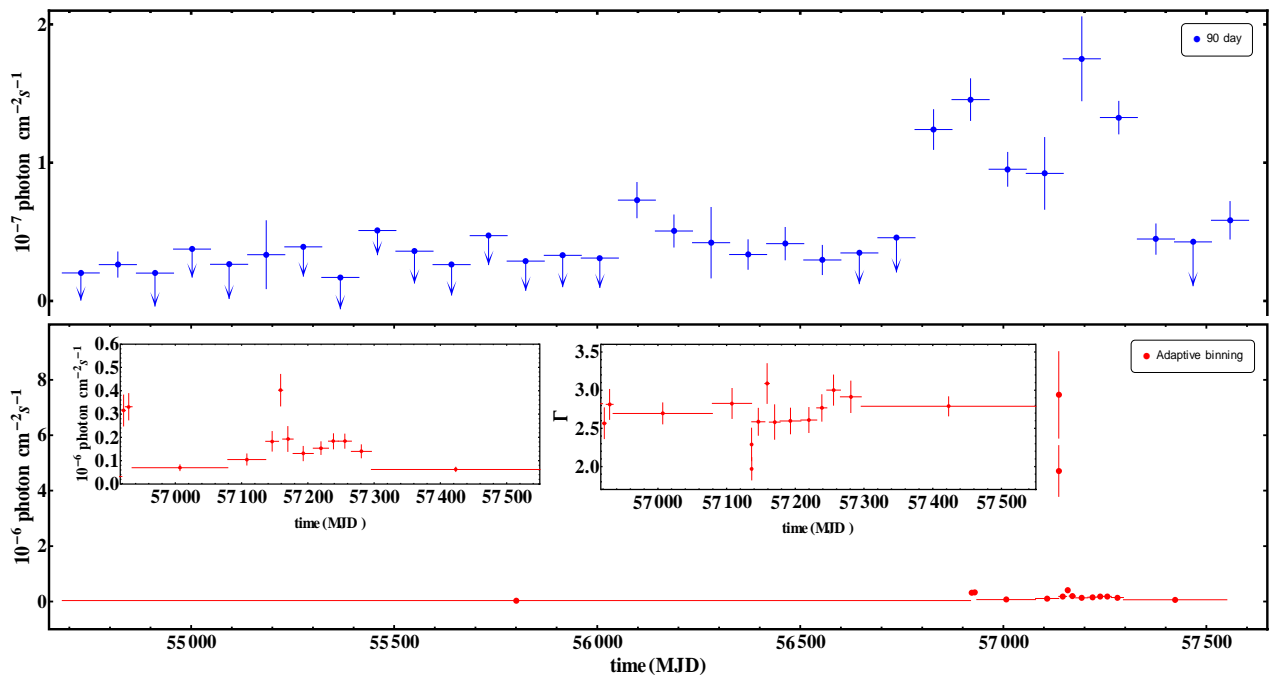
FIGURE 3.9: The γ-ray light curve of 3C 120 from August 4, 2008, to August 4, 2016. (a) The bin intervals correspond to 90 days. (b) The light curve obtained by adaptive binning method assuming 20 % of uncertainty. The change of photon index is shown in the insert.

Before ≈ MJD 56000 (March 14, 2012), the source is mostly undetectable by Fermi-LAT: only in two of the total 15 cases, the source detection significance exceeded the required threshold of 4σ. Then the source flux was high enough to be detected by Fermi-LAT, and up

to ≈ MJD 56800 it remained constant with no significant changes. Starting from ≈ MJD 56800, the flux substantially increased up to a few times $10^{-7} photon\ cm^{-2}\ s^{-1}$ and remained so until ≈ MJD 57350. The standard χ^2 analysis revealed a highly variable γ-ray flux, where the probability of the flux to be constant is $p(\chi^2) << 5\%$.

Table 3.3: Result of Fermi-LAT γ-ray data analysis, appropriately for the active and quiescent states.

date	Flux ($10^{-8} photon\ cm^{-2}\ s^{-1}$)	Γ	TS
2008/08/04-2014/09/19	2.87 ± 0.49	2.79 ± 0.08	179.43
2014/09/19-2014/10/04	24.9 ± 4.21	2.57 ± 0.16	90.5

In order to investigate the emission from 3C 120 in its quiet and active states, the γ-ray spectra were extracted from the following periods:

1) Long quiescent states, namely, between MJD 54682.65 and MJD 56919.31

2) The active state after MJD 56919.31

The period overlaps with the Swift observations on MJD 56934.19, 56937.70 and 5638.50. Although the Swift observation lasted several thousands of seconds, in order to increase the γ-ray photon statistics, the Fermi-LAT spectrum was extracted from 15 days (MJD 56919.31-56934.76), when the source showed a comparable flux level as inferred from the light curve obtained by an adaptive binning method.

The spectrum of 3C 120 was modeled as a power-law function ($dN/dE \sim N_0 E^{-\Gamma}$) with the normalization and index considered as free parameters. In order to find the best matches between the spectral models and events, a binned likelihood analysis is performed with gtlike for the first period, while an unbinned analysis was applied for the second one. The spectral fitting results are summarized in Table 3.3 and the plots of the SEDs are shown in Fig. 3.13 and 3.14. During the flaring periods, the γ-ray flux increased nearly by an order of magnitude and the photon index hardened.

3.4 X-ray observation of 3C 120 jet knots

As it was discussed above, the 3C 120 jet has peculiar X-ray structure, especially the extended X-ray knotty jet [19]. The Chandra X-ray telescope, due to its relatively good

resolution, was able to resolve and detect the X-ray emission from the jet of 3C 120. Since 2001 Chandra X-ray telescope observed 3C 120 more than 5 times and have the total observation time 251.86 ksec. Each observation id number, mission start date and the exposure time (in ksec) are presented in Table 3.4.

id	time	Exposure(ksec)
	Table 3.4: 120 Chandra X-ray observations.	
3015	2001-12-21 10:58:56	57.22
16221	2014-12-19 07:13:46	77.72
17564	2014-12-22 23:04:19	30.29
17565	2014-12-27 05:38:06	43.31
17576	2015-01-27 23:00:36	43.32

Initially, the regions of the knots and corresponding background are selected. The following knots k4, k7, s2, s3 and K25 region consists of sub-knots (inner, outer and new) were selected and further analyzed. This knots shape and coordinate selection is the same as in [9]. The Chandra X-ray image overlaid with the radio contour and the positions and shapes are shown in Fig. 3.10. The radio contours are from the VLA at 5 GHz radio observations [57]. The X-ray image was filtered from unnecessary noise using Gaussian smooth filter. Then the X-ray analysis is performed for the selected regions.
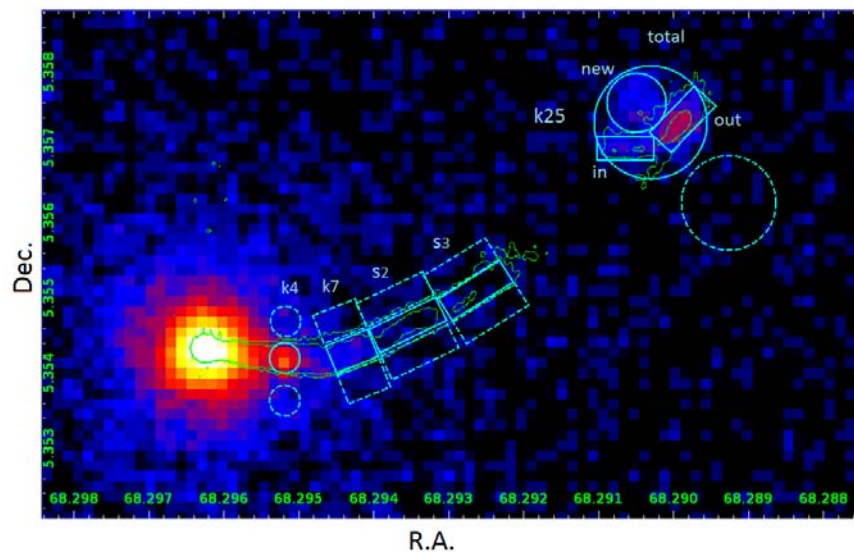
FIGURE 3.10: The count map of 3C 120 shown with 5 GHz with radio contour (Green). Source and background regions (green) are depicted on the picture solid and dashed lines respectively.

The data reduction and data analyses were done following the steps presented in the section 2.2.4. The background anomalous effect and flares have checked by *lc_clean* command and the background of 3C 120 was not affected any significant flares. The readout streaks were removed for each observation and the events files were then reprojected to a single physical coordinate system (using observation 16221 as a reference). In addition, to reduce the uncertainties caused by the position offsets of different observations, we made astrometric corrections. Furthermore, the spectral fit has been done with Sherpa[21]. We extracted the spectra and created weighted response files for each observation, using the *specextract* script. The knots spectra were rebinned using a different count threshold depending on the total number of counts, and fitted in the 0.5-10 keV energy range using a power-law with the Galactic absorption model (column density fixed at $N_H = 1.06 \times 10^{21} \, cm^{-2}$), where the index and the normalization are allowed to vary freely. The spectral fit was done with Sherpa using levmar optimization method and chi2datavar statistics.

The fitted spectral parameters are summarized in Table 3.5. The X-ray emission from the core is heavily saturated making it impossible to study the innermost parts of the jet. However, the nearby k4 knot's emission is well resolved from the core, the X-ray spectral index being 1.82 ± 0.1 and the flux being $(1.60 \pm 0.23) \times 10^{-13} erg \, cm^{-2} s^{-1}$.

Table 3.5: The Chandra X-ray analysis results of 3C 120 jet knots.

Region	Γ_X	νF_ν*	reduced χ^2
k4	1.82±0.10	15.97±2.3	1.03
k7	2.72±0.66	1.85±0.82	1.03
s2	2.64±1.26	0.78±0.51	0.81
s3	2.14±0.28	0.45±0.37	0.89
k25 inner	1.63±0.22	3.89±1.42	0.98
k25 outer	1.62±0.11	12.16±1.9	0.79
k25 new	1.80±0.19	6.28±1.67	0.91

*($\times 10^{-14} erg \, cm^{-2} \, s^{-1}$)

---

[21] http://cxc.harvard.edu/sherpa4.9/

The net counts from k7, s2 and s3 knots are relatively low < 50 (as compared with > 100 from other knots), not enough for a detailed spectral fitting. The fitting resulted in a steep X-ray slope (> 2.0) and a relatively faint X-ray flux ($\leq 10^{-14} erg\ cm^{-2} s^{-1}$). Because of low statistics and estimated large uncertainties, we did not consider them further. Following [9] we also sub-divide k25 into inner, outer and new regions which have different properties in the radio band (the inner refers to the upstream edge and the outer refers to the western edge, see Fig. 3 of [9]. The X-ray emissions from all 3 regions have harder X-ray emission spectra (≤ 1.8) with the X-ray flux varying within $(3.89 - 12.16) \times 10^{-14} erg\ cm^{-2} s^{-1}$. It is interesting to note that the flux of k25 outer is at the same level as that of the bright k4 but with a significantly harder X-ray spectral index of $\Gamma_X = 1.62 \pm 0.11$. The knot SEDs shown in Fig. 3.15-3.18 have been calculated by *sample_energy_flux* in Sherpa.

3.5 Modeling the spectral energy distributions

3.5.1 The core region

In the modeling of the origin of emission we initially use the data accumulated during 5.3 years of Fermi-LAT observations of 3C 120 [16]. The γ-ray light curves show that the flux is variable in 180 days ($t_{var} \sim 6\ month$). Using this variability time scale as well as typical dopler boosting factor for radio galaxies of $\delta \approx 3 - 5$, the emitting region size is

$$R < c\ t_{var} \sim 10^{18}\left(\delta/4\right)cm \tag{3.3}$$

This suggests that the γ-rays are produced from a compact region, which allowed to exclude the knots as the main sites where the γ-rays are produced.

Most likely, the γ-rays are produced in a compact region of the jet, e.g., the blob moving with relativistic velocities. Generally, the broadband spectrum of blazars as well as those from radio galaxies, which have jets oriented at systematically larger angles to our line of sight are successfully described by the SSC model [58-60]. In this modeling the low energy emission (radio through optical) is represented as a synchrotron emission from leptons in the homogeneous, randomly oriented magnetic field (*B*) while the HE component (from X-ray to HE γ-ray) is an inverse Compton scattering of the same synchrotron photons. This kind of interpretation for 3C 120 is the first choice considering the results of the modeling

of the other *Fermi*-LAT observed radio galaxies [61-63]. Here we apply the SSC mechanism to model the overall SED of 3C 120, particularly in the 0.1–100 GeV energy range. The multifrequency data (sub MeV/GeV energies) are from the simultaneous (quasi-simultaneous) observations of the 3C 120 [64].

We suppose that the emission is coming from a spherical region with the radius R_b moving with Lorentz factor $\Gamma = (1 - \beta)^{-1/2}$. The emission is boosted by $\delta = 1/[\Gamma(1 - \beta \cos(\theta))]$ where θ is the angle between the bulk velocity and the line of sight. The electron distribution follows

$$N'_e(E'_e) = N'_0 \left(\frac{E'_e}{m_e c^2}\right)^{-\alpha} Exp\left[-\frac{E'_e}{E'_{cut}}\right] \tag{3.4}$$

For $E'_{min} \leq E'_e \leq E'_{max}$, where E'_{min} and E'_{max} are the electron maximum and minimum energies respectively. The total electron energy $U_e = \int_{E'_{min}}^{E'_{max}} E'_e N'_e(E'_e) dE'_e$ is defined by N'_0, α are the electron spectral index, and E'_{cut} in the cutoff energy sales with the one of the magnetic fields.

We assume that HE emission has a pure SSC origin. As a first step, the radio data are included in the modeling, which means that the same electron population is responsible for both synchrotron and inverse-Compton emissions. The best guess values of electron energy distribution, which allows us to properly reproduce the low and HE data, corresponds to $\alpha = 2.8$, $\gamma_{min} = 800$ and $\gamma_c = 9.8 \times 10^3$ (dashed line in Fig. 3.11). Other model parameters are presented in Table 3.6. The ratio of non-thermal electron and magnetic field energy densities is equal to $U_e/U_B \approx 16$ (for magnetic field $B = 25$ mG). In this case, the jet power in the form of magnetic field and electron kinetic energy, given by $L_e = \pi c R_b^2 \Gamma^2 U_e$ and $L_B = \pi c R_b^2 \Gamma^2 U_B$, respectively $L_e = 2.42 \times 10^{45} erg\ s^{-1}$ and $L_B = 1.49 \times 10^{44} erg\ s^{-1}$. The total jet power L_{jet}, defined as $L_{jet} = L_B + L_e$, corresponds to $L_{jet} \approx 2.57 \times 10^{45} erg\ s^{-1}$, which is noticeably high. This interpretation is unlikely since the necessary jet power is of the same order as Eddington accretion power $L_{Edd} \approx 6.8 \times 10^{45} erg\ s^{-1}$ for the $5.5 \times 10^7 M_\odot$ black hole mass in 3C 120. This is not a strong argument considering that

some blazars might operate in the super-Eddington regime as follows from observations [65].

Table 3.6: SSC modeling parameters presented in Figure 3. The Doppler boosting is assumed to be $\delta = 4$ and emitting region radius $R_b \sim 10^{18}$ cm.

	$B(mG)$	α	γ_{min}	γ_c	U_e/U_B
solid line	30	2.4	700	1.7×10^4	1.9
dashed line	25	2.8	800	9.8×10^3	16
dot dashed line	25	2.0	2500	1.2×10^4	1.3
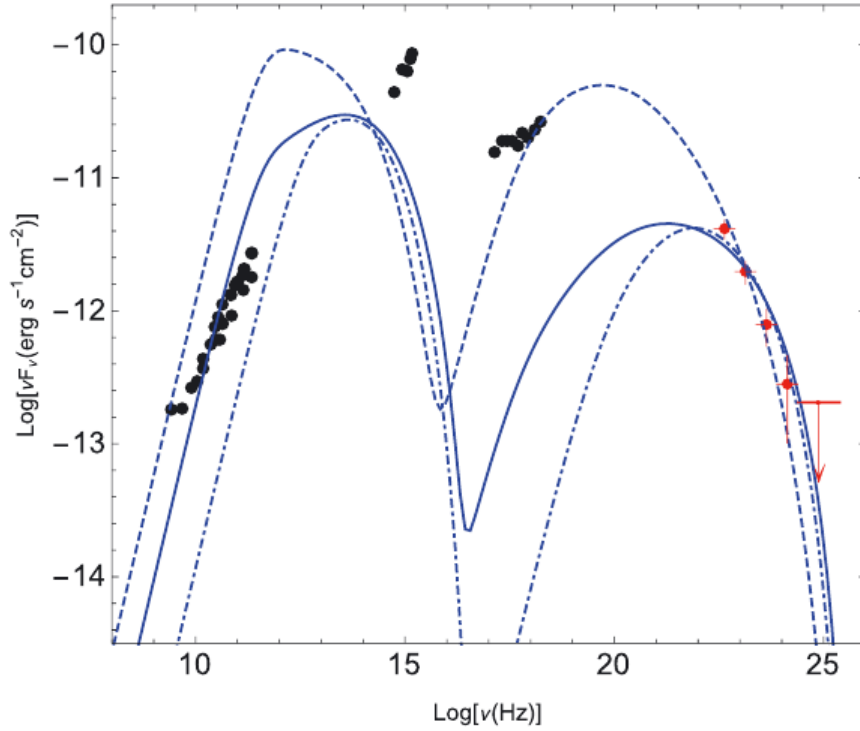
FIGURE 3.11: The SED of 3C 120 modeled with one-zone SSC component. Red points from Fermi-LAT 5.3 year's data analysis (this work), while black points refer to the simultaneous data from [64]. The SSC emission is calculated using a simulator developed by Andrea Tramacere [66-68] available at http://www.isdc.unige.ch/sedtool/.

However, this is not the case since the jet power can be relaxed, assuming the hard X-ray emission originates from the thermal Comptonization near the disk. Thus, the predicted flux from the SSC component falls below the hard X-ray limit in Fig. 3.11 (solid line). Indeed, a reasonable modeling of both radio and HE data gives an electron distribution with the index $\alpha = 2.4$ between $\gamma_{min} = 700$ and $\gamma_{cut} = 1.7 \times 10^4$. The jet energy carried out by particles (electrons) and magnetic field corresponds to $L_j = 6.27 \times 10^{44} erg\ s^{-1}$, which is still high but not dramatic. Moreover, unlike the other case, the electron nonthermal and magnetic field energy densities are close to equipartition $U_e/U_B = 2$ (for $B = 30$ mG). Even though

Page 48

the ratio $U_e/U_B = 16$ cannot be rejected, recalling other blazars where the jet is massively out of equipartition, the later modeling has an advantage considering the required total jet power.

In principle, the radio to X-ray and γ-ray emissions can be produced in different sites (blobs). Supposing the radio flux does not exceed that presented in [64], the electron distribution with a typical power law index $\alpha = 2$ predicted from strong shock acceleration theories can reproduce HE γ-ray data (dot dashed line in Fig. 3.11). The modeling requires a relatively high low energy cutoff, $\gamma_{min} = 2500$ and energy equipartition between nonthermal electrons and the magnetic field $U_e/U_B = 1.3$ (for $B = 25$ mG). Moreover, the total jet kinetic power is $L_{jet} \approx 3.4 \times 10^{44} erg\ s^{-1}$ approximately half that in the previous modeling. From the point of view of the necessary lower energy, this model has an advantage over previous model. Nevertheless, this modeling is very sensitive to the choice of the γ_{min} which can be constrained only with simultaneous data. Although the radio data presented in Fig. 3.11 are not synchronous, they can be treated as an upper limit. Consequently, the expected luminosity should not be higher than the above obtained value.

In Fig. 3.11, SSC mechanism provides a good fit to all data except those in the optical/UV band $(10^{15} - 10^{16})Hz$. This UV excess is likely caused by direct thermal emission from the accretion disk. Indeed, a thermal component with a blackbody temperature $> 15\,000\,K$ and luminosity $\geq 2 \times 10^{44} erg\ s^{-1}$ can explain detected UV flux. This lower limit to the temperature and luminosity corresponds to minimal UV flux reported in [64] and presented in Fig. 3.11, but a hotter and luminous disk is expected to explain observed data. Thus, SSC radiation plus thermal component (contribution of the accretion disk) can satisfactorily reproduce the entire SED (including UV data). However detailed modeling of the thermal component goes beyond the scope of this paper.

The Fermi-LAT analysis of the 7 years accumulated data gives an interesting results investigating γ-ray flux temoral variation in daily time scale, as well as two Flares periods were discovered, where γ-ray fluxes increas dramatically [18].The daily time scale variability of 3C 120 ($t_{var} \sim 7\ day$) denotes the compactness of the emitting region. Under any reasonable assumptions for Doppler boosting, $\delta = 3 - 5$, the emitting region can not be

larger than $R < c\, t_{var} \sim 10^{17}(\delta/4)\,cm$. This immediately allows us to exclude jet knots (extended regions) as the main sites where the observed γ-rays are produced. Most likely, the γ-rays are produced in a compact region of the jet, e.g. the blob moving with relativistic velocities. Generally, the broadband spectrum is successfully described by the SSC model [58-60]. We suppose that the emission is coming from a spherical region with the radius R_b moving with Lorentz factor $\Gamma = (1 - \beta)^{-1/2}$. The emission is boosted by $\delta = 1/[\Gamma(1 - cos(\theta))]$, where θ is the angle between the bulk velocity and the line of sight. It is assumed that the electron distribution has Power-Law exponenta cut-off distribution, as mentioned in Eq. 3.4 with expected from the shock acceleration theories and the electron energy density U_e scales with the one of the magnetic field U_B.

TABLE 3.7: SSC modeling parameters presented in the Fig. 3.12. The Doppler boosting is assumed to be δ = 4 and emitting region radius $R_b \sim 10^{17} cm$

	$B(G)$	α	γ_{min}	γ_c	U_e/U_B
7 year (Blue)	0.35	2.7	350	5.7×10^3	2.6
Flare 1 (Red)	0.3	2.15	260	10^4	7.1
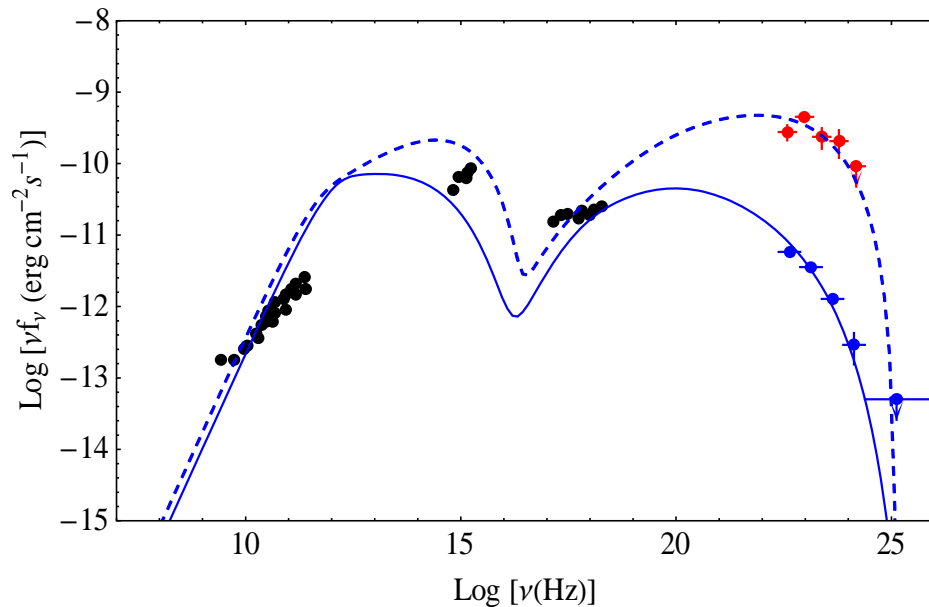
FIGURE 3.12: The SED of 3C 120 modeled with one-zone SSC component. Black points refer to the simultaneous (quasi-simultaneous) data from [64]. Red and blue points are from Fermi-LAT data analysis (this work). The details of the modeling parameters are presented in the Table 3.7.

In the Fig. 3.12 the results of the modeling of SED are presented. The solid line corresponds to the modeling of the averaged γ-ray spectrum, while dashed lines to the

modeling of flaring period. The long term averaged spectrum is best described assuming electron spectrum with $\alpha = 2.7$ between $\gamma_{min} = 350$ and $\gamma_c = 5.4 \times 10^3$. The ratio of non-thermal electron and magnetic field energy densities is equal to $U_e/U_B \approx 2.6$ (for magnetic field $B = 0.35\,G$). Other model parameters are presented in the Table 3.7. In this case, the jet power in the form of the magnetic field and electron kinetic energy, are $L_B = 1.24 \times 10^{44} erg\ s^{-1}$ and $L_e = 5.43 \times 10^{44} erg\ s^{-1}$. The total jet power L_{jet}, defined as $L_{jet} = L_B + L_e$, corresponds to $L_{jet} = 6.67 \times 10^{44} erg\ s^{-1}$. The flaring period is best described for the parameters $\alpha = 2.5$, $\gamma_{min} = 260$ and $\gamma_c = 10^4$ and $L_{jet} = 7.44 \times 10^{44} erg\ s^{-1}$. For both cases, the required jet power is smaller than Eddington accretion power $L_{jet} = 6.8 \times 10^{45} erg\ s^{-1}$.

In order to investigate the multiwavelength emission from 3C 120 nuclear region, more detailed data analyses results are used [19]. In particular, the emissions from 3C120 in the quiescent and flaring states are modeled tacking into account SSC and external inverse Compton models (EIC). In the flaring state (Fig. 3.14) the X-ray flux moderately increased and the spectrum softened, while the HE γ-ray flux increased and its spectrum shifted to higher energies. Within the synchrotron/SSC or EIC scenarios, these modifications can be explained as the result of introducing changes in the electron acceleration, increasing the commoving radius and bulk Lorentz factor, or including the contribution from external photons [69]. Here we discuss the following possibilities: (i) in the quiescent state the jet energy dissipation occurs close to the central black hole and the dominant mechanism is the synchrotron/SSC emission; (ii) in the flaring period again the dominant processes is SSC, although the emission region has a higher bulk Lorentz factor; and (iii) the optical/UV/X-ray emission is due to the synchrotron/SSC emission from an extended and slow-moving region, while the HE γ-rays come from a compact and fast-moving region where EIC dominates. This is similar to the scenario adopted by [70] to explain the very fast VHE γ-ray variations and the hard GeV spectrum of PKS 1222+216. The choice of this scenario is justified since strong changes are observed only in the γ-ray band. We assume, as in the quiescent state, since no significant γ-ray variability is observed (or it varies in a long period) most likely the emission is produced in a large region for which we assume $R \approx 4 \times 10^{17} cm \sim 0.1\ pc$.

Instead, in the active state the fast γ-ray flares in day/subday time scales indicate that the emitting region size should be $R/\delta \le c \times t \times \delta = 1.56 \times 10^{16}(t/1day)(\delta/6)cm.$

Table. 3.8: Parameters obtained from the fit of the emission from the inner jet of 3C 120 during quiescent and flaring states

	Parameter	SSC(blue-dashed)	SSC(red)	SSC	SSC+EIC
Doppler factor	δ	4	4	6	4(6)
Normalization of electron distribution	$N_0' \times 10^{50}\ eV^{-1}$	$15292^{+34383.07}_{-10357.06}$	$16.77^{+176.69}_{-14.02}$	$1.96^{+2.75}_{-1.13}$	$1713.92^{+19.88}_{-18.69}(817.55^{+118.64}_{-117.96}$
Electron spectral index	α	$3.12^{+0.15}_{-0.16}$	$1.85^{+0.31}_{-0.22}$	$2.79^{+0.16}_{-0.13}$	$3.12 \pm 0.22(3.24^{+0.89}_{-0.80})$
Minimum electron energy	$E'_{min}(MeV)$	$354.51^{+27.20}_{-24.55}$	$228.18^{+92.19}_{-120.10}$	$67.57^{+18.03}_{-20.65}$	$117.23^{+11.80}_{-12.64}(514.51^{+569.19}_{-352.58})$
Cut off electron energy	$E'_{cut}(GeV)$	$3.21^{+0.60}_{-0.46}$	$4.61^{+1.63}_{-0.77}$	$6.32^{+2.93}_{-1.48}$	$1.68^{+0.42}_{-0.41}(4.05^{+5.37}_{-2.10})$
Maximum electron energy	$E'_{max}(TeV)$	$2.30^{+3.84}_{-1.54}$	$1.90^{+3.02}_{-1.26}$	$1.83^{+2.19}_{-1.27}$	$10.71^{+4.64}_{-6.56}(54.56^{+75.36}_{-40.27})$
Magnetic field	B[G]	$0.16^{+0.006}_{-0.007}$	$0.0023^{+0.00025}_{-0.00018}$	$0.86^{+0.11}_{-0.09}$	$0.63 \pm 0.12(0.11^{+0.11}_{-0.08}$
Electron energy density	$U_e(erg\ cm^{-3})$	1.02×10^{-3}	1.99×10^{-2}	0.14	$4.39 \times 10^{-4}(0.25)$
Jet power in magnetic field	$L_B \times 10^{44}erg\ s^{-1}$	2.58	4.98×10^{-4}	0.22	38.34(0.0034)
Jet power in electrons	$L_e \times 10^{44}erg\ s^{-1}$	2.46	48.00	1.09	1.06(2.02)

In the flaring state, the inverse Compton scattering of external photons either reflected from the broad line region (BLR; [71]) or from the hot dusty torus [72,73] can contribute to the emission in the γ-ray band. For any reasonable assumption about the jet opening angle $(\theta = 0.1^{\circ})$ and Doppler boosting factor $(\delta = 6)$ the γ-ray emission region is at the distance $\sim R/\theta \approx 2.3\ pc$, well beyond the radius of BLR $(5.9 - 7.4) \times 10^{16}cm$ determined from reverberation mapping [74].

In this case, the dominant external photon field is the IR radiation from the hot dusty torus, which we assume has a blackbody spectrum with a luminosity of $L_{IR} = \eta L_{disk}$ ($\eta = 0.6$) [75] and these photons are filling a volume that for simplicity is approximated as a spherical shell with a radius of $R_{IR} = 3.54 \times 10^{18}(L_{disk}/10^{45})^{0.5}cm$ [76]. The accretion disk luminosity was

estimated using the Swift UVOT data points observed during the flaring periods. Reproducing the UVOT fluxes with the Shakura-Sunyaev disk spectrum [77] fixing the peak energy at ~10 eV, we obtained that the disk luminosity $L_{disk} = 1.2 \times 10^{45} \, erg \, s^{-1}$ (see Fig. 3.14 black dashed line), which is close to the value obtained in [78].
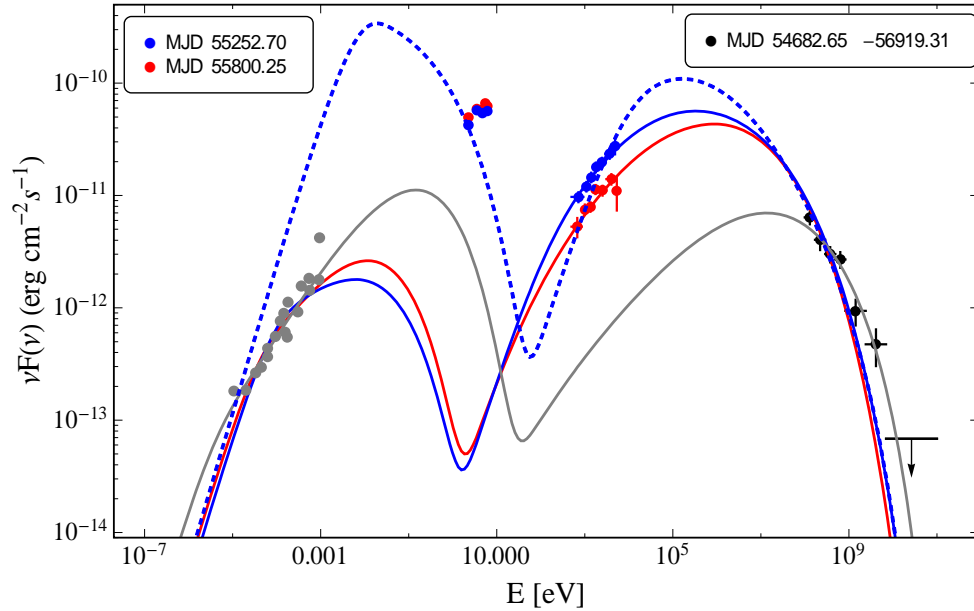
FIGURE 3.13: The broadband SED of 3C 120 core emission for quiescent state. The blue and red solid lines are the synchrotron/SSC model fitting for two different X-ray fluxes, taking into account the radio data and assuming Swift UVOT data are upper limits. Instead the dashed blue line is calculated assuming optical/UV emission is also produced by the jet. The model parameters are presented in Table 3.8.

In order to constrain the model's free parameters, we have modified the naima package [79], which derives the best fit and uncertainty distributions of spectral model parameters through Markov chain Monte Carlo (MCMC) sampling of their likelihood distributions. The prior likelihood, our prior knowledge of the probability distribution of a given model parameter, and the data likelihood functions are passed onto the emcee sampler function for an affine-invariant MCMC run. In the parameter sampling, the expected ranges considered are $1.5 \leq (\alpha, \alpha_{PL}) \leq 10$ and $0.511 \, MeV \leq E'_{cut} \leq 1 \, TeV$, and N_0 and B are defined as positive parameters. The synchrotron emission is calculated using the parameterization of the emissivity function of synchrotron radiation in random magnetic fields presented in [28], while the IC emission is computed based on the monochromatic differential cross section of [80].

The broadband emission modeling results obtained in the quiescent and flaring states are shown in Fig. 3.13 and in 3.14, with the corresponding parameters in Table 3.8.

In the quiescent state, the X-ray spectra have different photon indices, $\Gamma_X = 1.42 \pm 0.07$ and 1.53 ± 0.08, and is the reason why both spectra have been considered during the fit. In the fit we also included the archival radio data from the observations in the period when the source was in the quiescent state. The radio emission can be produced from the low energy electrons, which are accumulated for longer periods, so the radio flux should not exceed the presented limit. When both radio and optical/UV data are considered, a larger value of E'_{min} is required in order to have model which predicts emission below the radio flux. However, the increase of E'_{min} would also affect the flux predicted by SSC in the X-ray band; for example, the blue dashed line in Fig. 3.13 illustrates the model for $E'_{min} \simeq 354.51 \pm 25.91 \, MeV$ (summing the errors in quadrature) min beyond which the model predicts either a high radio flux or a low X-ray flux. The magnetic field is $B = 0.16 \, G$ with an energy density of $U_B = 1.07 \times 10^{-3} erg \, cm^{-3}$, slightly higher than that of the electrons $U_e = 1.02 \times 10^{-3} erg \, cm^{-3}$. This magnetic field energy density should be considered as an upper limit since the *Swift* UVOT data may represent the direct thermal disk emission, which means, in principle, that the synchrotron component can be much lower. Thus, in the second modeling, we assume that the low energy component is only defined by the radio data (blue and red solid lines in Fig. 3.13). In this case the underlying electron distribution is characterized by a harder power-law index ($\alpha = 2.22 \pm 0.19$ and $\alpha = 1.85 \pm 0.27$ for blue and red solid lines, respectively) and higher cutoff energy $E'_{min} = 4.61 \pm 1.27$. The magnetic field is significantly lower, $B = 2.3 \times 10^{-3} G$, and the jet should be strongly particle-dominated to have the peak flux of the HE component exceeding that of the low energy one. This particle dominance can be minimized assuming that the X-ray emission is of a different origin (e.g., from another blob or from thermal Comptonization near the disk). When the optical/UV and X-ray data are assumed as upper limits in the fit, a lower flux from SSC emission is expected (gray line in Fig. 3.13) and now $U_e/U_B \approx 43$.

When the SED in the flaring period is modeled considering SSC emission (red solid line in Fig. 3.14) the electron distribution and the magnetic field should vary. As the X-ray

spectrum is soft ($\Gamma_X = 1.8$), the modeling yielded a lower $E'_{min} = (67.57 \pm 19.38)\ MeV$ and $\alpha \simeq 2.79 \pm 0.15$. As the min $\gamma - ray$ spectrum is shifted to higher energies, then a cutoff of $E'_{cut} = (6.32 \pm 2.32)\ GeV$ is required. Since the emitting region radius decreases by ~ 25.6 times, the magnetic field should increase ($0.86 \pm 0.1\ G$) in order to produce a synchrotron flux of the same order (or higher) because the synchrotron emission depends on the total number of the emitting electrons (N_e, δ, and magnetic field B). In this case, the required electron energy density exceeds that of the magnetic field only 2.6 times, meaning there is no significant deviation from equipartition. The radio data are also plotted as reference values, but we note that in the flaring state the radio flux can also increase. However, the model does not predict a flux that significantly exceeds the observed radio data.
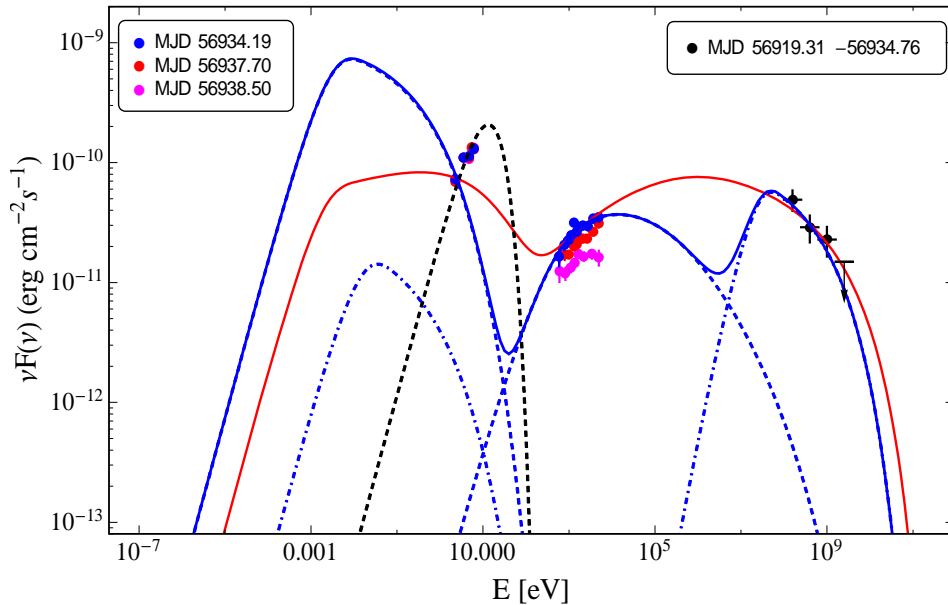
FIGURE 3.14: The broadband SED of 3C 120 core emission for flaring state. The SED in flaring state fitting with one-zone synchrotron/SSC (red solid line) and two zone SSC+EIC (blue solid line) models. The model parameters are presented in Table 3.8.

In Fig. 3.14 SSC (blue dashed line) and EIC (blue dot dashed line) modeling of the SED is shown (SSC+EIC, blue solid line). The X-ray emission can be explained by the SSC emission produced in a blob of a size similar to that emitting in a quiescent state, but additional changes in α, E'_{cut} and B are necessary to account for the new X-ray spectrum. Instead, the γ-ray emission is entirely due to the IC scattering of external photons in the fast and compact blob, which is strongly particle-dominated with $U_e/U_B \approx 519$, and the magnetic

field $B = 0.11 \pm 0.1\ G$, which does not differ much from the values obtained in the one-zone models. In the radio band, the modeling predicts a higher flux than the presented radio data. As the radio data are not from the source active periods, this is not a strong argument to disfavor such modeling. When a larger value for E'_{min} is used in the modeling, it does not introduce significant changes in the model parameters (especially in the energetics of the jet). Even if there are not enough data to estimate the parameters with a high significance, which means that the conclusions are not definite, this is an interesting modeling as it could possibility explain the rapid γ-ray activities. Such a blob can be naturally formed in the reconnection events that could produce compact regions of rapidly moving plasma inside the jet ("jet-in-jet scenario", [81]).

3.5.2 The large-scale jet emission

We assembled the 3C 120 knot SEDs from the radio to X-ray bands [19], using the radio to optical data from [9] (black points in Fig. 3.15, 3.16, 3.17, 3.18) and the X-ray data obtained in Section 3.2.2 (red points in Fig. 3.15, 3.16, 3.17, 3.18). The X-ray flux is well above the extrapolation from the radio to optical spectra and it hardens; this is more evident for the k25_new where $L_X/L_{rad} \simeq 250$. This confirms the previous findings that two different components are necessary to explain the radio to optical and X-ray emission from the knots of 3C 120. The detected highly polarized emission led to a conclusion that the radio to optical emission from the knots is of a synchrotron origin. The radiative mechanism usually considered to explain the origin of the X-ray emission is either the synchrotron emission from a second, much more energetic population of electrons (e.g., [9-12]) or the inverse Compton scattering on various possible sources of soft photons, including the synchrotron photons (SSC; e.g., [13]) and the cosmic microwave background photons (IC/CMB: e.g., [14]). Most naturally, the X-ray emission could originate from IC scattering of synchrotron photons with a density of $L_{radio}/4\pi R_{k4}^2 c \approx 3.2 \times 10^{-14}\ erg\ c$ where $L_{radio} \simeq 2.0 \times 10^{40} erg\ s^{-1}$ is the radio luminosity of k4 and $R_{k4} \approx 0.42\ kpc$ is the knot size. When comparing the radio and X-ray data it becomes clear that $L_{SSC} \geq L_{syn}$ $(U_B \leq U_{syn})$ is satisfied only if $B \leq 0.8\ \mu G$, which is in contradiction with the averaged value of $\geq 10\ \mu G$

usually estimated for the knots. In such a weak magnetic field, the observed radio luminosity can be accounted for only if the particle energy (U_e) strongly dominates over the magnetic field, thus contravening the equipartition condition, which means that we only consider the inverse Compton scattering of CMB photons and synchrotron emission from a second, much more energetic population of electrons.

In the IC/CMB scenario, it is assumed that the emitting region moves with a relativistic bulk Lorentz factor of Γ_{bulk} in order to predict a larger X-ray luminosity since in the jet frame the energy density of CMB photons will be enhanced by a factor of Γ_{bulk}^2. The condition of $L_{X-ray} > L_{radio}$ is satisfied only if δ is at least 10. In contrast, if the X-ray emission is produced by synchrotron radiation from a second population of relativistic electrons with very high maximum energy, a highly relativistic jet is not required and we assume $\delta = 1$. Since the electrons with high maximum energy would quickly cool down, most likely they were produced in a separate episode of acceleration that occurred more recently.

FIGURE 3.15: The SED of k4 knot. The radio-to-optical data (black points) are from previous studies and the X-ray data (red points) are derived in this paper. Black lines are the IC/CMB model calculated for $\delta = 10$ and blue lines are the fit by the two-component synchrotron model.

Moreover, the second population of electrons can be produced in different parts of the knot (e.g., [82,83]). We do not go into much detail, but we assume that there are two different electron populations responsible for the emission.

In the IC/CMB scenario, the underlying electron distribution is given by Eq. (3.4) with the cutoff energy allowed to vary only for k4, where the optical flux at $\sim 10^{14}\,Hz$ allows the HE tail of synchrotron emission to be constrained, while for the other knots it is fixed at

$E_{cut} = 100 \, GeV$ due to the lack of data. In addition, a power-law distribution in the form of $N \sim E^{-\alpha_{PL}}$ is added PL e to model the X-ray spectrum in the two-component synchrotron scenario. Since there are not enough data to constrain $E_{max,PL}$, an artificial HE limit of $E_{max,PL} = 1 \, PeV$ has been introduced, whereas $E_{min,PL}$ is left as a free parameter with the restriction that the flux from the second component should not exceed the first. In our calculations, we used the shapes and sizes of the knots as provided in [9]. To make the deviation from the equipartition condition as small as possible, we define $\eta = U_e/U_B$, which is used as a free parameter with U_e during the fit. This will allow us to find the optimum value for η when $\eta = 1$ does not give satisfactory representation of the data. In the two-component synchrotron model, we fix $\eta = 1$ and perform fitting of the radio to optical data. Then fixing this magnetic field, the X-ray data are fitted with the second component.
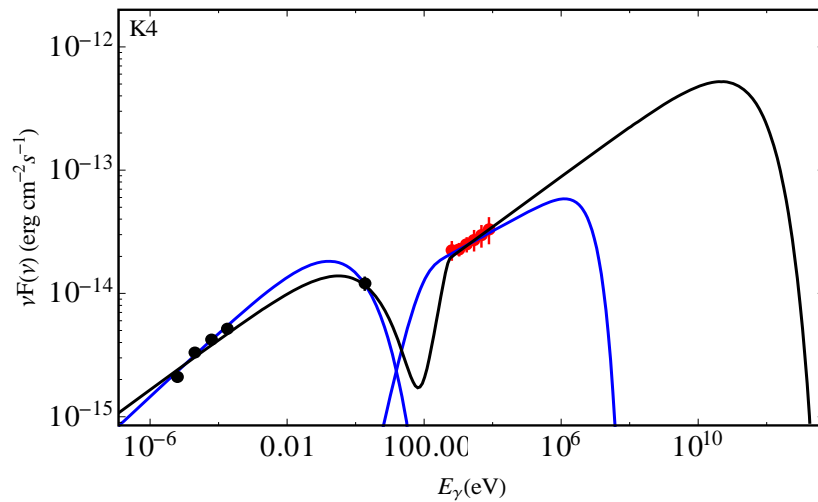

FIGURE 3.16: The SED of K25 inner knot. The radio-to-optical data (black points) are from previous studies and the X-ray data (red points) are derived in this paper. Black lines are the IC/CMB model calculated for $\delta = 10$ and blue lines are the fit by the two-component synchrotron model.

The black lines in Fig. 3.15-3.18 represent the IC/CMB radiation model calculated for $\delta = 10$. The obtained parameters are presented in Table 3.9. Similar photon indices observed in the radio and X-ray bands allowed defining the power-law index of electrons which varies from 2.4 to 2.6. The cutoff energy estimated for k4 is $E_c' \approx (916.3 \pm 251.4) \, GeV$ implies there is effective particle acceleration above the TeV energies. The value of $E_{min}' \simeq (18.20 - 24.01) MeV$ estimated, which we obtain min by requiring a turnover below the X-ray data in order not to overproduce the radio/optical flux, but in principle lower values cannot be excluded. The IC scattering of CMB photons with $u_{CMB} \simeq 4.0 \times$

$10^{-11} erg\ cm^{-3}$ density (when $\delta = 10$) still predicts a flux lower than the observed value, so we were forced to adopt larger values of η.

FIGURE 3.17: The SED of K25 new knot. The radio-to-optical data (black points) are from previous studies and the X-ray data (red points) are derived in this paper. Black lines are the IC/CMB model calculated for $\delta = 10$ and blue lines are the fit by the two-component synchrotron model.

We found that when $B = (0.93 - 5.6)\ \mu G$ and $\eta = (83.4 - 410.8)$, the IC/CMB model can reproduce the observed spectra. The maximum electron energy density is estimated to be $1.12 \times 10^{-10} erg\ cm^{-3}$ for the k4, while for the other knots it is > 4 times lower. This is natural, since even if the total number of particles is conserved, the low energy cutoff moves to lower energies (because of adiabatic losses), the normalization decreases and U_e does so as well. The IC/CMB component predicts emission up to $\sim \varepsilon_{CMB}(E_e/m_e c^2)^2 \approx$ 27.4 GeV so that $\gamma - ray$ emission is also expected. However, even if the predicted flux is above the Fermi-LAT sensitivity ($\sim 10^{-13} erg\ cm^{-2} s^{-1}$), its level (a few times $10^{-13} erg\ cm^{-2} s^{-1}$) would be still below the core emission in the quiet state (Fig. 3.13). Moreover, the Doppler boosting of $\delta \geq 10$ requires the jet to be highly relativistic or viewed at small angles at kpc distances from the core, which seems unrealistic for 3C 120, so even lower flux levels are expected.

The blue lines in Fig. 3.15-3.18 show the two-component synchrotron model fitting of the knot SEDs. The radio to optical data of the four knots are modeled with synchrotron emission with the following plausible parameters: B between 10.1 and 115.6 µG, and an electron power-law index of $\alpha = 2.20 - 2.48$.
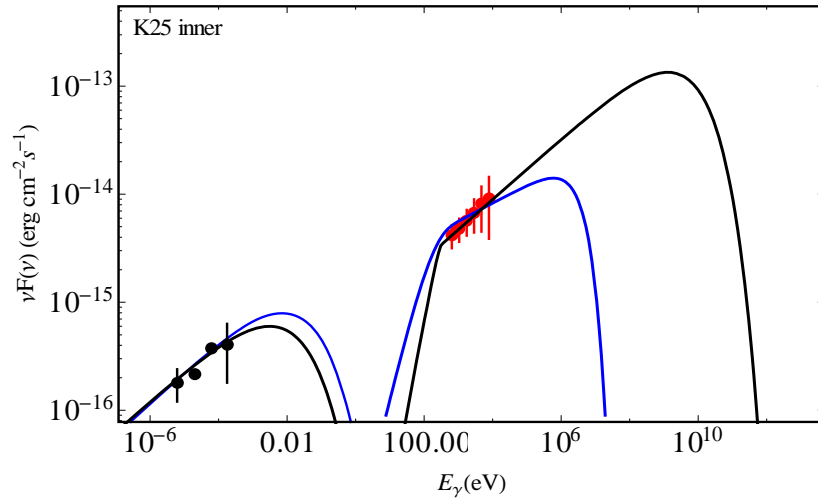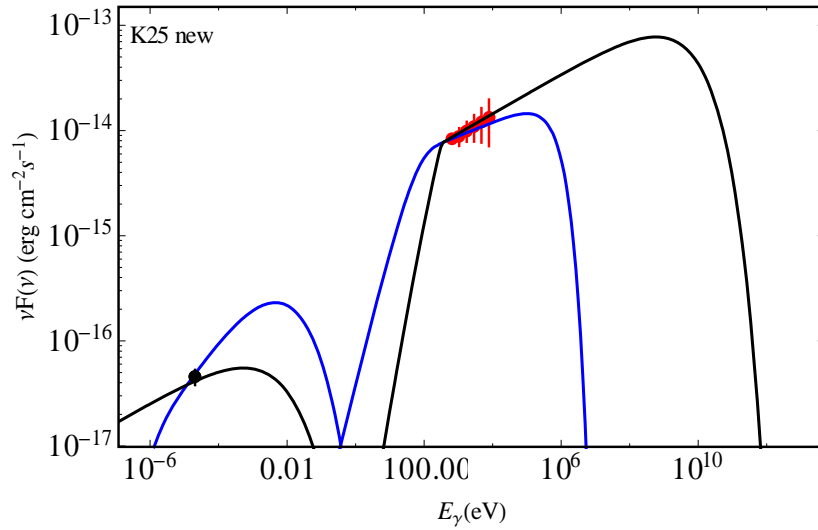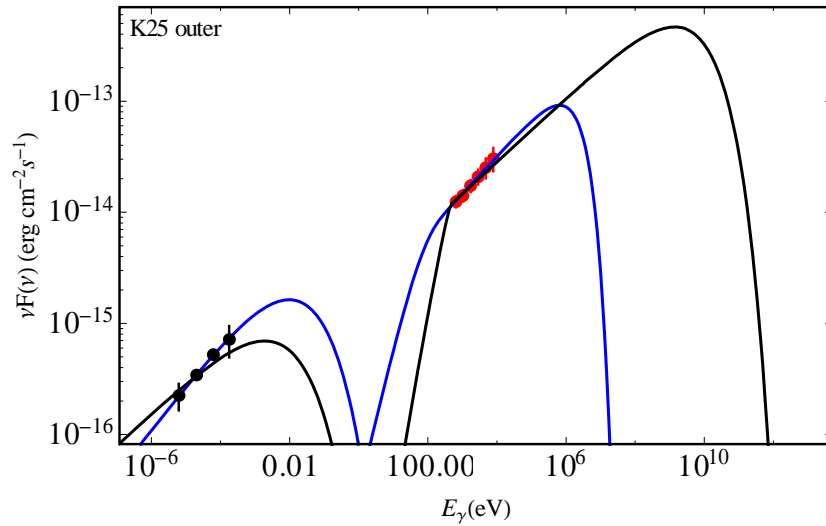
FIGURE 3.18: The SED of K25 outer knot. The radio-to-optical data (black points) are from previous studies and the X-ray data (red points) are derived in this paper. Black lines are the IC/CMB model calculated for $\delta = 10$ and blue lines are the fit by the two-component synchrotron model.

The plasma in the knots is in equipartition, $U_e = U_B = (4.1 - 531.5) \times 10^{-12} erg\ cm^{-3}$, which requires a magnetic field that is more than 10 times stronger for all the knots with respect to the previous modeling. The synchrotron emission of the second population of electrons for the same magnetic field can explain the X-ray flux when $E_{min} \simeq (2.83 - 8.88) TeV$ d $\alpha = (2.32 - 2.69)$. The particle energy density of this component is negligible compared with the other one. A significant contribution from the electrons with $E_e \simeq 10\ TeV$ is expected, the cooling time of which $t_{cool} = \frac{6\pi m_e^2 c^3}{\sigma_T B^2 E_e} \simeq 255.75\ yr$. This corresponds to a travel distance of $c \times t_{cool} \simeq 78.4\ pc$, which is much smaller than the size of the knots. Thus, it is required that the particle acceleration in situ over the entire volume of the knots should be extremely efficient.

The above obtained parameters were estimated taking into account the equipartition condition when the system is close to internal pressure or energy density condition, but for jet dynamics and propagation the jet pressure balance with the ambient medium is more important. The results presented here and previous observations of the knots allow us to put important constraints on some of the physical parameters of the jet. The jet half-opening angle (θ_j) at kpc scale can be estimated using the first resolved jet knot (k4); at a distance of 4 arcseconds from the core its radius is 0.738 arcsecond, implying $\theta_j \simeq 10.45°$.

Table. 3.9: The parameters derived from the modeling of the knots' SEDs.

Parameter	k4	k25 inner	k25 outer	k25 new
$U'_e(U_e)[erg\ cm^{-3}]$ $\times 10^{-12}$	$111.8^{+16.49}_{-9.91}(531.52^{+110.7}_{-84.76})$	$20.65^{+9.95}_{-3.47}(102.91^{+82.45}_{-45.22})$	$30.25^{+6.21}_{-2.73}(48.56^{+26.11}_{-13.47})$	$7.43^{+2.89}_{-1.43}(4.09^{+1.27}_{-0.63})$
α	$2.59\pm0.03(2.48\pm0.06)$	$2.44\pm0.1(2.41^{+0.22}_{-0.26})$	$2.42\pm0.04(2.20^{+0.17}_{-0.15})$	$2.62^{+0.14}_{-0.10}(2)$
$E'_{min}(E_{min})[MeV]$	$24.01^{+3.62}_{-5.44}(4.40^{+2.92}_{-2.31})$	$18.2\pm10.6(3.39^{+3.57}_{-1.90})$	$22.23^{+5.53}_{-8.43}(4.04^{+8.48}_{-2.92})$	$19.1^{+7.11}_{-8.57}(1445.67^{+3852.81}_{-1198.91})$
$B'(B)[\mu G]$	$5.61(115.6)$	$2.35(50.85)$	$1.36(34.94)$	$0.93(10.14)$
η	$89.39^{+7.48}_{-12.75}$	$94.04^{+49.8}_{-43.7}$	$410.86^{+64.28}_{-104.94}$	$214.3^{+162.67}_{-124.63}$
$U_{e,p}[erg\ cm^{-3}] \times 10^{-14}$	$6.01^{+5.85}_{-2.38}$	$2.36^{+2.59}_{-1.19}$	$7.22^{+3.01}_{-1.93}$	$13.22^{+15.7}_{-5.62}$
α_p	$2.69^{+0.22}_{-0.18}$	$2.66^{+1.15}_{-0.54}$	$2.32^{+0.17}_{-0.18}$	$2.73^{+0.29}_{-0.24}$
$E_{min,p}[TeV]$	$2.83^{+3.22}_{-1.73}$	$6.89^{+9.83}_{-5.17}$	$5.31^{+5.65}_{-3.16}$	$8.88^{+10.24}_{-6.78}$
$L_B \times 10^{42}$	$6.48(128)$	$71.26(333.7)$	$31.98(211)$	$0.67(3.69)$
$L_e \times 10^{44}$	$5.81(1.28)$	$66.98(3.34)$	$131.45(2.11)$	$1.44(0.04)$

Having the independent information on the jet Doppler factor, the upper bound on the magnetosonic (Mach) number is $M_j \sim 1/\tan(\theta_j)\Gamma_{bulk} \simeq 5.42/\Gamma_{bulk}$. If the jet remains relativistic up to kpc scale with $\Gamma_{bulk} = 5.3 \pm 1.2$, then $M_j \simeq 1.02$. For the pc jet of 3C 120, assuming an $R = 1.56 \times 10^{16} cm$ emitting region at parsec distance, M_j corresponds to 37.32. Thus, the relativistic jet with an initial high Mach number comes into static pressure equilibrium with the interstellar medium of the parent galaxy, starting to interact with it, causing the Mach number to decrease. This is qualitatively supported by the radio/X-ray observations, which reveal that at a distance of k4/k7 knots the jet starts to expand (e.g., Fig. 3 of [9].

3.6. Jet energetics

The fundamental quantity is the total power (particles + magnetic field) transported by the jet flow. The total jet power can be estimated using the parameters derived from the SED modeling using $L_e = \pi c R_b^2 \Gamma^2 U_e$ and $L_B = \pi c R_b^2 \Gamma^2 U_B$ [84] for electrons and magnetic field, respectively ($\Gamma = 1$ is assumed in the two-component synchrotron model). The protons with unknown contribution to the jet have not been considered in the calculations since a number of assumptions need to be made.

In the quiescent state, the total power at the jet core for all models presented in Fig. 3.13 is $L_{jet} = L_e + L_B \simeq (2.35 - 48.0) \times 10^{44} erg\ s^{-1}$ (as in [16-18,78]). Thus, the isotropic γ-ray luminosity, $L_{,em\gamma} \simeq 8.2 \times 10^{41} erg\ s^{-1}$, is only a small fraction of the total jet power. The jet's total power, $L_{jet} \simeq 1.31 \times 10^{45}\ erg\ s^{-1}$, decreases in the active state, since it scales with

the emitting region size ($L_{jet} \sim R^2 U$) and a smaller region is considered. However, this region is more energetic; the particle energy density is ~ 146.9 times higher than that in the quiet state. The SSC+EIC scenario requires a total jet luminosity of $L_{jet} \simeq 4.14 \times 10^{45}\ erg\ s^{-1}$, which is higher than the previous values, but is easily achievable for the black hole mass in 3C 120.

When the jet power is estimated for the knots, their largest reasonable volumes are used, so that the obtained values are the upper limits. In case of the beamed IC/CMB scenario the total jet power should be $L_{jet} \simeq (1.4 - 131.4) \times 10^{44} erg\ s^{-1}$ in order to explain the X-ray luminosity of $L_X \simeq (1.0 - 4.0) \times 10^{41} erg\ s^{-1}$. This jet luminosity is mostly defined by the kinetic energy of particles since the modeling reveals a moderate domination of particles over the magnetic field ($\eta \gg 1$). In the two-component synchrotron model, the total jet luminosity is lower, $L_{jet} \leq 6.7 \times 10^{44} erg\ s^{-1}$, where the contribution of the X-ray emitting component is negligible. The powers independently derived for the inner and outer regions of the jet are of the same order, suggesting that the jet does not substantially dissipate its power until its end, but becomes radiatively inefficient farther from the formation point.

3.7 Results and discussion

In this section, the multiwavelength emission from the 3C 120 core is investigated using Swift XRT/UVOT and Fermi-LAT data [16,18,19]. Quiescent and flaring states are identified and their modeling allowed us to investigate the jet properties and physical processes that take place in the core where, most likely, the jet is formed. On the other hand, the jet properties are also estimated at large distances from the core using the Chandra X-ray data. The adaptively binned γ-ray light curve showed that before MJD 56900 and after MJD 57300, the source was in a quiescent state characterized by a relatively faint γ-ray emission with the flux and the photon index consistent with the previously reported values. Then, from MJD 56 900 to MJD 57 300, most of the time, the source was in an effective γ-ray emitting state with rapid γ-ray flares. During the bright periods, the γ-ray photon index hardened and corresponded to ≈ 2.3 and ≈ 2.0. Two strong events with $(7.46 \pm 1.56) \times 10^{-6} photon\ cm^{-2} s^{-1}$ and $(4.71 \pm 0.92) \times 10^{-6} photon\ cm^{-2} s^{-1}$ within accordingly 19.0 min

and 3.15 h were detected on April 24, 2015, which are the highest fluxes detected so far from 3C 120. At a distance of 144.9 Mpc, these correspond to an isotropic γ-ray luminosity of $(1.20 - 1.66) \times 10^{46} erg\ s^{-1}$. The same value estimated for the quiescent state (the first bin in Fig. 3.13 red data) is $2.85 \times 10^{43} erg\ s^{-1}$. Yet, assuming δ = 6, the total power emitted in the γ-ray band in the proper frame of the jet would be $L_{em,\gamma} = L_{\gamma}/2\ \delta^2 = (1.67 - 2.31) \times 10^{44} erg\ s^{-1}$ during the peak flux and $L_{em,\gamma} = 8.9 \times 10^{41} erg\ s^{-1}$ in a quiescent state (assuming δ = 4). Thus, during the peak emission, the energy released in the γ-ray band corresponds to large fraction of Eddington luminosity ($L_{Edd} = 6.5 \times 10^{45} erg\ s^{-1}$ for the black hole mass of $5.5 \times 10^7 M_{\odot}$, [34]), while it is a small fraction ($\sim 1.4 \times 10^{-4}$) in the quiescent state.

Usually the radio galaxies have a luminosity of $\leq 10^{44} erg\ s^{-1}$ [21,85], and the peak γ-ray apparent luminosity of $(1.20 - 1.66) \times 10^{46} erg\ s^{-1}$ is unusual, more characteristic for BL Lac objects. Such a strong γ-ray output observed from 3C 120 is not surprising as the jet inclination angle is relatively small compared with other radio galaxies.

In the X-ray band, the average flux in the 0.5–10.0 keV range is around $(2.4 - 4.3) \times 10^{-11} erg\ cm^{-2} s^{-1}$ in the quiet state and $(5.4 - 6.7) \times 10^{-11} erg\ cm^{-2} s^{-1}$ on October 4–7, 2014 (active state). When the lowest and highest fluxes from Table 3.1, 3.3, and 3.5 are compared, a nearly 2.8 times increase of the X-ray flux is found, but its amplitude is lower than the substantial increase in the γ-ray band. During the considered periods, the source spectra were always hard $\Gamma_X < 2.0$. At bright γ-ray flares, the X-ray photon index softened (1.72–1.80) as compared with the hard photon index of (1.42–1.53) in a quiescent state. The small change in the X-ray flux level and the photon index softening might indicate that different mechanisms are contributing to the acceleration and/or cooling of electrons, which modifies the power-law index and the minimum energy of underlying electrons.

3.8 Summary

The main properties of the powerful jet of 3C 120 are investigated by comparing the physical state of the plasma on sub-pc and kpc scales [16,18,19]. The main processes responsible for the broadband emission in the innermost ($\leq pc$; Swift XRT/UVOT and

Fermi-LAT data) and outer ($\geq kpc$; Chandra data) regions are also studied. We report on the recent observations of 3C 120 with Fermi-LAT. The source is detected up to 10 GeV with statistically significant 18.27σ as a result of the accumulation of the data from longer all sky exposure. The photon index corresponds $\Gamma = 2.69$ and $F = (4.12 \pm 0.5) \times 10^{-8}$ photon $cm^{-2}s^{-1}$ photon flux above 100 MeV. We report also an interesting modification of the γ-ray flux in time. Initially the source described by the γ-ray flux mostly below than the Fermi-LAT sensitivity threshold appears to be frequently detected afterwards.

On April 24, 2015, a rapid and dramatic increase in the γ-ray flux was observed from the inner jet of 3C 120. Within 19.0 min and 3.15 h the flux was as high as $(7.46 \pm 1.56) \times 10^{-6}\ photon\ cm^{-2}s^{-1}$ and $(4.71 \pm 0.92) \times 10^{-6}\ photon\ cm^{-2}s^{-1}$ above 100 MeV which corresponds to an isotropic γ-ray luminosity of $(1.2 - 1.6) \times 10^{46}\ erg\ s^{-1}$. A luminosity of this level is unusual for radio galaxies and more typical for BL Lacs.

This increase of flux shows monthly or daily scale variability of 3C 120 indicating that the γ-rays are produced in sup-parsec regions. In principle, this change can have different physical origins. First, the change in the central engine, where possible jets obtain much of their energy from the infall of matter into a supermassive black hole, can at least have some influence. The changes in the jet power, hence higher intensity γ-ray, which is expected in the case when the additional matter is fueling the accretion disk. In theory, the observations of the region closer to the black hole with sensitive X-ray instruments (e.g. Chandra, XMM-Newton) can prove such a possibility. On the other hand, the environmental influence on the changes in γ-ray emission states can not be rejected considering the large scale powerful jet up to 100 kpc (e.g. target interacting with the jet). Any of the above mentioned possibilities would be supported by multiwavelength observations.

The synchrotron/SSC mechanism gives a reasonable explanation of the multiwavelength SED in the quiescent and flaring states. The increase and rapid changes in the flaring state can be also explained assuming an additional contribution from the blob where the dominant photon fields are of external origin. The necessary jet kinetic power is $L_{jet} \simeq (1.31 - 48.0) \times 10^{44}\ erg\ s^{-1}$.

The X-ray emission from the knots has a hard photon index of $\simeq (1.6 - 1.8)$ with a luminosity of $L_X \simeq (1.0 - 4.01) \times 10^{41}$. This X-ray emission can be explained by IC/CMB models only if $\delta > 10$, otherwise the particle energy density will strongly dominate over that of the magnetic field. If the X-rays were produced from the direct synchrotron radiation of the second population of electrons, which were produced more recently than the cooler population responsible for the radio to optical spectrum, then lower jet luminosity and no bulk relativistic motion on kpc scales is required.

Chapter 4

X-RAY EMISSION FROM γ-RAY EMITTING RADIO GALAXIES

4.1 Introduction

As it has been mentioned in the introduction, studying the emission processes in AGNs jet is one of the most modern and unsolved problems of modern astrophysics. The multiwavelength observations of the jets of AGNs allow to investigate some of the fundamental problems, such as jet formation, propagation and collimation, particle acceleration and emission processes, etc. [1]. Now, the available large amount of data (from radio to HE γ-ray bands) and the number of detected sources (e.g., nearly 3000 AGNs in the third catalog of AGNs detected by Fermi-LAT [85] significantly contributes to the understanding of the physics of AGN jets. In the AGN studies, perhaps one of the most discussed topics is the physical parameters of the plasma when the jet propagates from the central engine to the outer regions where the jet is starting to decelerate significantly. The recent progress in the X-ray instruments (e.g., Chandra) with an exceptional angular resolution allowed to investigate the jet emission even from distances much farther from the core, which opened a new window on the jet studies. Now, the strong jets can be well resolved in both small (pc) and large (kpc) scales, making it possible to investigate the processes occurring in powerful jets along their propagation. The fact that the knots are also X-ray emitters indirectly proves that there is an effective particle acceleration occurring in these structures. Definitely the emission produced in different regions of the jet are not from the same accelerated electrons since the GeV electrons (necessary to produce X-ray emission) only can propagate a few kpc from their acceleration sites [9]. On the other hand, as these electrons are accelerated in the same jet, some of the parameters, such as jet luminosity and the magnetic field, electron energy density etc. can be estimated and compared. For the current study [15,20], we select the radio galaxies having been detected

in the γ-ray band, because i) from the γ-ray observations the central/core region of the jet can be well investigated and ii) their large-scale jets are long enough to be resolved by Chandra telescope. There are 26 radio galaxies included in the third source catalog of Fermi-LAT and only the study of their spectral properties (e.g., their distribution, spectral breaks, etc.) provided interesting and important results [15]. On the other hand, the X-ray emissions from structures of these jets have been also detected which allows studying these jets in small and large scales [20].

4.2 Sample selection

For the study in this section, the radio galaxies included in the third catalog of AGNs detected by Fermi-LAT which have knots or hotspots in their large-scale jet are selected [15,20]. Among the detected 26 non-blazar AGNs we have selected eight sources (M87, Pictor A, 3C 303, 3C 275.1, NGC 6251, 3C 207, 3C 111 and 3C 120) which have a large-scale jet detected by Chandra. Some of the parameters of these sources are, e.g., the distances; types; coordinates and etc. are given in the Table 4.1.

Table 4.1: The main properties of the sample sources, as well as X-ray features are presented.

Source	R.A. Dec. (J2000) hh:mm:ss.s	class	Distance (red shift, z)	X-ray feature	N_H $\times 10^{20}\ cm^{-2}$
M87	12:30:49.4 +12:23:28.0	FRI	0.00427	knotty jet	1.94
Pictor A	05:19:49.7 –45:46:44.5	FRII	0.0350	linear jet, W hs,	3.12
3C 303	14:43:02.8 +52:01:37.3	FRII	0.141	2 knots, hs	1.71
3C 275.1	12:43:57.7 +16:22:53.2	LDQ	0.555	N hs	1.77
3C 207	08:40:47.5 +13:12:23.0	LDQ	0.680	knot, hs, CL	4.27
3C 111	04:18:21.3 +38:01:35.8	FRII	0.0491	knots	29.1
NGC 6251	16:32:31.9 +82:32:16.5	FRI/II	0.02488	knots	5.57

The considered sources are mostly nearby ones, the most distant source being 3C 207 at 4.1 Gpc, and the nearest source M87 at 18.4 Mpc. Their jets, having different structures and properties, extend from several tens of kpc to 150 kpc. The most interesting structures are observed in the large-scale jets of 3C 111 and Pictor A: in the jet of 3C 111, the X-ray emission is evident in at least nine regions, plus the northern and southern hotspots and the

jet of Pictor A extends over 200 kpc in projection with at least four evident X-ray emission regions in it. The knots are sometimes near the core (e.g., HST-1 at 60 pc), while some of the hotspots are at a distance larger than 150 kpc (e.g., WHS hotspot of Pictor A and SHS of 3C 111). Thus, this will allow to test the parameters of the jet plasma in the regions not only close to the central engine but also in the farther ones.

4.2.1 M87

M87 is one of the most studied and the nearest radio galaxies located in the Virgo cluster. At the distance 16.4 Mpc, (z=0.00436) [86] and having rich peculiar structures such us bright core and powerful one-sided jet [87], studying M87 allows to investigate almost all properties of AGNs and their components. The mass of supermassive black hole in M87 varies in the range of $(3 - 6.6) \times 10^9 M_\odot$ [88]. Initially the optical emission revel a jet like structure, originating from the core and extending more than $30''$ [89]. The jet formation and collimation processes have been essential targets of study for many years and M87 is a unique laboratory where it is possible to explore the collimation region of the jet occurring at -30–100 Schwarzschild radii (r_S) from the black hole [90]. Near the core, at the collimation region the opening angel of the jet is widening ($\sim 60^o$) [90]. In addition, it is noteworthy to mention that the Hubble Space Telescope (HST) observations have exposed eight features in the inner $6''$ of the core with optical superluminal velocity in the range 4c-6c [91]. Lorentz factor $\gamma \geq 6$ and 19 degree jet viewing angle were required for describing the observed fastest motions, which confirm that the bulk flow of the jet is relativistic [91].

The structure of the M87 jet has been minutely discussed due to Very Large Array (VLA)/Very Long Baseline Interferometry (VLBI) observations during the past three decades. From [92], at small distances ($< 10^5$ Schwarzschild radii), the jet retained parabolic and subsequently the jet is manifested as a conical shape, and the origin of the HST-1 is the result of the overcollimation of the jet. Another interesting result by [93] approves the existence of a triple-ridge structure across the jet based on the radio observations of M87 jet with the VLBA at 15 GHz. In the X-ray band the jet of M87 detected by Einstein [94,95] and the knots also investigated in the jet by [95], but it was not possible to estimate the

morphology of the inner jet's structure due to the low angular resolution of the Einstein and ROSAT data. Afterwards, at X-ray wavelengths, the nucleus and the inner structure of the jet of the M87 have been detected [96] and the brightest X-ray features i.e. the core and knot A have been detected [97].

Due to subarcsecond resolution, Chandra X-Ray Observatory allows us to precisely detect jet in the X-ray band. Furthermore, there are distinguished several bright knots (HST-1, D, E, F, I, A, B, C) shown in [20], which are presented in this work. The X-ray count map with removed noises by Gaussian filter and the knots and backgrounds region's sizes and coordinates are shown in Fig. 4.1. The X-ray regions sizes and coordinates are taken from observation [98,99] and the background's regions selection, as demonstrated in Fig. 4.1, are connected with the flares taken place in background, so previously we clean any anomalous effect during the X-ray analysis and after choose backgrounds. At high-energy γ-ray emission from the M87 has detected with Fermi-LAT based on 10 months' survey [47].
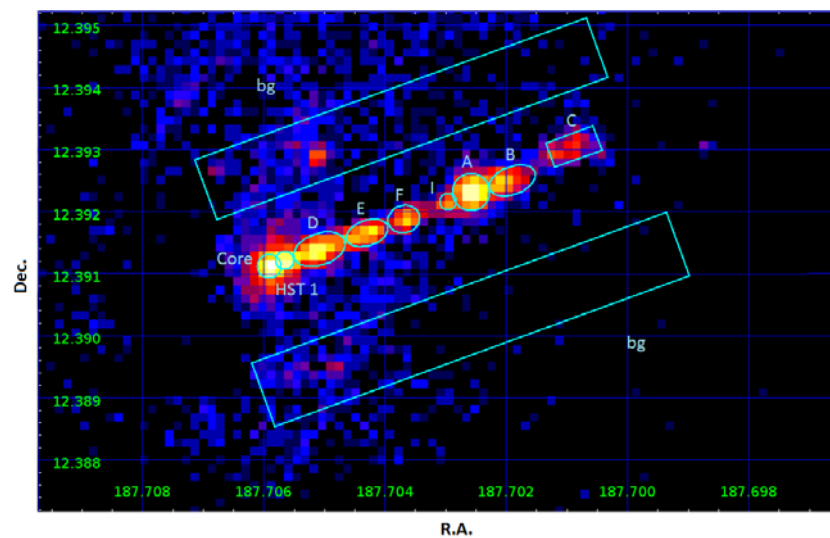
FIGURE 4.1: The X-ray count map of M87, with mentioned knots regions and backgrounds.

4.2.2 Pictor A

The broad line radiogalaxy Pictor A having two diffuse lobes included their bright hot spots, located appropriately on different poles of the radiogalaxy have the morphology similar to FRII sources [6,100]. In the optical emission spectrum of the Pictor A can be noticed broadening of the lines, thus it was classified as a broad line radiogalaxy (BLRG; [101]). The first radio observations indicate the source brightness in the radio wavelength, as well as

have been one of the brightest radio sources [102]. The radio Very Large Array (VLA) observation of the jet showed that it had relatively low luminous in comparison with the core and extended lobes [100]. Then, the very long baseline interferometry (VLBI) observations at 2.3 and 8.4 GHz showed the parsec scale structure of the jet, as well as discovered the relativistic motion of the several components within the jet [103]. Further observations also indicated the existence of compact hot spot inside the radio lobes [104]. Four knots have been investigated in the optical band in 32", 43", 106" and 112" distance from the core [105]. Moreover, interestingly in the X-ray band the emission from the jet is very bright as found from the Chandra X-ray observations [24]. The radiation from the knots in the radio to X-ray band can be well described by synchrotron radiation from the electrons [105].
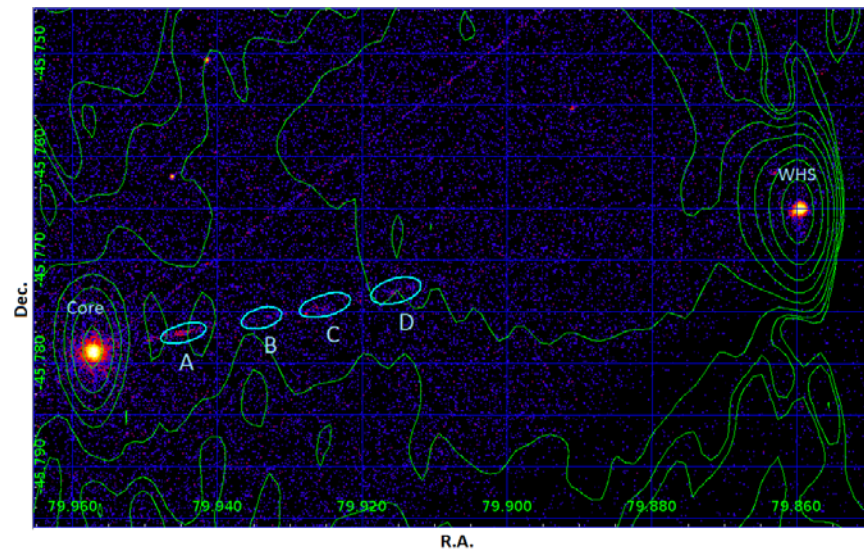
FIGURE 4.2 The X-ray count map of Pictor A, overlaid with radio contour, with mentioned four knots and western hotspot regions.

In Fig. 4.2 the count map of Pictor A as observed in the X-ray band with the knots in the large scale jet are shown. The X-ray count map overlaid with radio contour is taken from [104]. The knots are named A, B, C, D following their distance from the core, where the nearest one is at the distance of 30 arcsec (21 kpc) while the farthest one (D) at 105 arcsec (73.5 kpc) (1 arcsec corresponds to about 700 pc). It is interesting to highlight the western hotspot which is a distance of $4'2$ arcmin (176.4 kpc) with linear size of 10 arcsec (7 kpc). The three years of HE observations with Fermi-LAT have detected γ-ray emission from the Pictor A, with a significance of $\sim 5.8\sigma$, photon index, $\Gamma = 2.93 \pm 0.03$ and integrated flux is

$$F_\gamma = (5.8 \pm 0.7) \times 10^{-9} \ photon \ cm^{-2} s^{-1}$$ [106] and also included in Fermi-LAT 3FGL Catalog [85].

4.2.3 3C 303

The radiogalaxy 3C 303 (z=0.141) has a peculiar radio structure and the VLA 1.5 GHz image shows extended and exceedingly unsymmetrical kpc scale radio jet structure which is creating two-sided lobes (west and east) with their hotspots [107]. There were dedicated radio observations to investigate the emission from the western hotspot, which is very bright in the radio band [107] (see Fig. 4.3 where the count map observed by Chandra is shown). It is located at the end of one-sided jet approximately at the 36 kpc from nucleus as well as 408 MHz observation shows a double structure with [108]. At 5 GHz radio observations of 3C 303 shows that one-sided jet should have an inclination angle limited by $\leq 40°$ and the jet luminosity was estimated to be more than $0.7 \ c$ [109]. Optical observation by 2.5-m Nordic Optical Telescope have discovered optical counterpart of the composited radio hotspot [110]. Afterwards, during the Chandra observation X-ray emission has been detected from the hotspot and kpc-scale jet knots of 3C 303 [111]. The brightest radio structure hotspot was discovered [107] and also being resolved in the optical and X-ray bands [111].
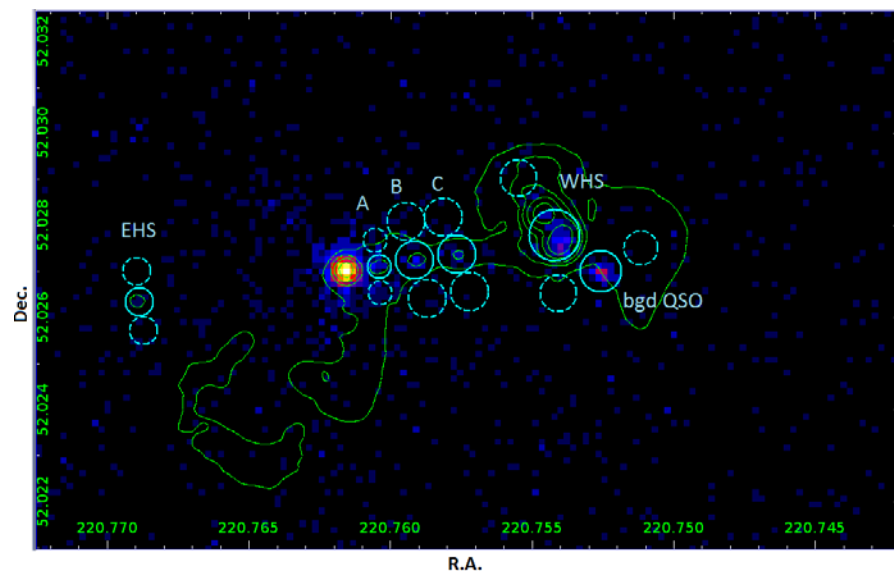
FIGURE 4.3: The X-ray count map of 3C 303, overlaid with radio contour, with shown knots, western hotspot and background regions.

The observations of 3C 303 resulted to detection of emission from near nuclear part and then the jet emission processes can be investigated both near the central nuclear parts as well as in the western hotspot the most extended and peculiar region [20]. The X-ray count map is overlaid with 1.5 GHz VLA radio contour taken from [107].

4.2.4 3C 275.1

3C 275.1 (z=0.557) is well known lobe dominated radio quasars (LDQ), having strong nuclei and interesting structured jet [112]. It is located at the center of a rich cluster of galaxies and is surrounded by an extremely large elliptical nebulosity having a major axis exceeding 100 kpc [113]. The source has extended noncollinear radio structure, and morphological studies indicate that the source exhibits "dog-leg" properties [114]. A parsec-scale radio image obtained in 15 GHz observations shows a typical core jet structure with jet extending toward northwest [115]. There are two visible components northern and southern hotspots, and the observations at 5 GHz show that one-sided jet is connected with the north edge-brightened radio lobe, while the opposite lobe appears to be separated from the core [114].
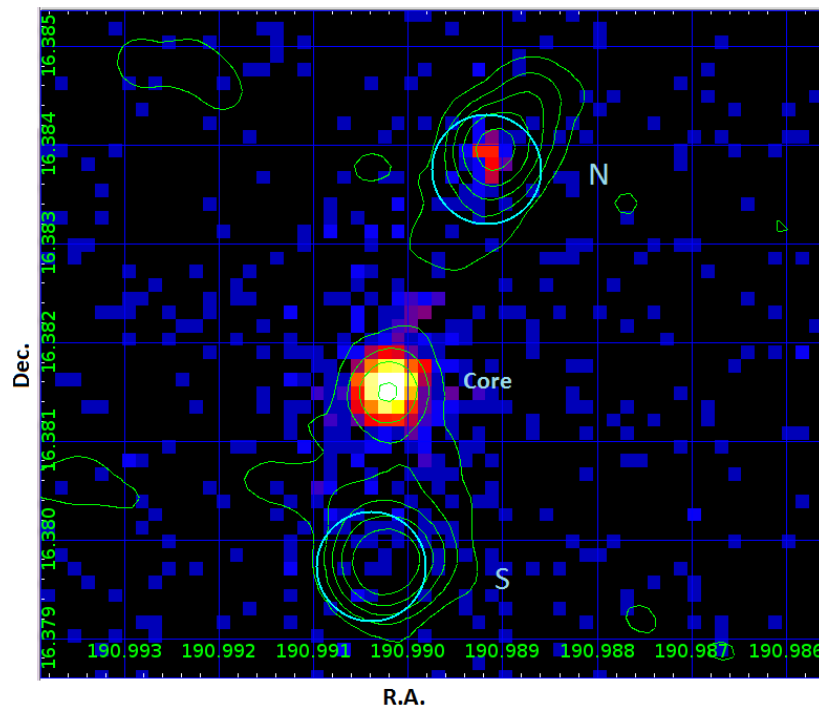
FIGURE 4.4: The X-ray count map of 3C 275.1, shown with radio contour and the Northern and Southern hotspot regions.

Interestingly, the emission from the hotspot in the north radio lobe is detected not only in the radio band, but also in the observations by Spitzer, Hubble Space Telescope (HST) and Chandra [116, 117].

In the Fig. 4.4 the X-ray image of 3C 275.1 obtained by Chandra telescope with corresponding hotspots is presented. The count map is overlaid with VLA 5 GHz radio contour taken from [118].

4.2.5 3C 207

3C 207 (z = 0.684) has been identified as strong lobe dominated radio quasar and the morphological study using VLBA observations shows activities both in the nuclear and the lobe regions [115]. The 3C 207 radiogalaxy is characterized as its luminous core correspondingly being continuum variable at short time scales [119]. Being very bright at 178 MHz, 3C 207 was included in Cambridge Third Catalog of Radio Sources (3CR) and then the VLBA images at 8.4 and 1.4 GHz provided more detailed view of the source with one-sided jet [120,121].
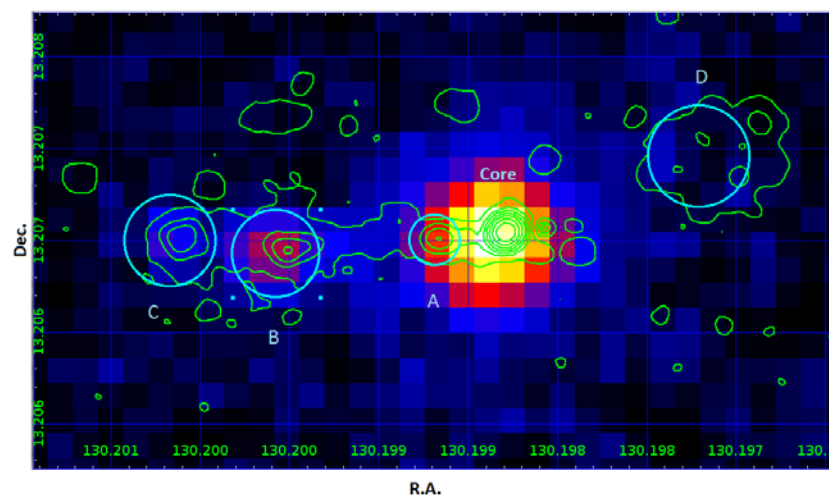
FIGURE 4.5: The X-ray count map of 3C 207 with the radio contours.

In X-ray band, the Chandra telescope has allowed to study the origin and energy of non-thermal relativistic electrons, correspondingly detecting X-ray photons from the northern hotspot [122]. 3C 207 radiogalaxy also displays activity at high energies and consequently detectable by Fermi-LAT, being included in first, second and third LAT AGN catalogs [47, 85,123]. The observations in the X-ray band with the Chandra telescope also resulted to

detection of X-ray emission from the northern hotspot. In the X-ray band the regions A, B, C and D are separated based on the observation of [124]. These regions are shown in the X-ray image in Fig. 4.5 and the count map is overlaid with the radio contour taken from [117].

4.2.6 3C 111

The 3C 111 is a broad line radiogalaxy and has FRII [6, 125] radio morphology. The bright source at z = 0.485 [126] was observed almost in all wavebands. The image of the 3C 111 at 20, 6 and 2 cm by VLA indicates the existence of rich extended structure with noticeable twin jet and distinguished knots, as well as north and south lobes and hot spots [127]. The jet inclination angle was estimated to be about $\sim 20°$ [128]. The jet is extremely long extending about 100 kpc on each side, and in this review 3C 111 is one of the candidates to study the properties of the extended structures of AGN's, including radio to X-ray wavebands [129]. The Chandra observation investigates X-ray emissions from the vast transverse northern jet, correspondingly detecting X-ray from the bright knots and hotspots [130]. Eight radio knots and northern and southern hot spots were also observed in near-IR/optical and X-ray bands, respectively with Hubble Space Telescope (HST) and Chandra telescope and the radio to X-ray SEDs of the knots were explained with two zone synchrotron radiation [129].
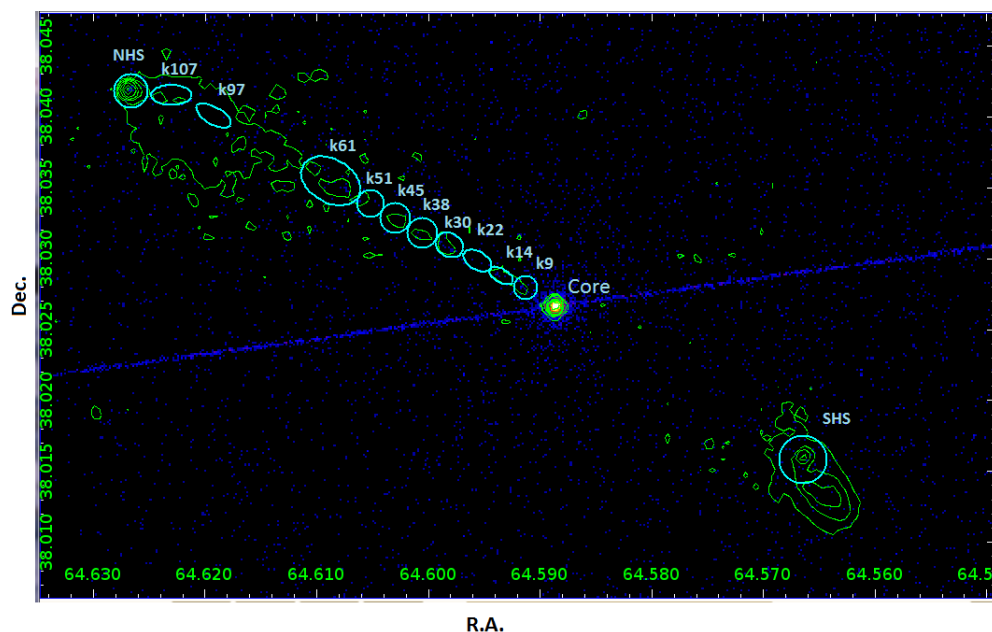
FIGURE 4.6: The X-ray count map of 3C 111 where the the knots and hotspots are shown.

The brightest features detected during the Chandra X-Ray observations are three knots in the northern jet (which we call K30, K61, and K97) and the northern hotspot (NHS) [129]. Now for the current study we select new knots based on [129] and are shown in Fig. 4.6. The overlaid radio contour is taken from [130] and it is remarkable that the hotspot NHS is far from the nucleus about 121 arcsec. Also, the strong emission from nuclear region was detected in the γ-ray band which made this source an ideal object for studying the jet emission in small and large scales [20].

4.2.7 NGC 6251

NGC 6251 is a huge elliptical of type E2 galaxy at redshift z = 0.024 (106 Mpc) [131] having radio morphology similar to FRI sources. The nucleus is surrounded with ionized gas ($\approx$ 150 pc) as implies that the nucleus of NGC 6251 hosts a black hole with mass $\approx (4-8) \times 10^8 \, M_\odot$ [132]. The VLA observations at 1.48 GHz and 4.9 GHz bands show a core and a complex jet, which is bright within 113 kpc, and it weakens and is curved at larger size scales [133]. Most likely the radio jet in NGC 6251, remains relativistic up to large distances from the core and it can be divided into (i) the bright inner region within $\sim 120''$ from the nucleus, (ii) from $\sim 120''$ up to $\sim 180''$ weak central part, (iii) the outer region between $\sim 180''$ and $\sim 270''$, and (iv) a curved and low-surface tail beyond $\sim 270''$ [94].
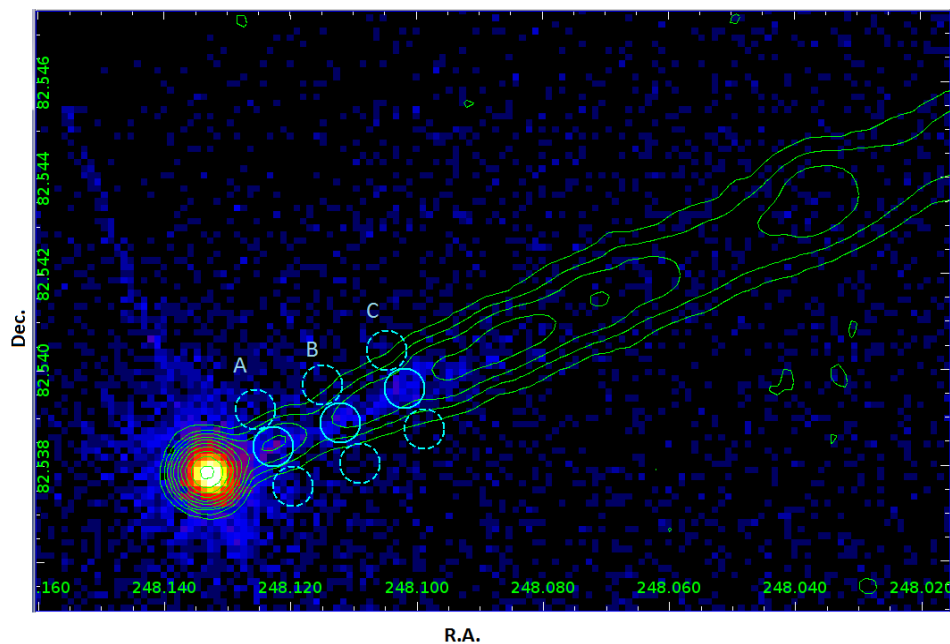
FIGURE 4.7: The X-ray count map of NGC 6251, overlaid with radio contour, with highlighted knots regions.

The X-ray observations allowed to identify A, B and C knots (see Fig. 4.7) which are respectively at distances $< 180''$, thus we are able to investigate the emission from the bright inner regions [20].

The X-ray emission from the large scale jet can be described by a power law with photon index $\Gamma \sim 1.2$ and IC/CMB radiation mechanism explains that X-ray emission, assuming that the system keeps equipartition condition and emission is strongly boosted by $\delta \sim 10$ [134]. At the HE energies the NGC 6251 has been detected with Fermi-LAT [20,48].

The X-ray image of NGC 6251 is shown in Fig. 4.7 with corresponding knots. The overlaid contour is the result of the VLA observation at 21 cm [135].

4.3 γ-ray and X-ray data analysis

The HE γ-ray emission of the selected AGNs has been investigated using the Fermi-LAT accumulated during its first 7 years' operation, from 4th August 2008 to 4th August 2015 (MET 239557417 - 460339204) [15]. The data analyses were performed following the steps in the Section 2.1.4 using the following parameters. The data were analyzed with standard Fermi Science Tools v10r0p5 software package released on May 18 2015, available from the Fermi Science Support Center.
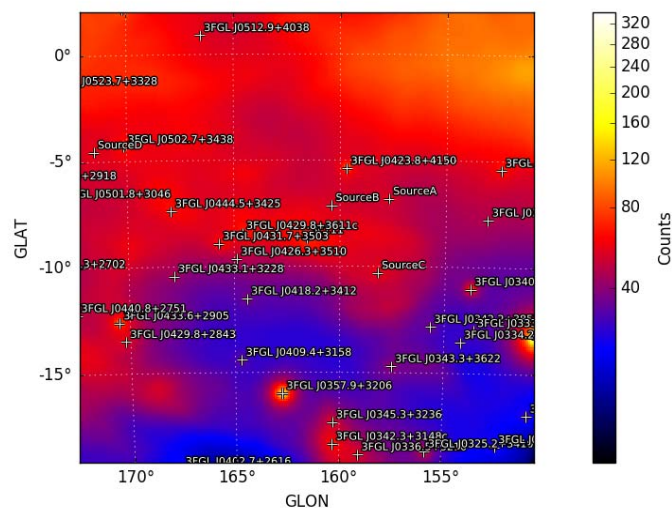
FIGURE 4.8: Count map of 3C 111 with the included sources.

The latest reprocessed Pass 8 events with energy between 90 MeV and 310 GeV and spacecraft data are used with the instrument response function P8R2 SOURCE V6 and

enabling energy dispersion correction. However, the likelihood analyses were restricted to 100 MeV - 300 GeV energy intervals. Only events with higher probability of being photons (evclass=128 evtype=3) are analyzed applying the standard cuts (e.g., the zenith angle larger than $90°$). The photons were downloaded from $10°$ around each source position taken from [48] (except for 3C 207, M87, the radius $12°$ is chosen to have better modeling of the region of interest (ROI)) and worked with a $90° \times 90°$ square ROI. The photons are binned with gtbin tool with a stereographic projection into pixels of $0.1° \times 0.1°$ and into 35 equal logarithmically spaced energy bins. The count maps of the 3C 111 and M87 includng ROI sources are presented in Fig. 4.8 and 4.9. The model file is created using the Fermi-LAT third source catalog [48] (3FGL) where all sources within ROI+5° region were included in the model file. For the Galactic and diffuse background models gll_iem_v05_rev1 and iso_source_v05 are used, currently recommended by LAT team. The normalization of background models as well as fluxes and spectral indices of the sources within ROI are left as free parameters in the analysis. In order to find the best matches between spectral models and events, the binned likelihood analysis is performed with *gtlike* and the detection significance is quantitatively estimated using the Test Statistics (TS), defined as $TS = 2(\log L - \log L_0)$, where L and L_0 are the likelihoods with an additional source and null hypothesis [136].

Using data from longer accumulation time than used in 3FGL, can result new γ-ray sources in the ROI which are not properly accounted in the model files. In order to probe for additional sources, a TS significance map of the ROI is created using the best-fit model. After subtracting the observed counts from the model map (constructed with the resulting likelihood model), if there are new sources with TS > 25 they are included in the source model file during data analysis, in addition to the 3FGL sources.

In the spectral analysis, initially the source spectra were modeled using Power-Law (PL) spectral shape. In case, the source spectrum shows deviation from simple PL modeling, more complex Power-Law with Exponential cut-off (PLEXP) or log parabolic (LP) shapes are considered. In order to check for statistically significant curvature in the spectrum, log likelihood ratio test was performed. After the likelihood fitting in the energy range between

0.1-300 GeV, the Spectral Energy Distribution (SED) of each source has been obtained by dividing the total interval into smaller bands and separately running *gtlike* for these intervals.
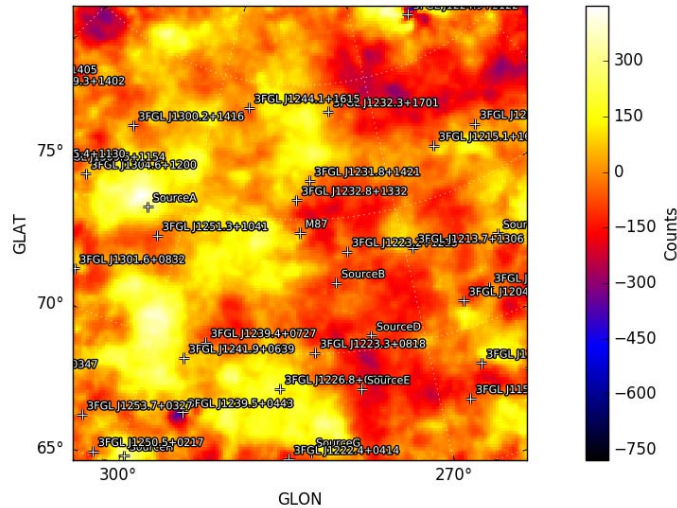
FIGURE 4.9: Count map of M87 with the included sources.

The X-ray Chandra data reduction and analysis have been performed, following the presented in section 2.2.4 using the CIAO 4.8 with CALDB version 4.7.2. For each knot and hotspot, the position and shape of the source region and the background are selected on the assumption of the previous studies. We extracted the spectra and created weighted response files for each observation, using the *specextract* script. The knots spectra were rebinned, using a different count threshold, depending on the total number of counts, and fitted in the 0.5-10 keV energy range using a power-law with the Galactic absorption model where the index and the normalization are allowed to vary freely. The spectral fit was done with Sherpa using the levmar optimization method and chi2datavar statistics.

4.4 Analysis results

The results from the current γ-ray data analysis are summarized in the Table 4.2. For each source the class, γ-ray photon index (Γ), flux (F_γ) (in the energy range from 90 MeV to 300 GeV), distance (*d*), γ-ray luminosity $\left(L_\gamma (erg\ s^{-1})\right)$ and TS are presented. Since reprocessed PASS 8 version of data is used, most of sources have been detected well above 5σ limit. The nearest source included in the sample is M87 (at $z = 0.00436$) while the farthest one is 3C

207 (at $z = 0.684$). The 7-years averaged γ-ray photon index ranges from 2.02 (for M87 and 3C 303) to as soft as 2.70 (for 3C 111). The luminosity of the considered sources varies in the range of $10^{41} - 10^{46}\ erg\ s^{-1}$ and the maximum γ-ray flux of $F_\gamma = (4.87 \pm 0.32) \times 10^{-8}$ photon $cm^{-2}s^{-1}$ observed for 3C 111.

TABLE 4.2: Results of the Fermi-LAT Data Analysis

Source	Class	Γ	$F_\gamma(> 90MeV)$ *	d(cm)	$L_\gamma(erg\ s^{-1})$	TS
M87	FRI	2.02 ± 0.04	$1.84 \pm 0.18 \times 10^{-9}$	5.68×10^{25}	8.18×10^{41}	1033.52
NGC 6251	FRI	2.35 ± 0.03	$2.81 \pm 0.15 \times 10^{-8}$	3.26×10^{26}	2×10^{43}	1001
3C 111	FRII	2.70 ± 0.05	$4.87 \pm 0.32 \times 10^{-8}$	6.32×10^{26}	8.2×10^{43}	254.75
3C 303	FRII	2.02 ± 0.19	$1.49 \pm 08 \times 10^{-9}$	1.84×10^{27}	7.16×10^{43}	26
Pictor A	FRII	2.53 ± 0.12	$1.38 \pm 0.37 \times 10^{-8}$	4.57×10^{26}	1.48×10^{43}	118.66
3C 207	SSRQ	2.63 ± 0.08	$1.58 \pm 0.23 \times 10^{-8}$	8.69×10^{27}	5.69×10^{45}	120.8
3C 275.1	SSRQ	2.47 ± 0.12	$1.1 \pm 0.24 \times 10^{-8}$	7.23×10^{23}	3.12×10^{45}	106

* $photon\ cm^{-2}s^{-1}$

The 7-years averaged spectra of all considered sources are better explained with power-law model and only NGC 6251 shows deviation from PL above several GeV. The log likelihood ratio test shows, that log parabola in the form of $dN/dE_\gamma = N_0\left(E_\gamma/E_b\right)^{-\alpha - \beta\log\left(E_\gamma/E_b\right)}$, where, N_0, α and β are free parameters, explains better the data. The corresponding SED is shown in Fig. 4.10.
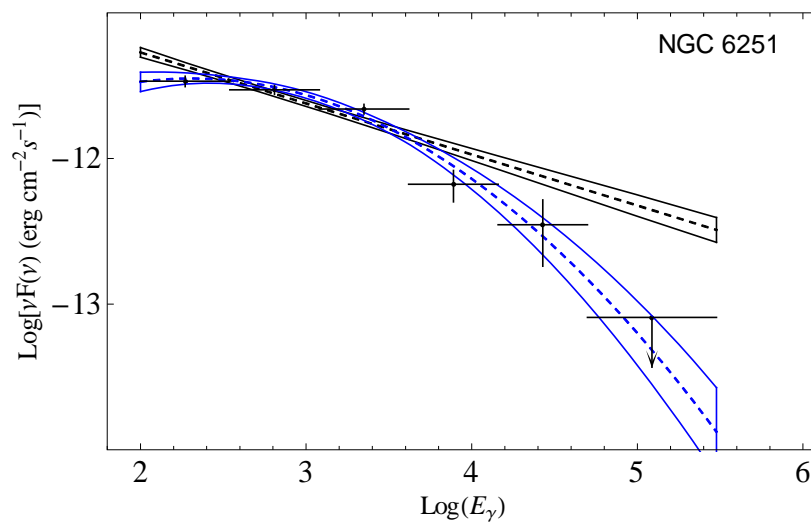

FIGURE 4.10: The SED of NGC 6251 in the range from 100 MeV to 300 GeV explained with Power-Law (black) and Log parabola (blue) models.

The Chandra X-ray data analysis results of the considered sources are presented in Table 4.3.

Table 4.3: The Chandra X-ray data analysis results of the knots and hotspots

	Γ	K $\times 10^{-6}\ photons\ s^{-1} keV^{-1}$	νF_{ν} $\times 10^{-14}\ erg\ cm^{-2} s^{-1}$	reduced χ^2
M 87				
HST1	2.36±0.02	244.1±2.166	92.01±1.20	1.01
D	2.12±0.01	132.7±0.85	57.84±0.68	1.10
E	2.48±0.02	29.55±0.45	10.05±0.19	0.93
F	2.85±0.05	15.4±0.35	4.84±0.13	0.89
I	2.38±0.11	7.99±0.11	2.99±0.12	1.09
A	2.38±0.01	173.49±0.93	64.49±0.13	1.07
B	2.64±0.04	18.96±0.38	6.31±0.15	1.04
C	1.9±0.04	12.75±0.37	1.0±0.014	0.92
PictorA				
A	1.87±0.07	4.99±0.24	2.66±0.24	0.83
B	2.02±0.17	1.78±0.18	0.84±0.14	0.73
C	1.81±0.10	2.86±0.19	1.61±0.21	0.93
D	1.83±0.12	2.67±0.21	1.48±0.19	0.94
WHS	1.93±0.01	131.56±0.89	67.08±1.50	1.01
3C 303				
WHS	1.51±0.32	6.73±1.28	5.18±1.80	0.84
3C 275.1				
NHS	1.67±0.30	3.16±0.58	2.04±0.68	0.64
NGC 6251				
A	1.61±0.46	1.59±0.5	1.07±0.5	0.91
B	2.02±0.44	1.28±0.37	0.62±0.2	0.81
C	2.29±0.28	2.21±0.38	0.87±0.19	0.72
3C 207				
A	1.14±0.16	3.61±0.51	4.01±0.84	0.86
B	1.15±0.17	3.08±0.47	3.58±1.51	1.00
HS	1.38±0.38	0.79±0.26	0.99±0.49	0.71
3C 111				
k9	0.71±0.09	5.09±0.57	12.14±0.57	0.90
k14	0.97±0.21	1.73±0.41	2.69±0.9	0.85
k22	0.65±0.3	0.748±0.32	1.86±0.8	1.1
k30	0.99±0.16	2.78±0.51	4.32±1.01	0.91
k38	1.27±0.55	1.03±0.51	1.06±0.6	0.62
k45	1.29±0.57	0.836±0.46	0.83±0.42	0.93
k51	1.28±0.69	0.56±0.31	0.81±0.51	0.53
k61	1.23±0.13	6.41±0.82	6.89±1.57	0.81
k97	2.07±0.67	0.91±0.37	0.40±0.17	1.09
NHS	1.41±0.24	2.21±0.51	1.92±0.65	0.91
SHS	0.89±0.77	0.59±0.47	2.71±2.01	0.97

For each source knots, the flux and photon index measured in the energy range from 0.5 to 10 keV, the corresponding luminosity, and reduced Chi2 are presented. The results of the individual knot studies are not discussed here because our prime task is to investigate the origin of emission within these knots but below we have mentioned several interesting results. First of all, it is interesting that many knots have the hard spectra in the X-ray band which indicates that the emission spectra $\nu F\nu$ representation is rising so cannot be explained by the extrapolation of synchrotron emission responsible for the low energy emission. The cases when X-ray emission defines the HE tail of synchrotron component are also important, as it allows to estimate the highest energies in the underlying electrons, thus to understand the acceleration and cooling processes but the hard spectrum needs to be explained taking into account the contribution from other emission components.

The highest X-ray flux has been observed from the HST1 knot of M87 source and corresponds to $(92.01 \pm 1.2) \times 10^{-14}\ erg\ cm^{-2}s^{-1}$. It is important to highlight the X-ray emission from large scale jet of 3C 111, except k97 from all other knots the X-ray spectra has very hard X-ray spectra implying there is effective particle acceleration along the jet.

In order to study the properties of the kpc scale jets in the X-ray band we have selected three candidate sources (M87, 3C 111 and Pictor A), which have peculiar large scale structure (knots, hotspots) resolved by Chandra.
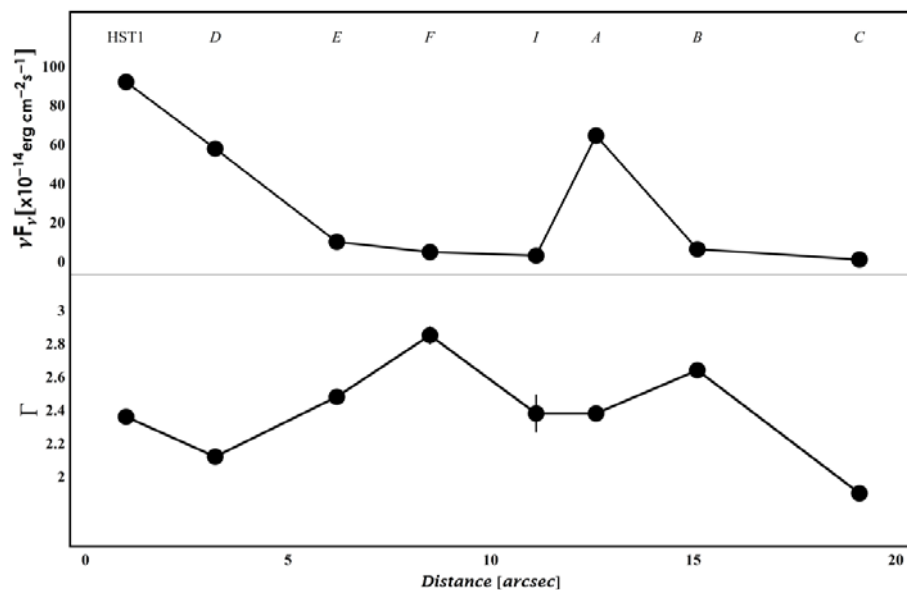

Fig. 4.11: The changes of the flux density (top panel) and power-law photon indices (bottom panel) along the jet in the X-ray 0.5–10 keV band along the jet of M87. The knot regions are mentioned above.

The first source is M87, which has eight knots detected and well studied in the X-ray band. In Fig. 4.11 is depicted the flux and photon index changes based on the best-fit results of the M87 knots observations in different distances from the central source. As we can see the nearest knot HST1 is the brightest, and the photon flux corresponds $F_X = (92.01 \pm 1.2) \times 10^{-14} \ erg \ cm^{-2} s^{-1}$ with the photon index $\Gamma_X = 2.36 \pm 0.02$. Afterwards, the jet radiation gradually decreases up to knot A. In the knot A which is the second bright knot the particles are accelerated more efficiently and the X-ray flux increases up to $F_X = (64.49 \pm 0.13) \times 10^{-14} \ erg \ cm^{-2} s^{-1}$ with photon index $\Gamma_X = 2.38 \pm 0.01$.

One of the most interesting structures has the 3C 111 radiogalaxy. The jet of 3C 111 expands over 100 kpc, including nine knots (k9, k14, k22, k38, k45, k51, k61 and k97) and two (the northern (NHS) and southern (SHS) hotspots regions. As depicted in Fig. 4.12, the results are indicates that along jet of the 3C 111 radiogalaxy, $\Gamma_X < 2$, which shows that the HE electrons are responsible for the emission along the jet. In particular, the X-ray photon indices of $\Gamma_X < 1.41$ (for k97 knot) was measured which indicate that particles should be accelerated inside k97, otherwise if the electrons are only accelerated in one region, they cannot travel up to the extended regions, due to energy lose. Thus, 3C 111 is one of the unique radio galaxies in the radiation and acceleration mechanism in small and large scale structures can be studied.
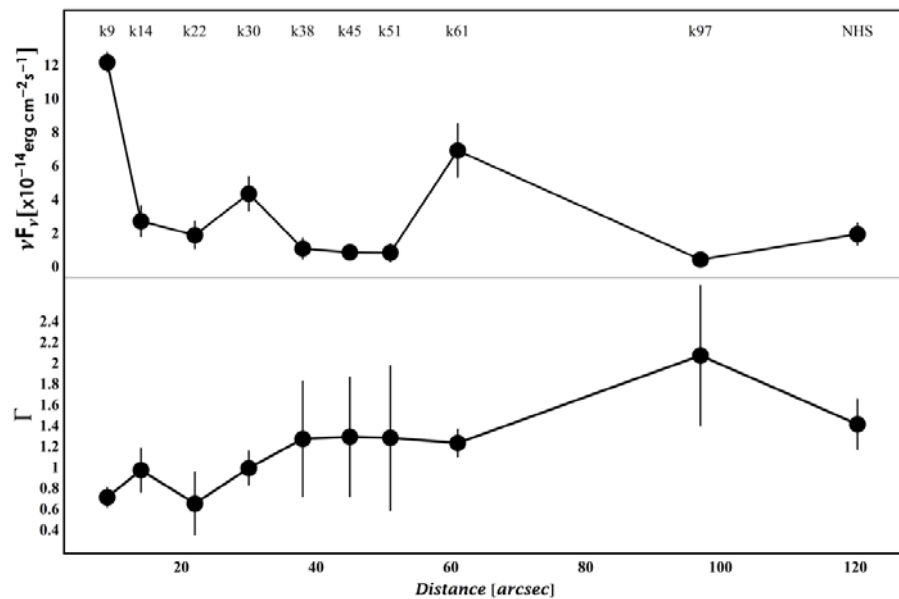
Fig. 4.12: The changes of the flux density (top panel) and power-law photon indices (bottom panel) in the X-ray 0.5–10 keV band along the jet of 3C 111. The knot regions are mentioned above.

The jet of Pictor A is about 200 kpc and based on the previous studies we separate four knots regions (A, B, C, D) in order to study the emission from the jet. The evolution of the jet of Pictor A, up to D knot (approximately 100 arsec) is shown in Fig. 4.13. The results show that the X-ray photon index is always about $\Gamma \approx 1.9$ and the photon flux varies between $F_X = (0.8 - 2.16) \times 10^{-14} \, erg \, cm^{-2} s^{-1}$ for the all knots along the jet. Probably this indicates that the same radiation and acceleration mechanisms are responsible for the X-ray emission along the whole jet, which is similar with the results of [105].
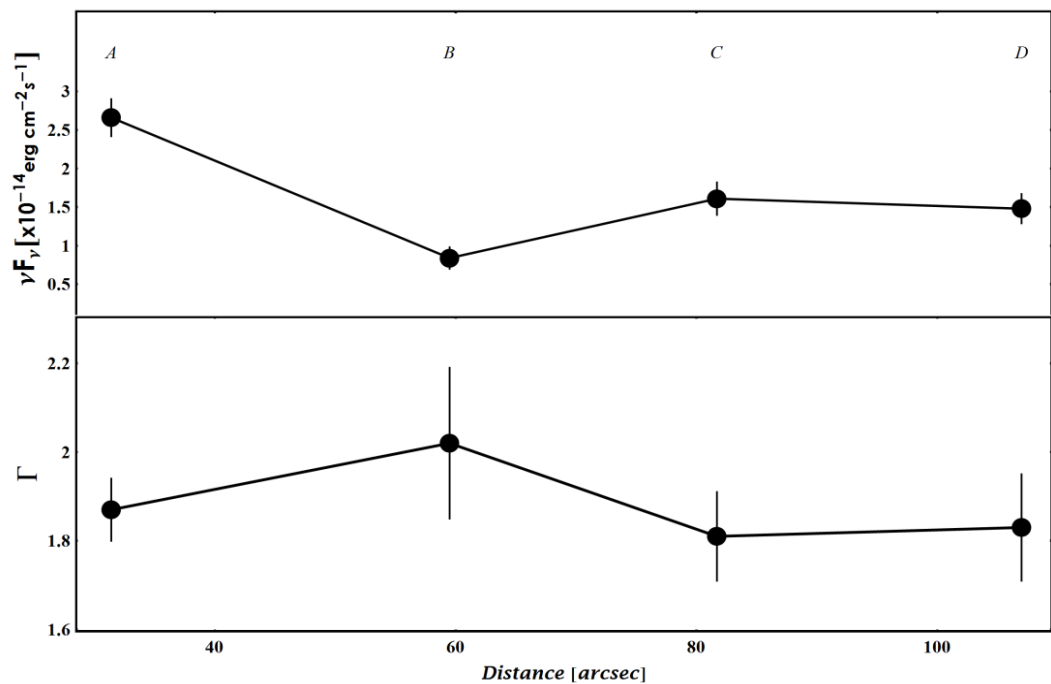
Fig. 4.13: The changes of the flux density (top panel) and power-law photon indices (bottom panel) in the X-ray 0.5–10 keV band along the jet of Pictor A. The knot regions are mentioned above.

4.5 Theoretical modeling the spectral energy distributions

Below the emission from both nuclear (radio through $\gamma - ray$) and knots (radio through $X - ray$) are modeled. The spectral energy distribution modeling is a technique that is used to make a conclusion of the physical properties of the AGNs, as well as particle acceleration and radiation mechanisms from the large scale jets.

4.5.1 The Core region

The multiwavelength emission of the cores of considered radio galaxies is modeled using the synchrotron/SSC model. The radio through optical emission is due to the synchrotron emission of energetic electrons in the homogeneous, randomly oriented magnetic field, while the X-ray to HE γ-ray emission is due to the inverse Compton scattering of the same synchrotron photons.

The emission region (the "blob") is assumed to be a sphere with a radius of R which carries a magnetic field with an intensity of B and a population of relativistic electrons which have a power-law with an exponential cut-off energy distribution expected from shock acceleration theories:

$$N'_e(E'_e) = N'_0 \left(\frac{E'_e}{m_e c^2} \right)^{-\alpha} Exp\left[-\frac{E'_e}{E'_{cut}} \right]$$ (4.1)

For $E'_{min} \leq E'_e \leq E'_{max}$, where E'_{min} and E'_{max} are the electron maximum and minimum energies respectively. The total electron energy $U_e = \int_{E'_{min}}^{E'_{max}} E'_e N'_e(E'_e) dE'_e$ is defined by N'_0, α is the electron spectral index, and E'_{cut} in the cutoff energy.

Since the blob moves along the jet with a bulk Lorentz factor of Γ_{bulk}, the radiation will be amplified by a relativistic Doppler factor of $\delta = 1/\Gamma_{bulk}(1 - \beta \cos[\theta_{obs}])$, where θ_{obs} is the angle between the bulk velocity and the line of sight. During the modeling of emission from all sources considered here, a characteristic value for radio galaxies, δ = 4 was used.

4.5.2 Large-scale jets

The SED of the knots discussed here are presented in Fig. 4.14–4.17. For some sources, the emission from radio to X-ray bands can be interpreted with a single component, whereas sometimes the X-ray flux is well above the extrapolation from the radio-to-optical spectra and it hardens. This indicates that two components are necessary to explain the radio to optical and X-ray emission from the knots.

The radio to optical emission from the knots is believed to be synchrotron emission of the relativistic non-thermal electrons in the magnetic field. This is also supported by the detection of highly polarized emission in the radio and optical bands. The radiation mechanism usually considered to explain the origin of X-ray emission is either the

synchrotron emission from a second much more energetic population of electrons (e.g., Ref. [9,10]) or the inverse Compton scattering on various possible sources of soft photons, including the synchrotron photons (SSC; e.g., [13]) and the cosmic microwave background photons (IC/CMB: e.g., [14]). In the case of SSC scenarios, since the luminosity in the X-ray band (L_{X-ray}, SSC) should exceed the one observed in the radio band L_{radio}, it is satisfied only when $U_B \leq U_{syn}$. Therefore the observed emission can be accounted for only if the particle energy (U_e) strongly dominates over the magnetic field thus contravening the equipartition condition. Because of this, we only consider (1) the inverse Compton scattering of CMB photons and (2) synchrotron emission from a second much more energetic population of electrons. In the IC/CMB scenario, it is assumed that the emitting region moves with a relativistic bulk Lorentz factor of Γ_{bulk} in order to predict a larger X-ray luminosity, since in the jet frame the energy density of CMB photons will be enhanced by a factor of Γ_{bulk}^2. Usually the Γ_{bulk} (or δ) are not well known for most of the sources. Thus, for each source we used δ (given in Table 4.4) for which the condition of $L_{X-ray} > L_{radio}$ is satisfied. In contrast, if the X-ray emission is produced by synchrotron radiation from a second population of relativistic electrons with very high maximum energy, it is not required to have a highly relativistic jet, and we assume $\delta = 1$. Since the electrons with high maximum energy would cool down quickly, then they must have been produced in a separate episode of acceleration, which occurred more recently. Moreover, the second population of electrons can be produced in different parts of the knot. We do not go much into details, but assume that there are two different electron populations responsible for the emission.

In the IC/CMB scenario the underlying electron distribution is given by Eq. 4.1 where the cutoff energy allowed to vary only the cases when the optical flux constrains the HE tail of synchrotron emission, while for the other cases it is fixed at $E_{cut} = 100\,GeV$ enough to produce photons up to X-ray band. In addition to this spectrum, a power-law distribution in the form of $N \sim E^{-\alpha_{PL}}$ is added to model the X-ray spectrum in the two-component synchrotron scenario. Since the data are not enough to constrain $E_{max,PL}$ an artificial HE limit of $E_{max,PL} = 1$ PeV has been introduced, whereas $E_{min,PL}$ is left as a free parameter

only ensuring that the flux from the second component does not exceed the first one. To make the deviation from the equipartition condition as less as possible, we define $\eta = U_e/U_B$, which is used as a free parameter with U_e during the fit. This will allow to find the optimum value for η when $\eta = 1$ does not give a satisfactory representation of the data. In the two-component synchrotron model we fix $\eta = 1$ and perform fitting of the radio-to-optical data. Then, fixing this magnetic field, the X-ray data are fitted with the second component.

As in the previous section the model free parameters of both core and knot emissions are estimated using MCMC methods. In the parameter sampling the following expected ranges are considered: $1.5 \leq (\alpha, \alpha_{PL}) \leq 10$, $0.511 \, MeV \leq E'_{cut} \leq 1 \, TeV$ and N_0 and B are defined as positive parameters.

4.6 Results and Discussion

The results of modeling of broadband emission from the core, knots and hotspots of M87, PictorA, NGC 6251 and 3C 111 are shown in Fig. 4.14-4.17 and the corresponding parameters are presented in Table 4.4.
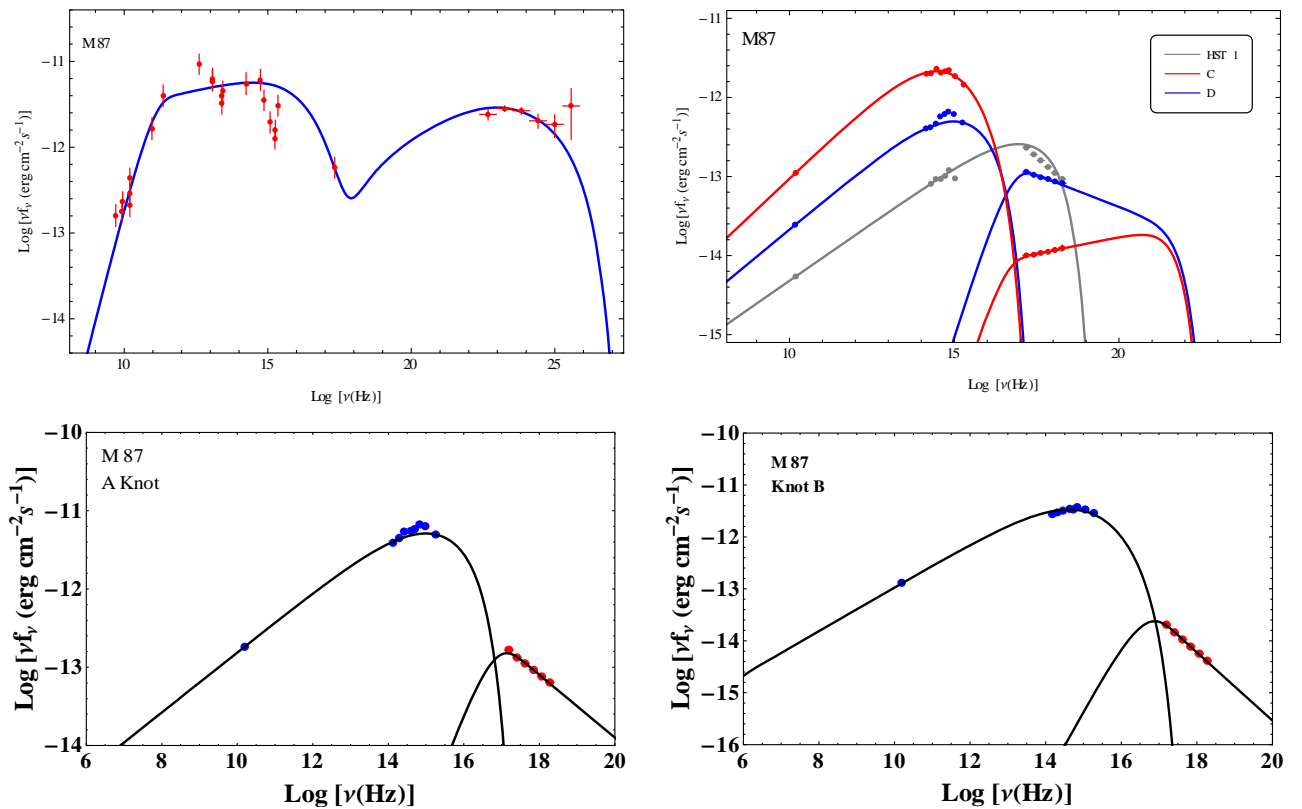
FIGURE 4.14: The modeling of broadband emission from the core and HST1, C, D, A and B knots of M87.

The photon index in the γ-ray band is usually $\Gamma \geq 2.4$. The cutoff energy is above several GeV with the highest cut-off energy of $\simeq 317.3$ GeV required for M87, since its emission extends above 100 GeV. The magnetic field varies between $B \simeq (0.3 - 100)\, mG$ a typical value usually used in the modeling of emission from the radio galaxies, and the system is close to equipartition condition with $\eta \simeq (10 - 600)$. Both the two-component synchrotron and IC/CMB models can satisfactorily reproduce the observed data. However, since the emission observed from M87 has a photon index of $\Gamma_X = (1.9 - 2.8)$, then it can be fitted with the two-component synchrotron model only. When the X-ray emission is interpreted as IC scattering of CMB photons with an energy density of $\simeq 4.0 \times 10^{-13}(1 + z)^4 erg$, it is required that the jet remains relativistic far from the nuclear region, with $\delta = 8$ in some cases. For most of the knots, the power-law index of electrons, defined by the radio and X-ray data, varies from 2.1 to 2.8. The only exceptions are the SHS hot spot and the k45 knots of 3C 111, which have $\alpha = (1.42 \pm 0.005)$ and 1.85 ± 0.005, respectively. The cut-off energy (when it can be estimated from the data) is $\geq 1\, TeV$, implying there is effective particle acceleration above TeV energies.
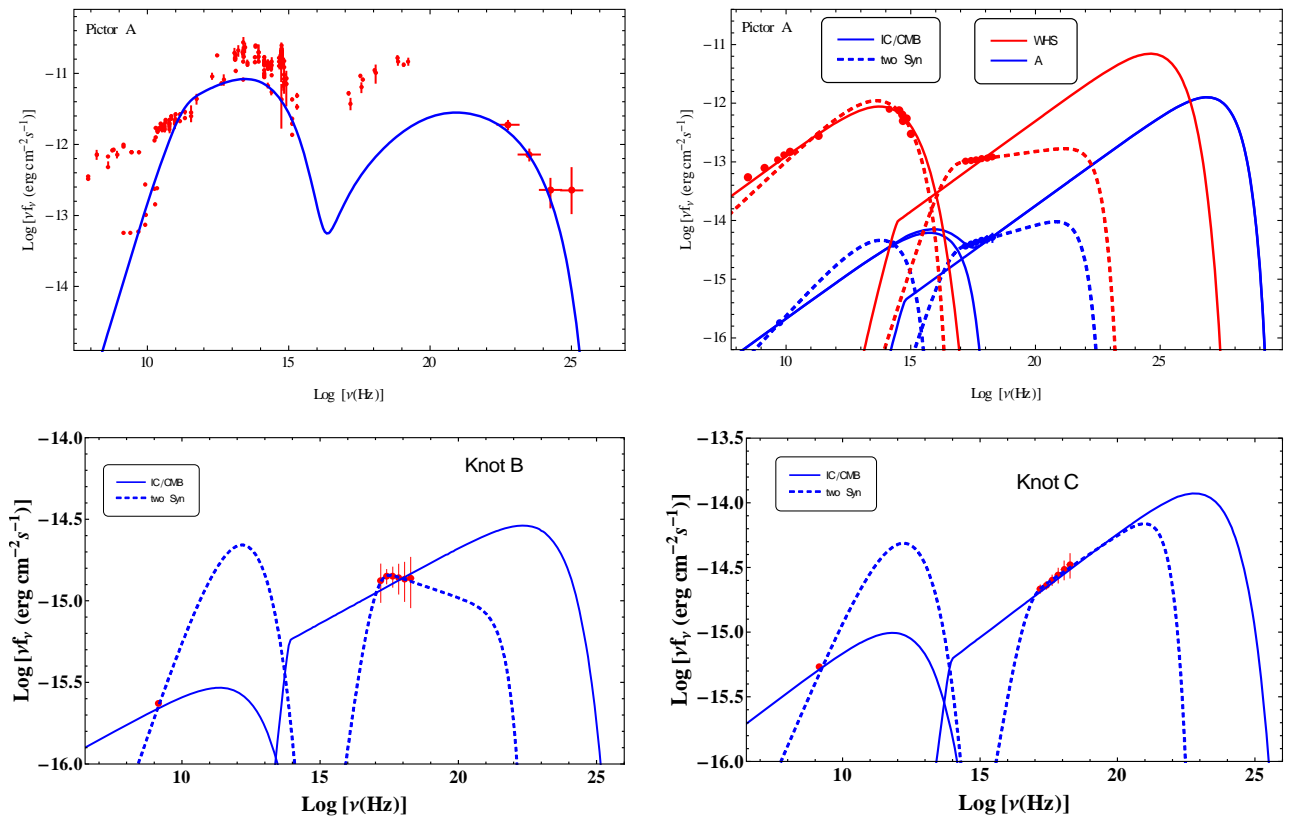
FIGURE 4.15: The modeling of broadband emission from the core, WHS hotspot, knot A, B and C of Pictor A.

The estimated magnetic field varies within $B \simeq (1.0 - 20)\mu G$. In the case of the two-component synchrotron model, the power-law index of electrons (responsible for radio to optical emission) is mostly defined by the radio data, changing from 2.03 to 2.85. The only exception is the k30 knot of 3C 111, which is modeled with $\alpha = 1.45 \pm 0.06$. Such a steep spectrum is necessary, since the peak of the first component should be around $10^{13} Hz$, otherwise it will overproduce the X-ray flux. As compared with the previous model, a larger magnetic field $B = (10 - 430)\,\mu G$ is needed. The synchrotron emission of the second population of electrons for the same magnetic field can explain the X-ray flux when $E_{\min} \simeq (2.03 - 331.1)\,TeV$ and $\alpha = (1.62 - 4.31)$. The particle energy density of this component is negligible as compared with the other one.
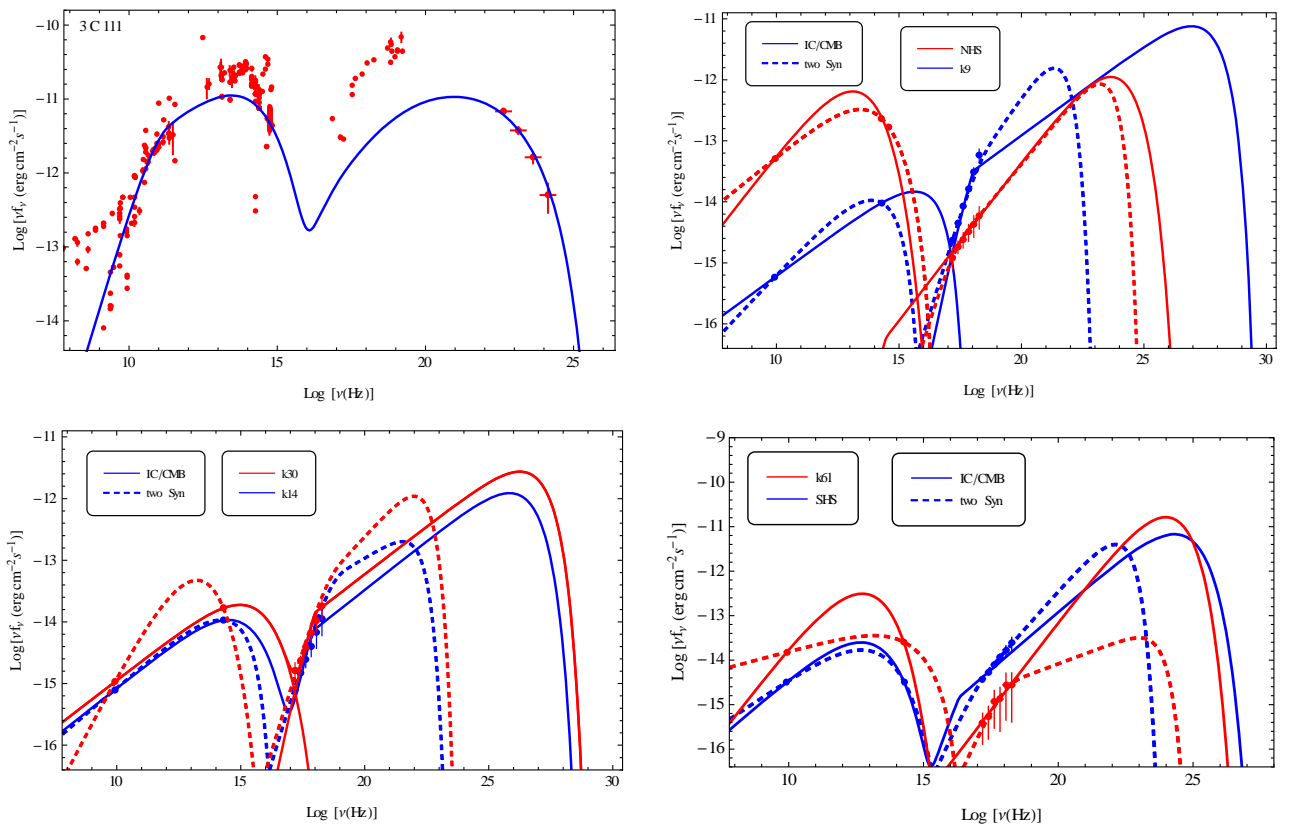
FIGURE 4.16: The modeling of broadband emission from the core, knot k9, k14, k30 k61 and NHS and SHS hotspots of 3C 111.

The fundamental quantity is the total power (particles + magnetic field) transported by the jet flow. The total jet power can be estimated using the parameters derived from the SED modeling using $L_e = \pi c R_b^2 \Gamma^2 U_e$ and $L_B = \pi c R_b^2 \Gamma^2 U_B$ for electrons and magnetic field, respectively ($\Gamma = 1$ is assumed in the two-component synchrotron model). The protons with

unknown contribution to the jet have not been considered in the calculations since a number of assumptions need to be made. The emission from the core can be modeled using the jet luminosity from $L_{jet} = L_e + L_B \cong 5.1 \times 10^{43} \ erg \ s^{-1}$ to $2.65 \times 10^{45} \ erg \ s^{-1}$. When the jet power is estimated for the knots, in case of the beamed IC/CMB scenario, the total jet power should change from $7 \times 10^{43} erg \ s^{-1}$ to $10^{47} \ erg \ s^{-1}$ in order to explain the X-ray luminosity. In the two-component synchrotron model, the total jet luminosity is lower $\leq 5 \times 10^{46} erg \ s^{-1}$ but still does not differ by much as compared with the luminosity of the core.
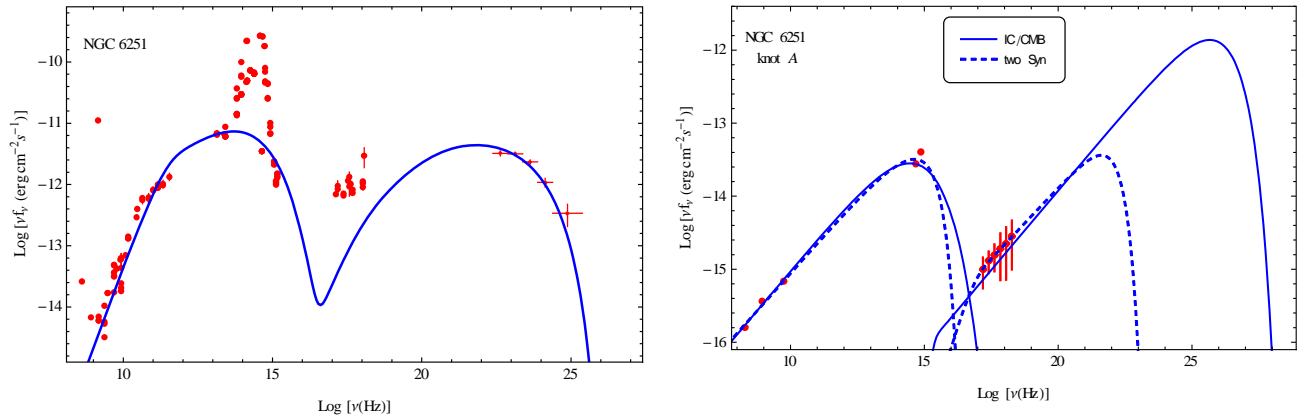
FIGURE 4.17: The modeling of broadband emission from the core and knot A of NGC 6251.

Table 4.4. The results of modeling of broadband emission from the core and knots/hotspots

	δ	α	E_{cut}(TeV)	(α'_p)	$(E'_{min,p} \text{TeV})$	B(μG)	η	$L_{jet} \times 10^{44}$ erg s^{-1}
				M 87				
core	4.0	$2.84^{+0.12}_{-0.11}$	$0.32^{+0.07}_{-0.10}$	-	-	3037.89^{+512}_{-465}	592.2	0.51
HST1	1.0	$2.42^{+0.0004}_{-0.0003}$	$10.48^{+0.34}_{-0.29}$	-	-	256.213	1.0	0.09
D	1.0	$2.31^{+0.0006}_{-0.0005}$	$0.78^{+0.006}_{-0.007}$	$3.32^{+0.01}_{-0.07}$	$3.01^{+0.016}_{-0.007}$	324.878	1.0	1.20
E	1.0	$2.36^{+0.002}_{-0.003}$	$2.01^{+0.11}_{-0.16}$	$4.07^{+0.03}_{-0.03}$	$3.03^{+0.05}_{-0.02}$	272.560	1.0	0.56
F	1.0	$2.19^{+0.1}_{-0.1}$	$0.59^{+0.04}_{-0.04}$	$4.86^{+0.06}_{-0.07}$	$3.04^{+0.07}_{-0.03}$	317.081	1.0	0.40
I	1.0	$2.25^{+0.025}_{-0.034}$	$0.66^{+0.19}_{-0.16}$	$3.82^{+0.09}_{-0.08}$	$3.23^{+0.33}_{-0.17}$	267.039	1.0	0.08
A	1.0	$2.23^{+0.0004}_{-0.0005}$	$0.74^{+0.003}_{-0.004}$	$3.8^{+0.014}_{-0.014}$	$3.21^{+0.02}_{-0.01}$	301.21	1.0	0.51
B	1.0	$2.14^{+0.0035}_{-0.0027}$	$0.33^{+0.0004}_{-0.0005}$	$4.31^{+0.06}_{-0.05}$	$2.16^{+0.16}_{-0.11}$	433.653	1.0	1.89
C	1.0	$2.21^{+0.0005}_{-0.0006}$	$0.4^{+0.002}_{-0.002}$	$2.83^{+0.07}_{-0.06}$	$2.64^{+0.55}_{-0.72}$	278.65	1.0	3.05
				PictorA				
core	4.0	$2.47^{+0.018}_{-0.011}$	$0.008^{+0.001}_{-0.001}$	-	-	34862.57^{+4440}_{-3593}	11.6	1.42
A	8.0	$2.38^{+0.0041}_{-0.0053}$	$10.87^{+1.21}_{-1.11}$	-	-	1.644	$23.68^{+2.23}_{-1.91}$	5.56
	1.0	$2.07^{+0.015}_{-0.017}$	$0.799^{+0.042}_{-0.043}$	$2.75^{+0.11}_{-0.09}$	$12.69^{+5.16}_{-5.45}$	11.818	1.0	1.82
B	8.0	$2.81^{+0.15}_{-0.16}$	0.1	-	-	8.902	$1.45^{+0.26}_{-0.21}$	127.89
	1.0	2.0	0.1	$3.11^{+0.38}_{-0.26}$	$17.51^{+6.96}_{-8.56}$	13.64	1.0	1.92

C	8.0	$2.67^{+0.11}_{-0.18}$	0.1	-	-	8.1165	$1.38^{+0.14}_{-0.11}$	163.90
	1.0	2	0.1	$2.71^{+0.15}_{-0.14}$	$12.33^{+4.84}_{-4.81}$	15.21	1.0	3.78
D	8.0	$2.86^{+0.045}_{-0.035}$	$0.68^{+0.353}_{-0.271}$	-	-	2.18721	$11.67^{+1.17}_{-1.03}$	61.63
	1.0	$2.026^{+0.023}_{-0.025}$	$0.92^{+0.01}_{-0.05}$	$2.78^{+0.22}_{-0.18}$	$21.13^{+10.16}_{-9.011}$	5.3487	1.0	0.45
WHS	8.0	$2.38^{+0.052}_{-0.035}$	$0.42^{+0.054}_{-0.021}$		-	9.97	$3.12^{+0.65}_{-1.02}$	32.57
	1.0	$2.21^{+0.041}_{-0.028}$	$0.37^{+0.024}_{-0.017}$	$2.88^{+0.64}_{-0.73}$	$5.81^{+0.64}_{-0.73}$	45.92	1.0	10.48
3C 303								
core	4.0	$2.69^{+0.06}_{-0.03}$	$0.0083^{+0.0009}_{-0.0003}$	-	-	64159.99^{+3049}_{-1387}	11.6	4.38
WHS	2.0	$2.58^{+0.0006}_{-0.0005}$	$1.547^{+0.0326}_{-0.0227}$	-	-	6.16	$26.65^{+3.39}_{-2.31}$	88.70
	1.0	$2.62^{+0.014}_{-0.025}$	$0.928^{+0.083}_{-0.131}$	$2.38^{+0.90}_{-0.51}$	$14.98^{+8.11}_{-9.42}$	48.45	1.0	78.80
3C 275.1								
core	4.0	$2.07^{+0.003}_{-0.003}$	$0.004^{+0.00004}_{-0.00005}$	-	-	77135.54^{+2081}_{-1706}	45.6	26.47
NHS	2.0	$2.19^{+0.095}_{-0.053}$	$0.19^{+0.007}_{-0.008}$	-	-	8.47	1.0	333.44
	1.0	$2.75^{+0.033}_{-0.041}$	$0.257^{+0.033}_{-0.041}$	$2.30^{+0.0011}_{-0.0011}$	$4.63^{+0.25}_{-0.29}$	51.42	1.0	915.44
NGC 6251								
core	4.0	$2.28^{+0.09}_{-0.13}$	$0.01^{+0.0014}_{-0.0015}$	-	-	15730.22^{+642}_{-258}	47.0	1.34
A	8.0	$2.13^{+0.0009}_{-0.0001}$	$1.084^{+0.015}_{-0.021}$	-	-	3.85	$10.05^{+1.15}_{-0.96}$	0.54
	1.0	$2.17^{+0.016}_{-0.021}$	$2.08^{+0.314}_{-0.172}$	$2.22^{+0.0017}_{-0.0021}$	$10.12^{+0.17}_{-0.16}$	34.24	1.0	0.24
3C 207								
core	4.0	$2.77^{+0.08}_{-0.11}$	$0.01^{+0.004}_{-0.004}$	-	-	105577^{+10107}_{-10265}	15.0	17.17
A	5.0	$1.98^{+0.201}_{-0.152}$	$0.145^{+0.02}_{-0.01}$	-	-	3.23	$69.33^{+10.54}_{-7.391}$	221.93
	1.0	$2.64^{+0.202}_{-0.228}$	$0.15^{+0.02}_{-0.02}$	$2.31^{+0.85}_{-0.54}$	$18.41^{+12.75}_{-10.64}$	79.84	1.0	226.11
B	2.0	$2.29^{+0.033}_{-0.036}$	$0.12^{+0.006}_{-0.003}$	-	-	7.53	$41.77^{+2.81}_{-2.03}$	1106.46
	1.0	$2.58^{+0.011}_{-0.003}$	$0.09^{+0.0006}_{-0.0007}$	$2.19^{+0.89}_{-0.40}$	$13.39^{+10.74}_{-9.012}$	65.26	1.0	770.20
HS	2.0	$2.35^{+0.002}_{-0.001}$	$0.11^{+0.002}_{-0.001}$	-	-	20.54	$1.98^{+0.27}_{-0.16}$	286.13
	1.0	$2.35^{+0.007}_{-0.001}$	$0.09^{+0.0002}_{-0.0005}$	$2.85^{+0.73}_{-0.67}$	$13.42^{+10.82}_{-8.881}$	56.339	1.0	286.77
3C 111								
core	4.0	$2.34^{+0.03}_{-0.03}$	$0.007^{+0.0005}_{-0.0004}$	-	-	32189.28^{+1453}_{-1677}	41.0	4.20
k9	8.0	$2.41^{+0.0041}_{-0.0035}$	$13.49^{+1.85}_{-1.61}$	-	-	1.05	$47.01^{+3.82}_{-2.93}$	2.89
	1.0	$2.14^{+0.019}_{-0.018}$	$0.911^{+0.066}_{-0.061}$	$1.8^{+0.55}_{-0.22}$	$89.97^{+7.492}_{-11.79}$	13.78	1.0	0.65
k14	8.0	$2.36^{+0.007}_{-0.009}$	$1.94^{+0.15}_{-0.14}$	-	-	2.59	$22.09^{+2.37}_{-2.36}$	25.37
	1.0	$2.31^{+0.015}_{-0.012}$	$0.98^{+0.087}_{-0.082}$	$2.51^{+0.7}_{-0.9}$	$2.03^{+0.23}_{-0.21}$	36.81	1.0	6.12
k22	6.0	$2.58^{+0.008}_{-0.007}$	$3.52^{+0.32}_{-0.37}$	-	-	5.84	$41.54^{+4.11}_{-4.38}$	10.51
	1.0	$2.502^{+0.01}_{-0.01}$	$0.99^{+0.059}_{-0.065}$	$2.73^{+0.81}_{-0.81}$	$331.07^{+369.2}_{-222.3}$	31.43	1.0	6.03
k30	8.0	$2.39^{+0.007}_{-0.006}$	$3.85^{+0.43}_{-0.39}$	-	-	2.78	$7.68^{+0.71}_{-0.72}$	22.48
	1.0	$1.454^{+0.057}_{-0.071}$	$0.18^{+0.013}_{-0.014}$	$2.13^{+0.57}_{-0.48}$	$99.09^{+158.41}_{-46.782}$	18.57	1.0	1.81
k38	4.0	$2.23^{+0.0307}_{-0.0272}$	$0.64^{+0.044}_{-0.047}$	-	-	2.46	$4.62^{+0407}_{-0.384}$	2.86
	1.0	$2.401^{+0.017}_{-0.012}$	$0.92^{+0.06}_{-0.05}$	$1.73^{+0.015}_{-0.014}$	$23.41^{+0.58}_{-0.56}$	17.26	1.0	0.67
k45	4.0	$1.85^{+0.005}_{-0.005}$	$0.32^{+0.0009}_{-0.0011}$	-	-	1.12	$64.19^{+3.51}_{-3.59}$	3.08
	1.0	$2.106^{+0.033}_{-0.034}$	$0.27^{+0.008}_{-0.009}$	$2.73^{+0.89}_{-0.92}$	$150.58^{+362.3}_{-107.4}$	12.36	1.0	0.95
k51	4.0	$2.42^{+0.007}_{-0.009}$	$1.287^{+0.04}_{-0.06}$	_	_	10.40	$2.61^{+0.12}_{-0.13}$	0.72
	1.0	$2.34^{+0.016}_{-0.022}$	$0.819^{+0.0486}_{-0.0567}$	$2.86^{+0.77}_{-0.93}$	$154.07^{+449.9}_{-121.4}$	15.91	1.0	1.18
k61	8.0	$1.95^{+0.03}_{-0.34}$	$0.16^{+0.0044}_{-0.0049}$	-	-	1.78	$8.48^{+0.75}_{-0.71}$	49.11
	1.0	$2.19^{+0.058}_{-0.052}$	$0.19^{+0.008}_{-0.011}$	$1.623^{+0.32}_{-0.24}$	$19.77^{+11.55}_{-11.35}$	19.24	1.0	60.30
k97	2.0	$2.85^{+0.003}_{-0.004}$	$9.14^{+1.36}_{-1.65}$	-	-	11.48	$23.33^{+3.23}_{-3.55}$	121.06
	1.0	$2.64^{+0.014}_{-0.019}$	$0.39^{+0.025}_{-0.022}$	$3.26^{+0.47}_{-0.59}$	$5.45^{+3.59}_{-5.72}$	66.26	1.0	41.39

NHS	4.0	$1.96^{+0.051}_{-0.102}$	$0.156^{+0.02}_{-0.01}$	-	-	11.25	$1.03^{+0.10}_{-0.13}$	11.83
	1.0	$2.34^{+0.0021}_{-0.0026}$	$0.36^{+0.0031}_{-0.0037}$	$2.02^{+0.522}_{-0.341}$	$16.04^{+9.95}_{-10.65}$	45.90	1.0	15.83
SHS	4.0	$1.42^{+0.003}_{-0.004}$	$0.151^{+0.00049}_{-0.00082}$	-	-	2.06	$26.95^{+1.59}_{-0.99}$	10.91
	1.0	$2.67^{+0.0051}_{-0.0092}$	$0.56^{+0.013}_{-0.019}$	$2.55^{+0.144}_{-0.324}$	$35.46^{+1.19}_{-2.71}$	45.66	1.0	30.13

CONCLUSION

In this thesis, the emission processes in large scale jets of several radio galaxies (M87, Pictor A, 3C 303, 3C 275.1, NGC 6251, 3C 207, 3C 111 and 3C 120) have been investigated. The radio galaxies (sub-class of AGNs) are among the brightest sources in the Universe. Compared with blazars, the studies of radio galaxies allow to investigate not only the emission from relativistic jets but also from other components (lobes, knots, middle relativistic plasma, etc.) which are crucial for understanding the physics of the AGNs. In the recent years, the availability of multiwavelength data allowed to make detailed study of the nonthermal processes in AGNs in general and radio galaxies in particular. The AGN studies are improved after the launch of several telescopes, such as Fermi LAT, Chandra, NuStar etc. The Fermi LAT provides continuous observation of sources, which are crucial for understanding the variable emissions from AGNs. The high quality NuStar observations significantly help to understand HE phenomena occurring in the core of AGNs while the exceptional angular resolution of Chandra allows to resolve the components in large scale jets and understand the emission processes in these components.

The main aim of this thesis is to estimate the main parameters of the extragalactic jets (e.g., luminosity, magnetic field, etc.) to compare these parameters in sub-parsec and kpc scales. For this purpose, the emissions from the radio galaxies observed in the γ-ray band which have large scale jet resolved by Chandra are investigated. For the considered sources, the data collected by Fermi LAT (γ-ray band) and Chandra (X-ray band) are analyzed together and the spectral energy distributions for the jet emission near the nucleus and farther from it are prepared using available multiwavelength data. These SEDs are modeled using a leptonic synchrotron and inverse Compton models, taking into account the seed photons originating inside and outside of the jet. The model parameters were estimated using the Markov Chain Monte Carlo methods. The jet main parameters in the innermost ($\leq$ pc) and outer ($\geq$ kpc) regions of the jets are estimated by means of a detailed theoretical modeling. This comparison can greatly help to understand the evolution and propagation of the jets from central engine to kpc regions.

In Chapter 1, the main unification theory of AGNs is presented discussing the main difference in AGNs of different types. The jets of AGNs with their main structure and components are also presented. Briefly, the main radiation processes (synchrotron emission and inverse Compton scattering) their cross sections, cooling times, spectra etc. are presented.

In Chapter 2, the Fermi LAT data extraction and the likelihood analyses methods are described providing detailed information on the data analyses steps (e.g., spectral and temporal analyses, light curve preparation etc.). The Chandra X-ray data analyses methods are presented, providing details on data extraction, preparation, source and background regions selections, spectral analyses with Sherpa, etc.

In chapter 3, the main properties of the powerful jet of 3C 120 are investigated using the multiwavelength data (Swift XRT/UVOT, Fermi LAT and Chandra data) from the jet observations on sub-pc and kpc scales. On April 24, 2015, the γ-ray emission from the innermost jet of 3C 120 was observed when within 19.0 min and 3.15 hours the flux was as high as $(7.46 \pm 1.56) \times 10^{-6} \, photon \, cm^{-2} s^{-1}$ and $(4.71 \pm 0.92) \times 10^{-6} \, photon \, cm^{-2} s^{-1}$ above 100 MeV which corresponds to an isotropic γ-ray luminosity of $(1.2 - 1.6) \times 10^{46} erg \, s^{-1}$. Such luminosity is unusual for radio galaxies and more typical for BL Lacs. The synchrotron/SSC mechanism can reasonably explain the multiwavelength emission in the quiescent and flaring states while in the flaring state an additional contribution from the external photon fields cannot be rejected. The necessary jet kinetic power is $L_{jet} \simeq (1.31 - 48.0) \times 10^{44} \, erg \, s^{-1}$. The X-ray emission from the knots has a hard photon index of $\simeq (1.6 - 1.8)$ with a luminosity of $L \simeq (1.0 - 4.01) \times 10^{41} \, erg \, s^{-1}$. This X-ray emission can be explained by IC/CMB models only if the jet Doppler boosting factor is δ > 10. If the X-rays are produced from the direct synchrotron radiation of the second population of electrons, which are produced more recently than the cooler population responsible for the radio-to-optical spectrum, lower jet luminosity and no bulk relativistic motion on kpc scales is required.

In Chapter 4, using the multiwavelength observations of M87, Pictor A, 3C 303, 3C 275.1, NGC 6251, 3C 207 and 3C 111, the main jet parameters are estimated through the

theoretical modeling and the constraints on these physical parameters in the innermost (< pc) and outer (> kpc) regions of the same jet are compared. The results show that the jet luminosities of the innermost and outer regions are comparable, suggesting that the jet does not suffer important energy losses when propagating from the regions close to the black hole to those at hundreds of kiloparsecs from it. However, at larger distances the magnetic field and the particle energy density decrease, and the jet becomes radiatively inefficient.

BIBLIOGRAPHY

[1]   Begelman, M. C., Blandford, R. D. & Rees, M. J., "Theory of extragalactic radio sources", Reviews of Modern Physics, 1984, 56, p. 255–351.

[2]   Ambartsumyan, V. A., "Galaxies and their nuclei", Highlights of Astronomy, Vol. 3, p. 51 - 66

[3]   R. D. Blandford and R. L. Znajek, "Electromagnetic extraction of energy from Kerr black holes", Monthly Notices of the Royal Astronomical Society, 1977, 179, p. 433-456

[4]   Ambartsumian, V. A., "On the activity of galactic nuclei (introductory lecture)", "Non-stable Phenomena in Galaxies, proceedings of IAU Symposium No. 29, Byurakan, May 4-12, 1966. Published by "The Pubblishing House of the Academy of Sciences of Armenian SSR", Yerevan, 1968 (translated from Russian)., p.11

[5]   Urry, C. M. and Padovani, P., "Unified Schemes for Radio-Loud Active Galactic Nuclei", Publications of the Astronomical Society of the Pacific, 1995, v.107, p.803

[6]   Fanaroff, B. L. & Riley, J. M., "The morphology of extragalactic radio sources of high and low luminosity" Monthly Notices of the Royal Astronomical Society, 1974, 167, p. 31P-36P

[7]   V. Beckmann & C. Shrader 2012, "The AGN phenomenon: open issues", in proceedings of the 9th INTEGRAL Workshop, 2012, id. 69

[8]   Wilson, A. S., Young, A. J., & Shopbell, P. L., "Chandra X-Ray Observations of Pictor A: High-Energy Cosmic Rays in a Radio Galaxy", The Astrophysical Journal, 2001, Volume 547, Issue 2, pp. 740-753.

[9]   Harris, D. E., Mossman, A. E., & Walker, R. C., "The X-Ray Jet of 3C 120: Evidence for a Nonstandard Synchrotron Spectrum", The Astrophysical Journal, 2004 Volume 615, Issue 1, pp. 161-172

[10] Jester, S., Harris, D. E., Marshall, H. L., & Meisenheimer, K., "New Chandra observations of the jet in 3C 273. I. Softer X-ray than radio spectra and the X-ray emission mechanism", The Astrophysical Journal, 2006, 648, 900

[11] Marshall, H. L., Miller, B. P., Davis, D. S., et al., "A High-Resolution X-Ray Image of the Jet in M87", The Astrophysical Journal, 2002, Volume 564, Issue 2, pp. 683-687

[12] Röser, H.-J., Meisenheimer, K., Neumann, M., Conway, R. G., & Perley, R. A., "The jet of 3C 273 observed with ROSAT HRI", Astronomy and Astrophysics, 2000, Vol. 360, p.99-106

[13] Hardcastle, M. J., Birkinshaw, M., Cameron, R. A., et al., "Magnetic Field Strengths in the Hot Spots and Lobes of Three Powerful Fanaroff-Riley Type II Radio Sources", The Astrophysical Journal, 2002, v. 581, p. 948–973

[14] Tavecchio, F., Maraschi, L., Sambruna, R. and Urry, C., "The X-Ray Jet of PKS 0637-752: Inverse Compton Radiation from the Cosmic Microwave Background?", 2000, The Astrophysical Journal, Volume 544, Issue 1, pp. L23-L26

[15] Sahakyan, N.; Baghmanyan, V, Zargaryan, D., "Gamma-ray emission from non-blazar AGNs", American Institute of Physics Conference Proceedings, Volume 1792, Issue 1, id.050002, pp 1-6 , (2017); doi: 10.1063/1.4968948

[16] Sahakyan, N., Zargaryan, D. and Baghmanyan, V., "On the gamma-ray emission from 3C 120", Astronomy & Astrophysics, 2015, Volume 574, id.A88, 5 pp.

[17] Tanaka, Y. T., Doi, A., Inoue, Y., et al., "Six years of Fermi-LAT and multi-wavelength monitoring of the broad-line radio galaxy 3c 120: jet dissipation at sub-parsec scales from the central engine", The Astrophysical Journal Letters, 2015, 799, L18 (6pp)

[18] Zargaryan, D., "The gamma-ray emission from broad-line radio galaxy 3C 120", American Institute of Physic Conference Proceedings, Volume 1792, Issue 1, id.050008, pp 1-6, (2017); doi: 10.1063/1.4968954

[19] Zargaryan, D., Gasparyan, S., Baghmanyan, V., & Sahakyan, N., "Comparing 3C 120 jet emission at small and large scales", Astronomy & Astrophysics, 2017, Volume 608, id.A37, 10 pp.

[20] D. Zargaryan, N. Sahakyan, H. Harutyunian, "Chandra observations of gamma-ray emitting radio galaxies", Int. J. Mod. Phys. D, https://doi.org/10.1142/S0218271818440224

[21] Abdo, A. A., Ackermann, M., Ajello, M., et al., "Fermi Large Area Telescope Observations of Misaligned Active Galactic Nuclei", 2010a, The Astrophysical Journal, Volume 720, Issue 1, pp. 912-922

[22] Laing, R. A., "in Astrophysical Jets", ed. D. Burgarella, M. Livio, & C. P. O'Dea (Cambridge: Cambridge Univ. Press), 1993, 95

[23] Cohen, M.Yi., et al., "Radio sources with superluminal velocities", Nature, 1977, 268, p. 405-509

[24] Kellermann, K. L, Sramek, R., Schmidt, M., Shaffer, D. B., and Green, R., "VLA observations of objects in the Palomar Bright Quasar Survey, Astronomical Journal" (ISSN 0004-6256), 1989, vol. 98, Oct., p. 1195-1207.

[25] Khachikian, E. Y. and Weedman, D. W., "An atlas of Seyfert galaxies", Astrophysical Journal, 1974, vol. 192, Sept. 15, pt. 1, p. 581-589.

[26] R. A. Perley, A. G. Willis & J. S. Scott, "The structure of the radio jets in 3C 449", Nature, 11 October 1979, volume 281, pages 437–442

[27] Aharonian, F. A., "Proton-synchrotron radiation of large-scale jets in active galactic nuclei", Monthly Notices of the Royal Astronomical Society, 2002, Volume 332, pp. 215-230

[28] Aharonian F. A., Kelner S. R. & Prosekin A. Y., "Angular, spectral, and time distributions of highest energy protons and associated secondary γ rays and neutrinos propagating through extragalactic magnetic and radiation fields", Phys. Rev. D vol. 82, pp. 43002, 2010, 33, 34

[29] Blumenthal, G.R., Gould, R.J., "Bremsstrahlung, Synchrotron Radiation, and Compton Scattering of High-Energy Electrons Traversing Dilute Gases", Reviews of Modern Physics, (1970),42, p. 237–271

[30] Coppi, P.S., Blandford, R.D., "Reaction rates and energy distributions for elementary processes in relativistic pair plasmas", Monthly Notices of the Royal Astronomical Society, (1990), Vol. 245, p. 453-507

[31]   Atwood, W. B.; Abdo, A. A.; Ackermann, M.; Althouse, W. et al., "The Large Area Telescope on the Fermi Gamma-Ray Space Telescope Mission", The Astrophysical Journal, Volume 697, 2009, Issue 2, pp. 1071-1102.

[32]   Schwartz, D. A., "Invited Review Article: The Chandra X-ray Observatory", Review of Scientific Instruments, 2014, 85, 061101

[33]   Burbidge, E. M., "Redshifts of Thirteen Radio Galaxies, Astrophysical Journal", 1967, vol. 149, p. L51

[34]   Peterson, B. M., Ferrarese, L., Gilbert, K. M., et al., "CENTRAL MASSES AND BROAD-LINE REGION SIZES OF ACTIVE GALACTIC NUCLEI. II. A HOMOGENEOUS ANALYSIS OF A LARGE REVERBERATION-MAPPING DATABASE", 2004, The Astrophysical Journal, Volume 613, Issue 2, pp. 682-699

[35]   Walker, R. C., Benson, J. M., & Unwin, S. C., "The radio morphology of 3C 120 on scales from 0.5 parsecs to 400 kiloparsecs", 1987, Astrophysical Journal, vol. 316, May 15, p. 546-572

[36]   Eracleous M., Halpern J. P., "ACCURATE REDSHIFTS AND CLASSIFICATIONS FOR 110 RADIO-LOUD AGNS, 2004", The Astrophysical Journal Supplement Series, 150, p. 181–186

[37]   Gómez, J. L., Marscher, A. P., & Alberdi, A., "86, 43, and 22 GHz VLBI Observations of 3C 120", The Astrophysical Journal, 1999, 521, L29

[38]   Homan, D. C., Ojha, R., Wardle, J. F. C., et al., "PARSEC-SCALE BLAZAR MONITORING : PROPER MOTIONS", THE ASTROPHYSICAL JOURNAL, 2001, 549, 840

[39]   Walker, R. C., Benson, J. M., Unwin, S. C., Lystrup, M. B., Hunter, T. R., Pilbratt, G., & Hardee, P. E., "The structure and motions of the 3C 120 radio jet on scales of 0.6-300 parsecs, Astrophysical Journal", 2001, 556, 756

[40]   Hardee, P. E., Walker, R. C., & Gómez, J. L., "Modeling the 3C 120 radio jet from 1 to 30 milliarcseconds", 2005, The Astrophysical Journal, 620, 646

[41] García-Lorenzo, B., Sánchez, S. F., Mediavilla, E., González-Serrano, J. I., & Christensen, L., "Integral field spectroscopy of the central regions of 3C 120: Evidence of a past merging event", The Astrophysical Journal, 2005, 621, 146

[42] Halpern, J. P., "X-ray spectrum and variability of 3C 120", The Astrophysical Journal, 1985, 290, 130

[43] Marscher, A. P., Jorstad, S. G., Ǵomez, J.-L., et al., "Observational evidence for the accretion-disk origin for a radio jet in an active galaxy", Nature, 2002, 417, 625

[44] Hjorth, J., Vestergaard, M., Sorensen, A. N., & Grundahl, F., "DETECTION OF A FAINT OPTICAL JET IN 3C 120", THE ASTROPHYSICAL JOURNAL, 1995, 452, L17

[45] Zhang, J., Bai, J. M., Chen, L., & Liang, E., "X-ray Radiation Mechanisms and Beaming Effect of Hot Spots and Knots in Active Galactic Nuclear Jets", The Astrophysical Journa, 2010, 710, 1017

[46] Lin, Y. C., Bertsch, D. L., Dingus, B. L., et al., "EGRET Limits on High-Energy Gamma-Ray Emission from X-Ray--and Low-Energy Gamma-Ray--selected Seyfert Galaxies", Astrophysical Journal Letters,1993, v.416, p.L53

[47] Abdo, A. A., Ackermann, M., Ajello, M., et al., "THE FIRST CATALOG OF ACTIVE GALACTIC NUCLEI DETECTED BY THE FERMI LARGE AREA TELESCOPE", The Astrophysical Journal, 2010c, 715, 429

[48] Nolan, P. L., Abdo, A. A., Ackermann, M., et al., FERMI LARGE AREA TELESCOPE SECOND SOURCE CATALOG, The Astrophysical Journal Supplement Series, 2012, 199:31 (46pp)

[49] Kataoka, J., Stawarz, L., Takahashi, Y., et al., "Broad-line radio galaxies observed with Fermi-LAT: the origin of the GeV γ-ray emission", The Astrophysical Journal, 2011, 740:29 (16pp)

[50] Gehrels, N., Chincarini, G., Giommi, P., et al., "The Swift gamma-ray burst mission", The Astrophysical Journal, 2004, 611, 1005

[51] Kalberla, P. M. W.; Burton, W. B.; Hartmann, Dap; Arnal, E. M.; Bajaja, E.; Morras, R.; Pöppel, W. G. L., "The Leiden/Argentine/Bonn (LAB) Survey of Galactic HI. Final data release of the combined LDS and IAR surveys with improved stray-radiation

corrections", Astronomy and Astrophysics, Volume 440, Issue 2, September III 2005, pp.775-782

[52] Roming, P. W. A., Koch, T. S., Oates, S. R., et al. "The First Swift Ultraviolet/Optical Telescope GRB Afterglow Catalog", The Astrophysical Journal, 2009, 690, 163

[53] Schlafly, E. F. & Finkbeiner, D. P. "Measuring reddening with Sloan Digital Sky Survey stellar spectra and recalibrating SFD", The Astrophysical Journal, 2011, The Astrophysical Journal, 737, 103

[54] Breeveld, A. A., Landsman, W., Holland, S. T., et al., "An Updated Ultraviolet Calibration for the Swift/UVOT", in American Institute of Physics Conference Series, Vol. 1358, American Institute of Physics Conference Series, ed. J. E. McEnery, J. L. Racusin, & N. Gehrels, 373–376, 2011

[55] Poole, T. S., Breeveld, A. A., Page, M. J., et al. " Photometric calibration of the Swift ultraviolet/optical telescope", Monthly Notices of the Royal Astronomical Society, 2008, Volume 383, Issue 2, pp. 627-645

[56] Ma, C., Arias, E. F., Eubanks, T. M., et al. "The international celestial reference frame as realized by very long baseline interferometry", THE ASTRONOMICAL JOURNAL, 1998, 116, 516

[57] Harris, D. E., Hjorth, J., Sadun, A. C., Silverman, J. D., & Vestergaard, M. ,"X-Ray Emission from the Radio Jet in 3C 120", The Astrophysical Journal, 1999, Volume 518, Issue 1, pp. 213-218

[58] Ghisellini, G., Maraschi, L., & Treves, A. " Inhomogeneous synchrotron-self-Compton models and the problem of relativistic beaming of BL Lac objects" Astronomy and Astrophysics (ISSN 0004-6361), 1985, vol. 146, no. 2, p. 204-212

[59] Celotti, A., Maraschi, L., & Treves, A. " A model for the spectral variability of BL Lacertae objects at high frequencies", The Astrophysical Journal, 1991, 377, 403

[60] Bloom, S. and Marscher, A.,"An Analysis of the Synchrotron Self-Compton Model for the Multi--Wave Band Spectra of Blazars", The Astrophysical Journal, (1996), 461, 657.

[61] Abdo, A. A., Ackermann, M., Ajello, M., et al., "FERMI LARGE AREA TELESCOPE VIEW OF THE CORE OF THE RADIO GALAXY CENTAURUS A", The Astrophysical Journal, 2010b, 719, 1433

[62] Abdo, A. A., Ackermann, M., Ajello, M., et al., "Fermi Large Area Telescope Gamma-Ray Detection of the Radio Galaxy M87", The Astrophysical Journal, 2009a, Volume 707, Issue 1, pp. 55-60

[63] Abdo, A. A., Ackermann, M., Ajello, M., et al., "FERMI DISCOVERY OF GAMMA-RAY EMISSION FROM NGC 1275" 2009b, The Astrophysical Journal, 699, 31

[64] Giommi, P., Polenta, G., Lähteenmäki, A., et al. "Simultaneous Planck, Swift, and Fermi observations of X-ray and γ-ray selected blazars", Astronomy & Astrophysics, 2012,Volume 541, id.A160, 59 pp

[65] Bonnoli, G., Ghisellini, G., Foschini, L., Tavecchio, F., & Ghirlanda, G., "The γ-ray brightest days of the blazar 3C 454.3", Monthly Notices of the Royal Astronomical Society, 2011, Volume 410, Issue 1, pp. 368-380

[66] Tramacere, A., Giommi, P., Perri, M., Verrecchia, F., & Tosti, G., " Swift observations of the very intense flaring activity of Mrk 421 during 2006. I. Phenomenological picture of electron acceleration and predictions for MeV/GeV emission", Astronomy and Astrophysics, 2009, 501, 879

[67] Tramacere, A., Massaro, E., & Taylor, A. M., "STOCHASTIC ACCELERATION AND THE EVOLUTION OF SPECTRAL DISTRIBUTIONS IN SYNCHRO-SELF-COMPTON SOURCES: A SELF-CONSISTENT MODELING OF BLAZARS' FLARES", The Astrophysical Journal, 2011, 739:66 (16pp)

[68] Massaro, E., Tramacere, A., Perri, M., Giommi, P., & Tosti, G., " Log-parabolic spectra and particle acceleration in blazars-III. SSC emission in the TeV band from Mkn 501", Astronomy and Astrophysics, 2006, 448, 861

[69] Paggi, A., Cavaliere, A., Vittorini, V., D'Ammando, F., & Tavani, M., "Flaring Patterns in Blazars", The Astrophysical Journal, 2011, 736:128 (5pp)

[70] Tavecchio, F., Becerra-Gonzalez, J., Ghisellini, G., et al., "On the origin of the γ-ray emission from the flaring blazar PKS 1222+216", Astronomy and Astrophysics, 2011, 534, A86

[71] Sikora, M., Begelman, M. C., & Rees, M. J., "Comptonization of diffuse ambient radiation by a relativistic jet: The source of gamma rays from blazars Astrophysical Journal, Part 1 (ISSN 0004-637X), 1994,vol. 421, no. 1, p. 153-162

[72] Błazejowski, M., Sikora, M., Moderski, R., & Madejski, G. M. "Comptonization of infrared radiation from hot dust by relativistic jets in quasars", The Astrophysical Journal, 2000, Volume 545, Issue 1, pp. 107-116.

[73] Ghisellini, G., Maraschi, L., & Tavecchio, F., "The Fermi blazars' divide", Monthly Notices of the Royal Astronomical Society, 2009b, 396, L105

[74] Pozo Nuñez, F., Haas, M., Ramolla, M., et al., "Modelling photometric reverberation data: a disk-like broad-line region and a potentially larger black hole mass for 3C 120" Astronomy & Astrophysics, 2014, 568, A36

[75] Ghisellini, G. & Tavecchio, F., "Canonical high-power blazars", Monthly Notices of the Royal Astronomical Society, 2009, 397, 985

[76] Nenkova, M., Sirocky, M. M., Nikutta, R., Ivezi′c, Ž., & Elitzur, M., "AGN dusty tori. II. Observational implications of clumpiness", The Astrophysical Journal, 2008, 685, 160

[77] Shakura, N. I. & Sunyaev, R. A., "Black holes in binary systems. Observational appearance.", Astronomy and Astrophysics, 1973, Vol. 24, p. 337 - 355

[78] Janiak, M., Sikora, M., & Moderski, R., "Application of the spine-layer jet radiation model to outbursts in the broad-line radio galaxy 3C 120", Monthly Notices of the Royal Astronomical Society, 2016, Volume 458, Issue 3, p.2360-2370

[79] Zabalza, V. 2015, "Naima: a Python package for inference of particle distribution properties from nonthermal spectra", Proceedings of the 34th International Cosmic Ray Conference (ICRC2015), 30 July - 6 August, 2015, The Hague, The Netherlands. Online at http://pos.sissa.it/cgi-bin/reader/conf.cgi?confid=236, id.922

[80] Aharonian, F.A., Atoyan, A.M.: Compton scattering of relativistic electrons in compact X-ray sources. Ap&SS 79, (1981), 321–336

[81] Giannios, D., Uzdensky, D. A., & Begelman, M. C., "Fast TeV variability in blazars: jets in a jet", Monthly Notices of the Royal Astronomical Society: Letters, 2009, Volume 395, Issue 1, pp. L29-L33

[82] Ostrowski, M., "On possible 'cosmic ray cocoons' of relativistic jets", Monthly Notices of the Royal Astronomical Society, 2000, 312, 579

[83] Stawarz, Ł. & Ostrowski, M., "Radiation from the relativistic jet: a role of the shear boundary layer", The Astrophysical Journal, 2002, Volume 578, Issue 2, pp. 763-774.

[84] Celotti, A. & Ghisellini, G., "The power of blazar jets", Monthly Notices of the Royal Astronomical Society, 2008, Volume 385, Issue 1, pp. 283-300

[85] Ackermann, M., Ajello, M., Atwood, W. B., et al., "The third catalog of active galactic nuclei detected by the Fermi Large Area Telescope", The Astrophysical Journal, 2015, Volume 810, Issue 1, article id. 14, 34 pp.

[86] Blakeslee, J. P., Jordán, A., Mei, S., et al., "The ACS Fornax Cluster Survey. V. Measurement and Recalibration of Surface Brightness Fluctuations and a Precise Value of the Fornax-Virgo Relative Distance", The Astrophysical Journal, 2009, Volume 694, Issue 1, pp. 556-572

[87] Shklovsky, I. S., "Nature of Jets in Radio Galaxies", Soviet Astronomy, (1964), 7:748–754.

[88] Gebhardt, K.; Thomas, J., "The Black Hole Mass, Stellar Mass-to-Light Ratio, and Dark Halo in M87", 2009, The Astrophysical Journal, Volume 700, Issue 2, pp. 1690-1701

[89] Harris, D. E., Biretta, J. A., Junor, W., et al., "Flaring x-ray emission from HST-1, a knot in the M87 jet", The Astrophysical Journal, 2003, Volume 586, Issue 1, pp. L41-L44

[90] W. Junor, J.A. Biretta, & M. Livio, "Formation of the radio jet in M87 at 100 Schwarzschild radii from the central black hole", Nature 401, 1999, 891-892.

[91] Biretta, J. A., Sparks, W. B., & Macchetto, F., "Hubble Space Telescope observations of superluminal motion in the M87 jet", The Astrophysical Journal, 1999, 520, 621

[92] Asada K., Nakamura M., "The structure of the M87 jet: A transition from parabolic to conical streamlines", The Astrophysical Journal Letters, 2012, 745, L28

[93] Hada K., "The Structure and Propagation of the Misaligned Jet M87", Galaxies, 2017, vol. 5, issue 1, p. 2

[94] Evans, D. A.; Hardcastle, M. J.; Croston, J. H.; Worrall, D. M.; Birkinshaw, M., "Chandra and XMM-Newton observations of NGC 6251", Monthly Notices of the Royal Astronomical Society, Volume 359, Issue 1, pp. 363-382

[95] Biretta, J. A., Stern, C. P., & Harris, D. E., "The radio to X-ray spectrum of the M87 jet and nucleus", The Astronomical Journal, 1991, AJ, 101, 1632

[96] Neumann, M., Meisenheimer, K., Röser, H.-J., & Fink, H. H., "ROSAT-HRI observations of the jet in M 87", Astronomy and Astrophysics, 1997, v.318, p.383-389

[97] Bo¨hringer, H., et al., "XMM-Newton observations of M 87 and its X-ray halo", Astronomy and Astrophysics, 2001, 365, L181

[98] Wilson, A. S.; Yang, Y., "Chandra X-Ray Imaging and Spectroscopy of the M87 Jet and Nucleus", The Astrophysical Journal, 2002, Volume 568, Issue 1, pp. 133-140

[99] Perlman, Eric S.; Wilson, Andrew S., "The X-Ray Emissions from the M87 Jet: Diagnostics and Physical Interpretation", The Astrophysical Journal, 2005, Volume 627, Issue 1, pp. 140-155

[100] Perley, R. A., Roser, H. J., & Meisenheimer, K., "The radio galaxy PictorA--a study with the VLA", Astronomy and Astrophysics, 1997, v.328, p.12-32

[101] Danziger, I. J., Fosbury, R. A. E., & Penston, M. V., "Optical observations of Pictor A" Monthly Notices of the Royal Astronomical Society, Apr. 1977, vol. 179, p. 41P-45P.

[102] L. G. Robertson, "An all-sky catalogue of strong radio sources at 408 mhz", Australian Journal of Physics, 1973, 26, 403

[103] Tingay, S.J., et al., "The parsec-scale structure and evolution of the nearby Fanaroff-Riley type II radio galaxy Pictor A", THE ASTRONOMICAL JOURNAL, 2000, v. 119 pp. 1695-1700

[104] Tingay, S.J., Lenc, E., Brunetti, G. & Bondi, M., "A high resolution view of the jet termination shock in a hot spot of the nearby radio galaxy Pictor A: implications for X-ray models of radio galaxy hot spots", The Astronomical Journal, 2008, Volume 136, Issue 6, pp. 2473-2482

[105] Hardcastle, M. J.; Lenc, E.; Birkinshaw, M.; Croston, J. H.; Goodger, J. L et al. "Deep Chandra observations of Pictor A", Monthly Notices of the Royal Astronomical Society, 2016, Volume 455, Issue 4, p.3526-3545.

[106] Brown, A. M. & Adams, J., "Discovery of γ-ray emission from the broad-line radio galaxy Pictor A", Monthly Notices of the Royal Astronomical Society, 2012, 421, 2303-2309

[107] Leahy, J. P. & Perley, R. A., "VLA images of 23 extragalactic radio sources", Astronomical Journal (ISSN 0004-6256), vol. 102, Aug. 1991, p. 537-561.

[108] Lonsdale, C. J., Hartley-Davies, R., & Morison, I, "The radio structure of 3C303 at 408 MHz", Monthly Notices of the Royal Astronomical Society, 1983, vol. 202, p. 1P-5P.

[109] Giovannini, G., Cotton, W. D., Feretti, L., Lala, L., & Venturi, T., "VLBI Observations of a Complete Sample of Radio Galaxies: 10 Years Later", The Astrophysical Journal, 2001, Volume 552, Issue 2, pp. 508-526

[110] Kronberg, P. P., "3C 303: a source with unusual radio and optical properties", The Astrophysical Journal, 1976, 203, L47

[111] Kataoka, J.; Edwards, P.; Georganopoulos, M.; Takahara, F.; Wagner, S., "Chandra detection of hotspot and knots of 3C 303", Astronomy and Astrophysics, 2003, v.399, p.91-97

[112] Bridle, A. H., & Perley, R. A., "Extragalactic Radio Jets", IN: Annual review of astronomy and astrophysics. Volume 22. Palo Alto, CA, Annual Reviews, Inc., 1984, p. 319-358

[113] Hintzen, P., & Stocke, J., "Detection of a rotating gas cloud 100 kiloparsecs in diameter surrounding 3C 275.1, a quasar at the center of a rich cluster of galaxies", The Astrophysical Journal, 1986, 308, 540

[114] Stocke, J. T., Burns, J. O., & Christiansen, W. A., "VLA observations of quasars with 'Dogleg' radio structure", Astrophysical Journal, Part 1 (ISSN 0004-637X), vol. 299, Dec. 15, 1985, p. 799-813

[115] Hough, D. H., Vermeulen, R. C., Readhead, A. C. S., et al., "Parsec-Scale Radio Structure and Broad Optical Emission Lines in a Complete Sample of 3CR Lobe-dominated Quasars", The Astronomical Journal, 2002, v. 123, p.1258–1287

[116] Crawford, C. S., & Fabian, A. C., "Extended X-ray emission around four 3C quasars at 0.55> z< 0.75 observed with Chandra", Monthly Notices of the Royal Astronomical Society, 2003,Volume 339, Issue 4, Pages 1163–1169

[117] Werner, M. W., Murphy, D. W., Livingston, J. H., et al., "SPITZER OBSERVATIONS OF HOTSPOTS IN RADIO LOBES", The Astrophysical Journal, 2012, 759:86 (21pp)

[118] Cheung, C. C.; Wardle, J. F. C.; Chen, Tingdong, "Discovery of Optical Emission in the Hot Spots of Three 3CR Quasars: High-Energy Particle Acceleration in Powerful Radio Hot Spots", The Astrophysical Journal, 2005, Volume 628, Issue 1, pp. 104-112

[119] Marziani, P., Sulentic, J. W., Dultzin-Hacyan, D., Calvani, M., & Moles, M., "Comparative Analysis of the High- and Low-Ionization Lines in the Broad-Line Region of Active Galactic Nuclei", Astrophysical Journal Supplement, 1996, v.104, p.37

[120] Bogers, W. J., Hes, R., Barthel, P. D., & Zensus, J. A., "High resolution radio observations of intermediate redshift quasars and radio galaxies", Astronomy and Astrophysics Suppl., 1994, Vol. 105, p.91-113

[121] Herbig, T., & Readhead, A. C. S., "A compendium of radio spectra and luminosities for three complete samples of radio sources", Astrophysical Journal Supplement Series (ISSN 0067-0049), 1992,vol. 81, no. 1, July 1992, p. 83-124

[122] Brunetti, G., Bondi, M., Comastri, A., & Setti, G., "Chandra discovery of extended non-thermal emission in 3C 207 and the spectrum of the relativistic electrons", Astronomy & Astrophysics, 2002, 381, 795

[123] Ackermann, M., Ajello, M., Atwood, W. B., et al., "The Second Catalog of Active Galactic Nuclei Detected by the Fermi Large Area Telescope", The Astrophysical Journal, 2011, Volume 743, Issue 2, article id. 171, 37 pp.

[124] Sambruna, R. M., Gambill, J. K., Maraschi, L., et al., "A Survey of Extended Radio Jets with Chandra and the Hubble Space Telescope", 2004, The Astrophysical Journal, Volume 608, Issue 2, pp. 698-720

[125] Sargent W.L.W., "Redshifts for six 3CR radio galaxies and the spectrum of 3C 111", 1977, The Astrophysical Journal, vol. 212, p. L105, L106

[126] Véron-Cetty M.P., Véron P., A catalogue of quasars and active nuclei, 2010, Astronomy & Astrophysics 518, A10

[127] Leahy J.P., Black A.R.S., Dennett-Thorpe J., et al., "A study of FR II radio galaxies with z < 0.15 — II. High-resolution maps of 11 sources at 3.6 cm", Monthly Notices of the Royal Astronomical Society, 1997, Volume 291, Issue 1, pp. 20-53

[128] Jorstad, S. G., Marscher, A. P., Lister, M. L., et al., "Polarimetric Observations of 15 Active Galactic Nuclei at High Frequencies: Jet Kinematics from Bimonthly Monitoring with the Very Long Baseline Array", The Astronomical Journal, 2005, Volume 130, Issue 4, pp. 1418-1465

[129] Clautice D., Perlman E.S., Georganopoulos M., et al., "The Spectacular Radio-near-IR-X-Ray Jet of 3C 111: The X-Ray Emission Mechanism and Jet Kinematics", The Astrophysical Journal, 2016, Volume 826, Issue 2, article id. 109, 12 pp

[130] Hogan, B., Lister, M. L., Kharb, P., Marshall, H. L., Cooper, N. J., "Chandra Discovery of 10 New X-ray Jets Associated with FR II Radio Core-selected AGNs in the MOJAVE Sample", The Astrophysical Journal, 2011, 730, 92

[131] Wegner, G., Bernardi, M., Willmer, C. N. A., et al., "Redshift-Distance Survey of Early-Type Galaxies: Spectroscopic Data", The Astronomical Journal, 2003, Volume 126, Issue 5, pp. 2268-2280

[132] Ferrarese, L., & Ford, H. C., "Nuclear Disks of Gas and Dust in Early-Type Galaxies and the Hunt for Massive Black Holes: Hubble Space Telescope Observations of NGC 6251", The Astrophysical Journal, 1999, Volume 515, Issue 2, pp. 583-602

[133] Perley, R. A., Bridle, A. H., & Willis, A. G., "High-resolution VLA observations of the radio jet in NGC 6251", Astrophysical Journal Supplement Series (ISSN 0067-0049), 1984, vol. 54, p. 291-334

[134] Sambruna, R. M., Gliozzi, M., Donato, D., et al., "The XMM-Newton view of the X-ray halo and jet of NGC 6251", Astronomy and Astrophysics, 2004, v.414, p.885-894

[135] Werner, P. N.; Worrall, D. M.; Birkinshaw, M, "NGC 6251 at multiple scales and wavelengths", Particles and Fields in Radio Galaxies Conference, ASP Conference Proceedings Vol. 250. Edited by Robert A. Laing and Katherine M. Blundell. ISBN: 1-58381-090-0. San Francisco: Astronomical Society of the Pacific, 2001. p.294

[136] Mattox, J. R., Bertsch, D. L., Chiang, J., Dingus, B. L., Digel, S. W., Esposito, J. A, "The Likelihood Analysis of EGRET Data", Astrophysical Journal, 1996, v.461, p.396